

HIGH-ENERGY EMISSION AND TEMPORAL PROPERTIES OF
MAGNETARS

by
SİNEM ŞAŞMAZ MUŞ

Submitted to the Graduate School of Engineering and Natural Sciences
in partial fulfillment of
the requirements for the degree of
Doctor of Philosophy

Sabancı University
April 2014

HIGH-ENERGY EMISSION AND TEMPORAL PROPERTIES
OF MAGNETARS

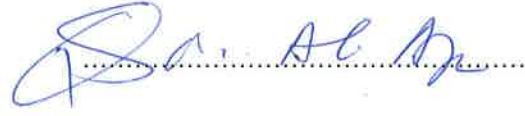
APPROVED BY:

Prof. Ersin Göğüş



(Dissertation Supervisor)

Prof. M. Ali Alpar



Assoc. Prof. K. Yavuz Ekşi



Assoc. Prof. Ünal Ertan



Assoc. Prof. Mehmet Keskinöz



DATE OF APPROVAL: 22.04.2014

© SİNEM ŞAŞMAZ MUŞ 2014

All Rights Reserved

ABSTRACT

HIGH-ENERGY EMISSION AND TEMPORAL PROPERTIES OF MAGNETARS

Sinem Şaşmaz Muş

Physics, Ph.D. Thesis, 2014

Supervisor: Prof. Ersin Göğüş

Keywords: pulsars, magnetars, X-rays, gamma-rays

Magnetars have been intriguing sources since their discovery, as they opened new avenues on the formation, evolution and emission mechanisms of the neutron stars. Thanks to the long-term observations of these sources, we are able to investigate many aspects of them. In this thesis, we investigate the high-energy gamma-ray emission properties of one of the brightest magnetars in X-ray band, 4U 0142+61. We searched for persistent and pulsed gamma-ray emission using the data obtained with *Fermi*/LAT. We did not detect significant high-energy gamma-ray emission from this source. Nevertheless, we could place upper limits to the gamma-ray flux and spectral break energy of the source. Together with the earlier works on soft and hard X-ray emission of 4U 0142+61, these upper limits provide a hint on the spectral shape of the source in a wide energy band. Next, we studied the long-term timing and X-ray properties of two frequently glitching magnetars, 1RXS J170849.0-400910 and 1E 1841-045, with *RXTE*/PCA. In the analysis of 1RXS J170849.0-400910 we identified two significant glitch candidates in two data gaps. The source was radiatively stable during the *RXTE* observations. In the analysis of 1E 1841-045, we identified a glitch and an anti-glitch ~ 1 yr apart from each other. We found no evidence of radiative variability during both the glitch and anti-glitch events. Finally, we discuss our results in the context of glitch models.

ÖZ

MAGNETARLARIN YÜKSEK ENERJİ IŞIMA VE ZAMANSAL ÖZELLİKLERİ

Sinem Şaşmaz Muş

Fizik, Doktora Tezi, 2014

Danışman: Prof. Ersin Göğüş

Anahtar Kelimeler: atarcılar, magnetarlar, X ışınları, gama ışınları

Magnetarlar keşiflerinden beri, nötron yıldızlarının oluşumu, evrimi ve ışım mekanizmaları hakkında yeni alanlar açmaları sebebiyle merak uyandırıcı kaynaklar olmuşlardır. Bu kaynakların uzun süreli gözlemleri sayesinde birçok özelliklerini araştırabiliyoruz. Bu tezde, X ışını bandında en parlak magnetarlardan biri olan 4U 0142+61'in yüksek enerji gama ışını ışım özelliklerini inceledik. *Fermi*/LAT verilerini kullanarak sürekli ve atımlı gama ışını ışımını aradık. Bu kaynaktan belirgin bir gama ışımını gözlemleyemedik. Ancak, bu kaynağın gama ışını akısına ve tayfsal enerji dağılımının kırınım enerjisine üst limit belirledik. 4U 0142+61 kaynağının yumuşak ve sert X ışını ışımını üzerine daha önceki çalışmalar ile birlikte bu üst limitler, kaynağın geniş enerji aralığındaki tayf özelliğine dair önemli ipucu sağlamaktadır. Daha sonra, sıkça sıçrama gösteren iki magnetarın, 1RXS J170849.0-400910 ve 1E 1841-045, *RXTE*/PCA ile elde edilen verilerini kullanarak uzun süreli zamanlama ve X ışını özelliklerini çalıştık. 1RXS J170849.0-400910'un analizlerinde iki veri boşluğunda iki belirgin sıçrama adayını tespit ettik. Kaynak *RXTE* gözlemleri süresince ışınımsal olarak kararlıydı. 1E 1841-045'in analizlerinde birbirinden ~1 yıl aralıklı bir sıçrama ve bir zıt sıçrama tespit ettik. Sıçrama ve zıt sıçrama olaylarının ikisinde de ışınımsal değişkenliğe dair bir kanıt bulamadık. Son olarak, sonuçlarımızı sıçrama modelleri çerçevesinde tartıştık.

ACKNOWLEDGEMENTS

Foremost, I would like to express my gratitude and appreciation to my advisor Ersin Göğüş for his guidance and patience. I would like to thank M. Ali Alpar for valuable discussions and his support. I would also like to thank Emrah Kalemci and Ünal Ertan for their support and valuable comments.

I acknowledge support from EU FP6 Transfer of Knowledge Project Astrophysics of Neutron Stars (MTKD-CT-2006-042722). I acknowledge support through the national graduate fellowship program of the Scientific and Technological Research Council of Turkey (TÜBİTAK).

I would like to thank Şirin and Aslıhan for their support and warm friendship. I am also thankful to Atakan Gürkan and Barış Pekerten for their friendship.

Finally, I would like to thank Köksal and my family for their support and love.

CONTENTS

List of Tables	ix
List of Figures	x
List of Abbreviations	xiv
1 Introduction	1
1.1 Neutron Stars	1
1.1.1 Historical Overview	1
1.1.2 Basics of Neutron Stars	2
1.1.3 Emission Mechanisms	11
1.1.4 Glitches	15
1.2 Magnetars	17
1.2.1 General Properties	17
1.2.2 Theoretical Models	17
1.3 Thesis Outline	26
1.4 Instruments	27
2 Search for High-Energy Gamma-ray Emission from an Anoma- lous X-ray Pulsar, 4U 0142+61	32
2.1 Abstract	33
2.2 Introduction	33
2.3 Observations and Data Analysis	35
2.3.1 <i>Fermi</i> /LAT	35
2.3.2 <i>RXTE</i>	36
2.4 Results	37
2.4.1 Search for Persistent Emission	37
2.4.2 Search for Pulsed Emission	37
2.5 Discussion	39
3 Long-Term Timing and Glitch Characteristics of Anomalous X- ray Pulsar 1RXS J170849.0-400910	42

3.1	Abstract	43
3.2	Introduction	43
3.3	<i>RXTE</i> Observations	45
3.4	Data Analysis And Results	46
	3.4.1 Phase Coherent Timing	46
	3.4.2 Pulse Profile Evolution	47
	3.4.3 Pulsed Count Rates	51
	3.4.4 Search for Glitches	53
3.5	Discussion and Conclusions	54
4	A Glitch and an Anti-glitch in the Anomalous X-ray Pulsar 1E 1841-045	61
	4.1 Abstract	62
	4.2 Introduction	62
	4.3 Observations and Data Processing	64
	4.4 Data Analysis & Results	64
	4.5 Discussion and Conclusions	69
5	Summary and Outlook	73

LIST OF TABLES

2.1	Spin ephemeris of 4U 0142+61	38
3.1	Pulse Ephemeris of 1RXS J170849.0-400910	47
3.2	Timing Solutions in the Segments (Including the Gaps)	54
3.3	Critical parameter values and results of the expectancy analysis of 1RXS J170849.0-400910	59
4.1	Pulse Ephemeris of 1E 1841-045	64
4.2	Parameters for Glitch 4	67
4.3	Parameters for Anti-glitch	68

LIST OF FIGURES

1.1	Mass-Radius (M-R) relations calculated for different equations of state (EOSs). Black curves represent the hadronic EOSs while green curves are for strange quark matter EOSs. For the explanation of EOSs, see table 1 of Lattimer & Prakash (2001). Figure is taken from Lattimer (2012).	3
1.2	Schematic figure of a pulsar.	6
1.3	Period-period derivative diagram. Light gray dots represent radio pulsars. Magnetars are shown with diamonds. Rotating Radio Pulsars (RRAT) and X-ray Dim Isolated Neutron Stars (XDINS) are shown with star and triangle symbols, respectively. The data were taken from ATNF pulsar catalogue (Manchester et al., 2005). The period derivative of SGR 0418+5729 is taken from Rea et al. (2013).	9
1.4	Pulsar magnetosphere model of Goldreich & Julian (1969). Figure is taken from Goldreich & Julian (1969).	12
1.5	Neutron star structure. $\rho_{ND} = 4.3 \times 10^{11}$ g cm ⁻³ is the neutron drip density and $\rho_0 = 2.8 \times 10^{14}$ g cm ⁻³ is the nuclear matter saturation density. Figure is taken from Haensel et al. (2007).	14
1.6	A wide band νF_ν spectrum of four AXPs: Spectra of two young radio pulsars, Crab and PSR B1509–58 and a middle-aged pulsar, Vela pulsar, are presented for comparison. Figure is taken from Kuiper et al. (2006).	23
1.7	<i>INTEGRAL</i> detection of five magnetars above 18 keV. Dotted lines above 18 keV represent best fit power-law models. Blackbody (dashed lines) plus absorbed power-law (dotted lines) emission models below 10 keV are shown with solid lines. Figure is taken from Götz et al. (2006).	24

1.8	A wide band spectra of 4U 0142+61: <i>XMM-Newton</i> observations (0.55–11.5 keV) are shown in black. Black squares represent the <i>INTEGRAL</i> /ISGRI (20–300 keV) data, red open squares are <i>INTEGRAL</i> /SPI (20–1000 keV) data and black arrows represent the 2σ <i>CGRO</i> /COMPTEL (0.75–30 MeV) upper limits. Dashed line is the best fit power law model to the ISGRI data points and the blue curve is logparabola fit to the whole data (den Hartog et al., 2008). Figure is taken from den Hartog et al. (2008).	25
1.9	Schematic figure of <i>RXTE</i> and its instruments PCA, HEXTE and ASM. Figure is taken from webpage of NASA	28
1.10	Schematic view of LAT. Tracker, calorimeter, anticoincidence and data acquisition systems are shown. The outermost layer is the thermal blanket. The Grid is composed of aluminum and supports the instrument. Figure is taken from Atwood et al. (2007).	29
1.11	Structure of the converter-tracker system. Conversion of an incident photon to a pair and propagation of the pair between the layers are shown. Figure is taken from Atwood et al. (2007).	30
2.1	Smoothed <i>Fermi</i> /LAT count map around AXP 4U 0142+61 in the 0.2–100 GeV energy range. The large circle and small circle show the 15° and 2° radius extraction regions, respectively. The plus sign indicates the position of AXP 4U 0142+61.	35
2.2	(<i>Top</i>) spin phase shifts of <i>RXTE</i> /PCA observations of 4U 0142+61 with respect to the epoch. The solid line is the best fitting model, that is a third-order polynomial. (<i>Bottom</i>) residuals of the fit.	38
2.3	<i>Fermi</i> /LAT pulse profiles of 4U 0142+61. <i>Left</i> : in the 30–200 MeV band, <i>Middle</i> : in the 200 MeV–1 GeV band, <i>Right</i> : in the 1–10 GeV band.	39
2.4	Wide band νF_ν spectrum of 4U 0142+61: <i>INTEGRAL</i> /ISGRI (20–300 keV) in black (stars), <i>INTEGRAL</i> /SPI (20–1000 keV) in red (open squares) and <i>CGRO</i> /COMPTEL (0.75–30 MeV) 2σ upper limits in black (data constructed from den Hartog et al., 2008). <i>Fermi</i> /LAT upper limits (in the 0.2–1.0 GeV and 1.0–10.0 GeV) obtained using the 2° extraction region are shown in blue diamonds and that of 15° extraction region in red triangles. Dashed line is the best fit power law model to the ISGRI data points (den Hartog et al., 2008). Solid line shows the power law upper limit trend of the 2° <i>Fermi</i> /LAT region.	40

3.1	Distribution of exposure times of individual <i>RXTE</i> /PCA observations. The shortest observation with an exposure of 0.25 ks is excluded for clarity.	46
3.2	(a) Spin frequency evolution of 1RXS J170849.0-400910. (b) Phase residuals after the subtraction of the pulse ephemeris given in Table 3.1. (c) Frequency derivatives obtained using ~ 2.5 months long data segments. (d) Long-term behavior of the rms pulsed count rates in the 2–10 keV band.	48
3.3	Pulse profile history of 1RXS J170849.0-400910 in the energy bands 2–10, 2–4 and 4–6 keV. The labels on the right are the corresponding time intervals of accumulated data.	49
3.4	Pulse profile history of 1RXS J170849.0-400910 in the energy bands 6–8, 8–12 and 12–30 keV. The labels on the right are the corresponding time intervals of accumulated data. The 12–30 keV profiles are plotted with 20 phase bins due to lower count rate in this energy band.	50
3.5	Time evolution of the normalized Fourier harmonic powers in the first three harmonics. Dashed lines represent the averaged power of the related harmonic in all segments. The energy intervals in which the powers are calculated are displayed inside the panels.	51
3.6	Plots of rms pulsed count rates vs. energy. Time intervals within which these plots were obtained are shown in the top-right of each panel. Solid lines show the best fit power law trends to the corresponding energy dependent rms pulsed count rates. Uncertainties in these power law indices refer to the last digit as shown in parenthesis in each panel.	52
3.7	<i>Left column:</i> Phase residuals of the polynomial fit to each data segment. <i>Right column:</i> Phase residuals of the glitch model fit.	55
3.8	<i>Left column:</i> Phase residuals of the polynomial fit to each gap segment. <i>Right column:</i> Phase residuals of the glitch model fit.	56

4.1	<p><i>Top panel:</i> Phase residuals after the subtraction of the polynomial models presented in Table 4.1 from data. For Segment 1 we present the phase residuals after subtraction of the polynomial model (blue diamonds) presented in Table 4.1 and glitch model presented in Table 4.2 (see Figure 4.2 for more detailed presentation of this segment). <i>Middle panel:</i> Frequency derivative evolution of the source. <i>Bottom panel:</i> Evolution of the pulsed count rates in the 2–10 keV band. The times of glitch 4 and anti-glitch are shown with the vertical dotted and dashed lines, respectively. Solid vertical lines indicate the times of energetic bursts listed in table 1 of Lin et al. (2011). Data gaps are indicated with light gray bars.</p>	66
4.2	<p>(a) Spin frequency evolution of the source during Segment 1. (b) Phase residuals after the subtraction of a fourth order polynomial model from the data. (c) Phase residuals after subtracting the glitch model. (d) Pulsed count rates of the source in the 2–10 keV band obtained using sets of observations spanning mostly over 40–50 days to ensure significant pulsed flux measurement.</p>	68
4.3	<p>(a) Spin frequency evolution of the source during Segment 2. The solid line is the spin-down trend obtained by fitting the observations before MJD ~ 54630, and extrapolated onwards. (b) Residuals of the model and its extrapolation in (a). (c) Phase residuals after the subtraction of a fourth order polynomial fit presented in Table 4.1. (d) Phase residuals after the subtraction the glitch model presented in Table 4.3 (e) The pulsed count rates in 2–10 keV averaged over ~ 40 days.</p>	69

LIST OF ABBREVIATIONS

ADAF	Advection-Dominated Accretion Flow
AXP	Anomalous X-Ray Pulsar
BMC	Bulk-Motion Comptonization
CCO	Central Compact Object
CGRO	Compton Gamma Ray Observatory
COMPTEL	Imaging Compton Telescope
DOF	Degrees of Freedom
EGRET	Energetic Gamma Ray Experiment Telescope
EOS	Equation of State
Fermi	Fermi Gamma-ray Space Telescope
FOV	Field of View
FP	Fourier Power
GBM	Gamma-ray Burst Monitor
INTEGRAL	International Gamma-Ray Astrophysics Laboratory
ISGRI	INTEGRAL Soft Gamma-Ray Imager
LAT	Large Area Telescope
MJD	Modified Julian Date
PCA	Proportional Counter Array
PCU	Proportional Counter Unit
PSR	Pulsar
RQNS	Radio-Quiet Neutron Star
RRAT	Rotating Radio Transient
RXTE	Rossi X-ray Timing Explorer
SGR	Soft Gamma-Ray Repeater
SNR	Supernova Remnant
SPI	Spectrometer on INTEGRAL
SSD	Silicon Strip Detector
TOA	Time of Arrival
TS	Test Statistics
XDINS	X-Ray Dim Isolated Neutron Star

Chapter 1

Introduction

1.1 Neutron Stars

A Neutron Star is a compact object left after the explosion, a.k.a supernova explosion, of a massive star. Neutron stars typically have masses ~ 1.4 Solar mass (M_{\odot}) and radii ~ 10 km. When the progenitor star runs out of its internal energy source, the core of the star cannot support the matter pressure and starts to collapse. Stars in the mass range of $8 M_{\odot} - 20 M_{\odot}$ (see, e.g., Wellstein & Langer, 1999; Woosley et al., 2002) collapse until the gravitational energy of the falling material is supported by the pressure of degenerate neutrons. This leads to the formation of neutron stars as a dense compact remnant. Below, a short chronological overview of the major developments in the field of neutron stars is provided.

1.1.1 Historical Overview

Existence of dense objects were first proposed by Landau (1932) and Baade & Zwicky (1934) just after the discovery of neutron by Chadwick (1932). In 1965 Hewish and Okoye discovered an unusual source of high radio brightness temperature in the Crab Nebula (Hewish & Okoye, 1965). Two years after this discovery, Jocelyn Bell noticed an unusual signal in the radio data and in their 1968 paper (Hewish et al., 1968) announced the discovery of a rapidly pulsating radio source which is now called a pulsar. Anthony Hewish was awarded the Nobel prize in 1974 “*for his decisive role in the discovery of pulsars*”¹. In 1967 Pacini proposed that the unusual source in Crab Nebula is also a pulsar (Pacini, 1967). Soon after that Crab pulsar was observed by Staelin & Reifenstein (1968). It is proposed that these pulsations can be explained by radiation produced by the relativistic plasma within the magnetosphere around a rotating and highly magnetized neutron star (Pacini, 1967; Gold, 1968, 1969). In

¹“The Nobel Prize in Physics 1974”. Nobelprize.org. Nobel Media AB 2013. Web. 16 May 2014. <http://www.nobelprize.org/nobel_prizes/physics/laureates/1974/>

1962 Giacconi et al. (1962) detected X-ray emission outside the solar system from a source now known as Scorpius X-1, a neutron star accreting matter from a normal companion star and emitting radiation. Giacconi was awarded the Nobel Prize in 2002 “for pioneering contributions to astrophysics, which have led to the discovery of cosmic X-ray sources”². Russell A. Hulse and Joseph H. Taylor discovered the first pulsar-neutron star binary system in 1974 (Hulse & Taylor, 1975). In 1993 they were awarded the Nobel Prize “for the discovery of a new type of pulsar, a discovery that has opened up new possibilities for the study of gravitation”³. These possibilities have been extended by the discovery of the first double neutron star system both observed to be pulsars (Burgay et al., 2003; Lyne et al., 2004).

Since the first observation of a pulsar in 1967 (Hewish et al., 1968) many different types of pulsars have been discovered, with different characteristics. Pulsation periods of pulsars range from milliseconds to hundreds of seconds (see, e.g., Manchester et al., 2005; Haberl & Pietsch, 2005) and surface magnetic field strengths range from 10^8 to 10^{15} G (see, e.g., Manchester et al., 2005). Initially discovered as pulses in radio band, some of them are now observed in optical, X-ray and gamma-ray bands. They are found to be in binary systems or isolated without any evidence of a companion. Pulsars with millisecond periods have low magnetic fields and are thought to be old pulsars spun-up via angular momentum transfer through accretion from their binary companion (Alpar et al., 1982). At the higher end of the magnetic field strength range are anomalous X-ray pulsars (AXPs) and soft gamma-ray repeaters (SGRs) (see, e.g., Mereghetti, 2013, for a recent review). Other classes of pulsars include rotating radio transients (RRATs), X-ray dim isolated neutron stars (XDINSs), central compact objects (CCOs), and radio-quiet neutron stars (RQNSs). Current research involves the distinct properties of these sources and possible evolutionary links between them.

1.1.2 Basics of Neutron Stars

1.1.2.1 Masses and Radii

Investigations on the mass and radius limits of neutron stars started soon after the suggestion of their existence in 1934. As these stars are so compact, implying densities larger than the nuclear saturation density, general relativity effects must be taken into account. The structure of a neutron star is determined by the solutions of the Tolman-Oppenheimer-Volkoff (TOV) equations which are hydrostatic equilibrium equations for relativistic nonrotating spherically symmetric matter with a

²“The Nobel Prize in Physics 2002”. Nobelprize.org. Nobel Media AB 2013. Web. 16 May 2014. <http://www.nobelprize.org/nobel_prizes/physics/laureates/2002/>

³“The Nobel Prize in Physics 1993”. Nobelprize.org. Nobel Media AB 2013. Web. 16 May 2014. <http://www.nobelprize.org/nobel_prizes/physics/laureates/1993/>

particular equation of state: the relation between pressure and density (Tolman, 1939; Oppenheimer & Volkoff, 1939). Since the equation of state of dense matter is not fully understood at neutron star densities, there is no unique mass and radius limit for a neutron star (see Figure 1.1). First calculations by Oppenheimer & Volkoff (1939) on the maximum mass which a neutron star can support using noninteracting degenerate relativistic neutron gas equation of state give a mass of $0.7 M_{\odot}$. Rhoades & Ruffini (1974) calculated the maximum mass of a neutron star without needing the details of the equation of state. In the context of general relativity, they assumed that the pressure is a monotonically increasing function of density (Le Chatelier's principle) and the principle of the causality where the sound speed is smaller than the speed of light. According to these assumptions the maximum mass of a neutron star cannot exceed the value of $\sim 3.2 M_{\odot}$ (Rhoades & Ruffini, 1974).

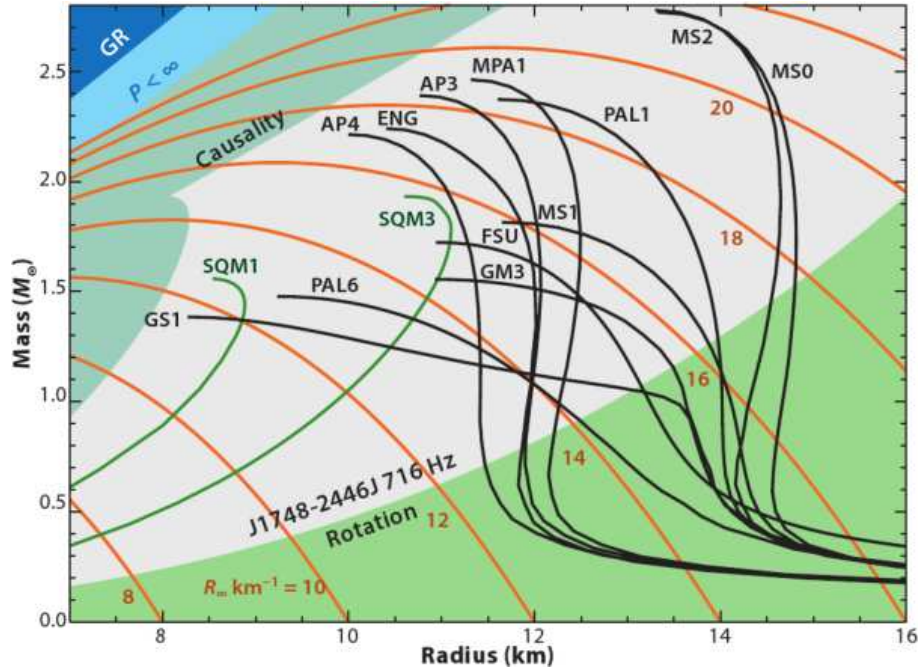


Figure 1.1: Mass-Radius (M-R) relations calculated for different equations of state (EOSs). Black curves represent the hadronic EOSs while green curves are for strange quark matter EOSs. For the explanation of EOSs, see table 1 of Lattimer & Prakash (2001). Figure is taken from Lattimer (2012).

We can roughly estimate the maximum mass of a neutron star, without including the general relativistic effects, by following Landau (1932) and Shapiro & Teukolsky (1983): Fermi energy of a relativistic particle is

$$E_F = pc \sim \hbar n^{1/3} c \sim \frac{\hbar c N^{1/3}}{R}, \quad (1.1)$$

where \hbar and c are the Planck constant and speed of light, respectively. N is the

number of fermions and $n \sim N/R^3$ is the number density of fermions in a star of radius R . In a star of mass M , the gravitational energy per fermion is

$$E_G \sim -\frac{GMm_B}{R} \sim -\frac{GNm_B^2}{R}. \quad (1.2)$$

Here mass of the star is taken as $M = Nm_B$ where m_B is the baryon mass. Then, the total energy of the star, $E = E_F + E_G$, is

$$E \sim \frac{\hbar c N^{1/3}}{R} - \frac{GNm_B^2}{R}. \quad (1.3)$$

As discussed in Shapiro & Teukolsky (1983) the star can be bound for a maximum baryon number when $E = 0$ which gives:

$$N_{max} \sim \left(\frac{\hbar c}{Gm_B^2} \right)^{3/2} \sim 2 \times 10^{57}, \quad (1.4)$$

and the maximum mass that a neutron star can achieve is given by:

$$M_{max} \sim N_{max}m_B \sim 1.5 M_\odot. \quad (1.5)$$

Relativistic neutrons start to become degenerate when the Fermi energy (Equation (1.1)) is on the order of their rest mass energy, i.e.

$$E_F \gtrsim m_n c^2. \quad (1.6)$$

Once they become degenerate, they will balance against gravitational collapse. Equilibrium radius, from Equations (1.1) and (1.6), is given by

$$R \leq \frac{\hbar}{m_n c} \left(\frac{\hbar c}{Gm_B^2} \right)^{1/2} \sim 3 \times 10^5 \text{ cm}. \quad (1.7)$$

Besides theoretical studies, there are many observational efforts on determining masses and radii of neutron stars, hence on constraining the equation of state. Observations of quiescent emission (Heinke et al., 2006; Webb & Barret, 2007), X-ray bursts with photospheric radius expansion (Damen et al., 1990; Özel, 2006; Galloway et al., 2008), quasiperiodic oscillations (Miller et al., 1998), timing properties (Link et al., 1999), and Keplerian parameters of binary systems (see, e.g., Thorsett & Chakrabarty, 1999) provide invaluable information on the mass and radius of the star (see, e.g., Lattimer, 2010, 2012; Özel, 2013, for details of these methods). Masses of many neutron stars are measured via observations of binary systems with neutron stars (see recent review by Lattimer, 2012, and references therein). Among them, timing observations of radio binary pulsars provide the most accurate mass measurements and they give a mass of $\sim 1.4 M_\odot$ (Lattimer, 2012). The largest

well-measured neutron star masses observed until now are $1.97 \pm 0.04 M_{\odot}$ (PSR J1614-2230) (Demorest et al., 2010) and $2.01 \pm 0.04 M_{\odot}$ (PSR J0348+0432) (Antoniadis et al., 2013) which have already put challenges on soft equations of state.

Heinke et al. (2006) estimated the radius of a neutron star in a quiescent low mass X-ray binary X7 which resides in the globular cluster 47 Tucanae. Their atmosphere model fits to the X-ray spectrum, obtained with the *Chandra* satellite, result in a radius of $14.5_{-1.6}^{+1.8}$ km if the star has a mass of $1.4 M_{\odot}$ or if they assume a radius of 10 km, the mass of the star is found as $2.20_{-0.16}^{+0.03} M_{\odot}$, again puts challenge on soft equations of state (Heinke et al., 2006).

Webb & Barret (2007) observed three neutron stars in quiescent X-ray binaries located in globular clusters with *XMM-Newton*. Using the same method as in Heinke et al. (2006), they report a radius lower limit as 8 km and a mass upper limit as $2.4 M_{\odot}$ (Webb & Barret, 2007).

Özel and her colleagues devoted serious effort in a series of papers to constrain the masses and radii of six neutron stars residing in binary systems which have shown thermonuclear X-ray bursts with photospheric radius expansion. The lower limits on the mass and radius of the star in EXO 0748-676 are $M \geq 2.10 \pm 0.28 M_{\odot}$, $R \geq 13.8 \pm 1.8$ km (Özel, 2006). However, these limits were shown to be invalid due to the implausibility of the origin of the absorption lines that were thought to be coming from the photosphere of the star (Lin et al., 2010). For the neutron star in EXO 1745-248, Özel et al. (2009) presented two solutions: one with $M = 1.4 M_{\odot}$, $R = 11$ km and the other with $M = 1.7 M_{\odot}$, $R = 9$ km. Masses and radii of the stars in 4U 1608-52 and 4U 1820-30 were reported as $M = 1.74 \pm 0.14 M_{\odot}$, $R = 9.3 \pm 1.0$ km and $M = 1.58 \pm 0.06 M_{\odot}$, $R = 9.1 \pm 0.4$ km, respectively (Güver et al., 2010a,b). Özel et al. (2012) reported upper limits on the mass and radius of the low mass X-ray binary KS 1731-260 as $M \leq 2.1 M_{\odot}$ and $R \leq 12.5$ km. Recently, Güver & Özel (2013) reported two solutions on the mass and radius of the neutron star in SAX J1748.9-2021: $M = 1.78 \pm 0.3 M_{\odot}$, $R = 8.18 \pm 1.62$ km and $M = 1.33 \pm 0.33 M_{\odot}$, $R = 10.93 \pm 2.09$ km. In conclusion, current observational studies with the highest possible accuracy on the radii of neutron stars imply a radius range of $9 < R < 12$ km as noted by Özel (2013).

1.1.2.2 Magnetic Fields

The magnetic field of a typical neutron star is simply thought to be enhanced via flux (Φ) conservation during the collapse of the progenitor star,

$$\Phi \sim \mathbf{B} \cdot \mathbf{A} = \text{constant}. \quad (1.8)$$

If a neutron star of $R \sim 10^6$ cm is formed from a progenitor star with a radius

$R \sim 10^{11}$ cm and magnetic field $B \sim 10^2$ G, then the magnetic field of the newly formed neutron star will be $\sim 10^{12}$ G. A rotating magnetized neutron star possesses a changing magnetic dipole moment and emits radiation (Pacini, 1967). Following Shapiro & Teukolsky (1983), the magnetic field strength of a neutron star can be estimated as follows: if the angle between the magnetic field and the rotation axis (see Figure 1.2) is α and the rotation frequency is Ω , the magnetic dipole moment is

$$\mathbf{m} = \frac{1}{2}BR^3(\sin \alpha \cos \Omega t \hat{\mathbf{i}} + \sin \alpha \sin \Omega t \hat{\mathbf{j}} + \cos \alpha \hat{\mathbf{k}}). \quad (1.9)$$

Here, B is the surface magnetic field at the magnetic pole of the star. The radiation from a magnetic dipole is given by Larmor's formula:

$$\dot{E} = -\frac{2}{3c^3}|\ddot{\mathbf{m}}|^2. \quad (1.10)$$

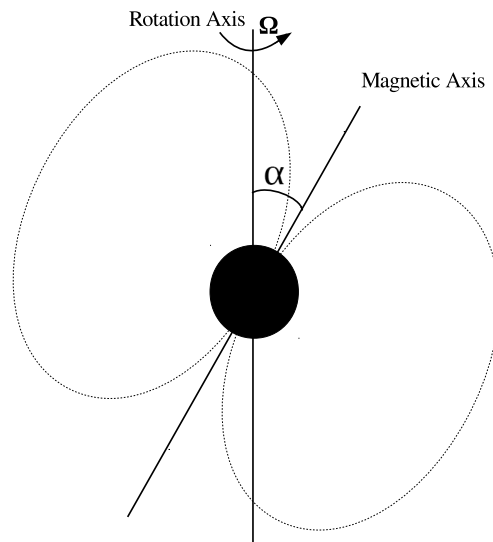


Figure 1.2: Schematic figure of a pulsar.

The energy loss rate at frequency Ω is then

$$\dot{E} = -\frac{B^2 R^6 \Omega^4 \sin^2 \alpha}{6c^3}. \quad (1.11)$$

The origin of this radiation is the rate of change of rotational kinetic energy of the star. Since the star is rotating with a frequency of Ω , it has a rotational kinetic energy:

$$E = \frac{1}{2}I\Omega^2, \quad (1.12)$$

where I is the moment of inertia of the neutron star ($I = (2/5)MR^2$ for a solid sphere. $I \sim 10^{45}$ g cm² for a typical neutron star.) and the rate of change of the kinetic energy is:

$$\dot{E} = I\Omega\dot{\Omega}. \quad (1.13)$$

Using Equations (1.11) and (1.13), we get an expression for the magnetic field in terms of the observable quantities:

$$B = \sqrt{\frac{6Ic^3}{R^6 \sin^2 \alpha}} \sqrt{\frac{-\dot{\Omega}}{\Omega^3}}. \quad (1.14)$$

We get the well-known magnetic field relation of a neutron star inferred from the period and period derivative as:

$$B = \sqrt{\frac{3Ic^3}{2\pi^2 R^6 \sin^2 \alpha}} \sqrt{P\dot{P}} = \frac{6.4 \times 10^{19}}{\sin \alpha} \sqrt{P\dot{P}} \text{ G}. \quad (1.15)$$

For a typical young pulsar spinning down via magnetic dipole braking, the magnetic field strength is of the order of $\sim 10^{12}$ G. As calculated from observed values of periods and spin-down rates, magnetic fields of pulsars range from 10^8 to 10^{15} G (see, e.g., Manchester et al., 2005).

The only way of directly measuring the magnetic field of a neutron star is by observing a cyclotron line in its spectrum. Cyclotron lines originate from the transition of electrons between quantized energy levels after scattering with X-ray photons in a highly magnetized plasma (Mészáros, 1992). The first cyclotron lines were observed from accreting X-ray pulsars Her X-1 and 4U 0115+63, indicating a field strength of $\sim 5 \times 10^{12}$ G (Trümper et al., 1978; Wheaton et al., 1979). After the launches of HEXE instrument, *GINGA* and *RXTE* satellites, cyclotron lines from a dozen of neutron stars observed at energies 10–100 keV were measured (see, e.g., Heindl et al., 2004; Caballero & Wilms, 2012, and references therein), all suggesting a magnetic field on the order of $\sim 10^{12}$ G. Recently, Tiengo et al. (2013) reported detection of a cyclotron feature in the X-ray spectrum of SGR 0418+5729 which implies a magnetic field strength higher than 10^{14} G.

1.1.2.3 Rotation Periods and Period Derivatives

Rotation periods of pulsars range from milliseconds to hundreds of seconds. The very long period pulsars, i.e. $P \sim 10^3$ s, which are thought to be accreting from a companion star (see, e.g., Ikhshanov, 2007) and in general all accreting pulsars will not be discussed here. The shortest period detected until now is 1.4 ms (Hessels et al., 2006) and the longest period is 11.8 s (Vasisht & Gotthelf, 1997). Rotation

periods are observed to increase steadily except during the sudden spin-up events, i.e. ‘*glitches*’. The changes in the rotation period range from 10^{-21} to 10^{-10} s s^{-1} (Manchester et al., 2005).

Apart from the surface magnetic field strengths, we can deduce information on the age of the pulsar and deviations from pure dipole field via observations of its period and its change in time.

From Equations (1.11) and (1.13) we get $\dot{\Omega}$ as

$$\dot{\Omega} = -\frac{B^2 R^6 \sin^2 \alpha}{6Ic^3} \Omega^3. \quad (1.16)$$

In Equation (1.16), the exponent of Ω (which is 3) indicates the torque mechanism on the star. In this case, it is a pure dipole with a constant dipole moment. In general, slow-down rate is given by the relation

$$\dot{\Omega} \propto -\Omega^n, \quad (1.17)$$

where n is called the braking index. Taking the time derivative of this equation and arranging it to get the n , results in;

$$n = \frac{\Omega \ddot{\Omega}}{\dot{\Omega}^2}. \quad (1.18)$$

For the sources for which $\ddot{\Omega}$ is also measured, the braking index can be calculated. Due to the observational constraints it is hard to determine higher order derivatives of Ω . Measurements of more steady rotating pulsars, i.e. highest accurate measurements, resulted in braking indices of less than 3 (see, e.g., Livingstone et al., 2007; Espinoza et al., 2011), suggesting deviations from a pure dipole field. Besides that, the range of braking indices is very large even for the longest observed pulsars (Hobbs et al., 2010).

Now, from Equation 1.17 we can estimate the age of the star which has an initial angular velocity Ω_0 . Integration of Equation 1.17 results in

$$\tau = -\frac{\Omega}{(n-1)\dot{\Omega}} \left[1 - \left(\frac{\Omega}{\Omega_0} \right)^{n-1} \right]. \quad (1.19)$$

τ is the characteristic age of the pulsar. If the star is initially spinning much faster than the current value, Ω , and if $n = 3$, characteristic age is simply given as:

$$\tau = -\frac{\Omega}{2\dot{\Omega}} = \frac{P}{2\dot{P}}. \quad (1.20)$$

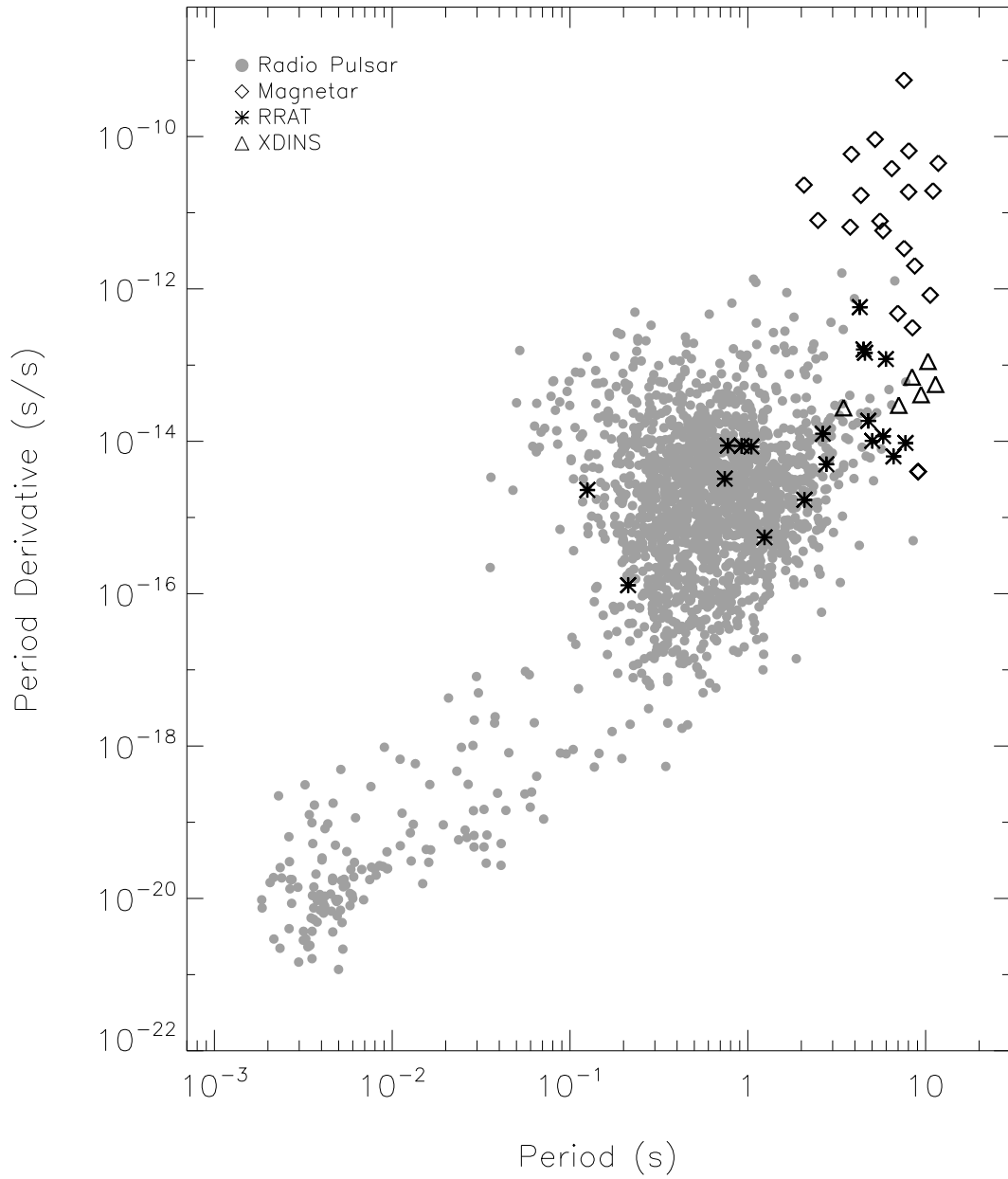


Figure 1.3: Period-period derivative diagram. Light gray dots represent radio pulsars. Magnetars are shown with diamonds. Rotating Radio Pulsars (RRAT) and X-ray Dim Isolated Neutron Stars (XDINS) are shown with star and triangle symbols, respectively. The data were taken from ATNF pulsar catalogue (Manchester et al., 2005) (<http://www.atnf.csiro.au/people/pulsar/psrcat/>). The period derivative of SGR 0418+5729 is taken from Rea et al. (2013).

1.1.2.4 Magnetosphere

Until now we have assumed that pulsars are rotating in vacuo. However, Deutsch (1955) and Goldreich & Julian (1969) showed that electric fields parallel to the surface of a magnetized star are strong enough to pull out particles from the surface and form a magnetosphere filled with plasma.

For a perfect conductor we can find the electric field inside the star and using boundary conditions on the tangential and normal components of electric field we can find the electrostatic potential: Following Griffiths (1999), the current density \mathbf{J} is proportional to the force per unit charge \mathbf{f} : $\mathbf{J} = \sigma\mathbf{f}$. The proportionality constant is called the conductivity of the medium. If the charges are driven by the electromagnetic force, then the current density is given by Ohm's law: $\mathbf{J} = \sigma(\mathbf{E} + \mathbf{v}/c \times \mathbf{B})$. For a perfect conductor σ is infinitely large and Coulomb force vanishes, i.e. $\mathbf{J}/\sigma = 0$, then the equation becomes

$$\mathbf{E} + \frac{\mathbf{v} \times \mathbf{B}}{c} = 0. \quad (1.21)$$

Following Goldreich & Julian (1969) and Shapiro & Teukolsky (1983), the electric field inside a perfectly conducting neutron star rotating with angular velocity Ω is given using Equation 1.21 as

$$\mathbf{E}^{\text{in}} + \frac{(\boldsymbol{\Omega} \times \mathbf{r})}{c} \times \mathbf{B}^{\text{in}} = 0. \quad (1.22)$$

Here \mathbf{B}^{in} is the dipole magnetic field at $r = R$:

$$\mathbf{B}^{\text{in}} = B \left(\cos \theta \hat{\mathbf{r}} + \frac{\sin \theta}{2} \hat{\boldsymbol{\theta}} \right). \quad (1.23)$$

Goldreich & Julian (1969) calculated the electric field, assuming that rotational and magnetic axes are aligned, i.e. aligned rotator. If this axis is the z axis, then $\boldsymbol{\Omega} = \Omega \hat{\mathbf{z}}$ and the electric field inside the surface is

$$\mathbf{E}^{\text{in}} = \frac{\Omega R B \sin \theta}{c} \left(\frac{\sin \theta}{2} \hat{\mathbf{r}} - \cos \theta \hat{\boldsymbol{\theta}} \right), \quad (1.24)$$

and $\mathbf{E} \cdot \mathbf{B} = 0$ inside the star. Goldreich & Julian (1969) continued with the assumption that there are no charges outside the star, i.e. $\nabla \cdot \mathbf{E} = 0$. Boundary condition on the tangential component of the electric field states that it is continuous at the stellar surface. So, solution of the Laplace's equation gives an electrostatic potential outside the star as

$$\Phi = -\frac{B\Omega R^5}{6cr^3} (3 \cos^2 \theta - 1) \quad (1.25)$$

(Goldreich & Julian, 1969). Outside the star the electric field has a component

parallel to the magnetic field. The strength of this component is high enough to rip off particles from the surface of the star:

$$E_{\parallel} = -\frac{\Omega R}{c} B \sim 2 \times 10^8 \left(\frac{P}{s}\right)^{-1} \left(\frac{B}{10^{12} \text{ G}}\right) \text{ V cm}^{-1} \quad (1.26)$$

(Shapiro & Teukolsky, 1983) which is orders of magnitude greater than the gravitational force on the surface of the star. Goldreich & Julian (1969) concluded that a vacuum solution for a pulsar is unstable. In the plasma-filled magnetosphere, electric field component parallel to the magnetic field is screened by the plasma ($\mathbf{E} \cdot \mathbf{B} = 0$) and plasma corotates with the star within a radius where the rotation speed reaches the speed of light, therefore, the radius of the light cylinder is calculated as

$$R_{LC} = \frac{c}{\Omega} = 4.77 \times 10^4 \left(\frac{P}{s}\right) \text{ km.} \quad (1.27)$$

Field lines beyond the light cylinder cannot be closed, otherwise particles moving along these lines would move faster than the speed of light. The surface region of the star where open field lines emerge is called the magnetic polar cap region. A description of an aligned pulsar has been given by Goldreich & Julian (1969) (see Figure 1.4). Charge density of the magnetosphere inside the light cylinder is

$$\rho = \frac{1}{4\pi} \nabla \cdot \mathbf{E} = -\frac{1}{4\pi c} \nabla \cdot [(\boldsymbol{\Omega} \times \mathbf{r}) \times \mathbf{B}] = -\frac{\boldsymbol{\Omega} \cdot \mathbf{B}}{2\pi c} = -\frac{\Omega B_z}{2\pi c}, \quad (1.28)$$

and the number density is

$$n = \frac{\rho}{e} = 7 \times 10^{-2} B_z P^{-1} \text{ particles cm}^{-3} \quad (1.29)$$

which is called the Goldreich-Julian density (Goldreich & Julian, 1969).

1.1.3 Emission Mechanisms

The number of pulsars observed in the radio band has increased significantly over recent years owing to large pulsar surveys⁴ (Manchester et al., 2005). Only six pulsars were previously observed emitting in gamma-rays with observations done by *CGRO*/EGRET (Hartman et al., 1999). After the launch of *Fermi* satellite (see §1.4) in 2008, many new pulsars which are only seen in gamma-ray band have been observed (Abdo et al., 2013). Although there are significant efforts to explain their emission mechanisms, the issue is still not resolved completely.

Deutsch (1955) and Goldreich & Julian (1969) suggested that the electric field near a magnetized star can have a component parallel to the magnetic field ($\mathbf{E} \cdot \mathbf{B} \neq 0$) and accelerate particles to high energies. However, this is achieved if there are low

⁴<http://www.atnf.csiro.au/people/pulsar/psrcat/>

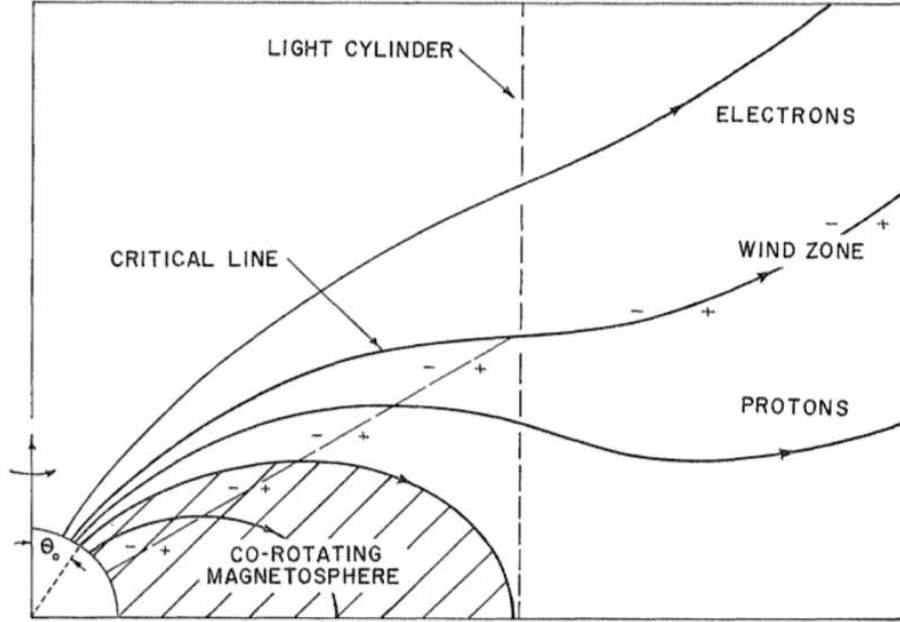


Figure 1.4: Pulsar magnetosphere model of Goldreich & Julian (1969). Figure is taken from Goldreich & Julian (1969).

density regions or vacuum gaps in the magnetosphere of the star (Deutsch, 1955). Such regions, such as polar cap, slot gap and outer gap, have been proposed to exist in the pulsar magnetosphere (Sturrock, 1971; Ruderman & Sutherland, 1975; Arons, 1979; Cheng et al., 1986a). According to the model developed by Sturrock (1971), radio emission from pulsars is explained via accelerated particles streaming from polar caps due to large electric fields. These particles, flowing along the open field lines, emit curvature radiation which is observed as gamma-rays. In the presence of a strong magnetic field, interaction of these gamma-rays with the field creates electron-positron pairs. These pairs produce curvature radiation as well as secondary pairs, generating a pair cascade which emits coherent radiation in the radio regime of the spectrum (Sturrock, 1971). However, this model neglects the screening of the parallel component of the electric field by the pairs. Ruderman & Sutherland (1975) proposed that ions are tightly bound to the surface and cannot be ripped off and eventually, due to the absence of positive ions (in a counteraligned pulsar) from the surface, outflow of electrons from the light cylinder cannot be balanced, forming a gap with a height of 10^4 cm in the magnetosphere. This gap discharges when the potential difference across the gap reaches 10^{12} V and generates electron-positron pairs. These pairs are accelerated inside the gap due to the parallel component of the electric field, emit curvature radiation and generate a pair cascade. Electrons are accelerated towards the surface and positrons away from the surface. Although positrons will not be accelerated significantly outside the gap, they emit curvature radiation following open field lines and generate pair cascades resulting in coherent

radio emission as in the Sturrock model (Ruderman & Sutherland, 1975).

Gamma-ray emission in polar gap models are observed when the photons with insufficient energy to produce pairs escape from the magnetosphere. Calculations of Salvati & Massaro (1978) indicated that synchrotron emission from secondary pairs contribute to the pulsar’s gamma-ray emission significantly. Numerical simulations by Daugherty & Harding (1982) supported these calculations, indicating polar gaps have the potential to explain high-energy emission from pulsars.

Arons (1979) investigated radiation from an oblique rotator with $\boldsymbol{\Omega} \cdot \mathbf{B} > 0$, so that electrons are ripped off from the surface. He proposed that the particle acceleration takes place in a slot gap, which is the region bounded by the last closed field lines and open field lines which bend toward the rotational axis of the star. Due to the curvature of the magnetic field lines charge density differs from the Goldreich-Julian density (see Equation 1.29) along the field lines; a potential difference occurs and particles accelerate which results in pair formation process within a height of 1–2 km (Arons, 1981). Unlike Ruderman & Sutherland (1975) they assume the binding of ions and electrons are negligible. Once the pair formation process starts, acceleration stops at a thin layer which they call pair formation front.

Cheng et al. (1986a,b) suggested another gap that resides in the outer magnetosphere near the null surface, i.e. the surface which separates positive and negative charges ($\boldsymbol{\Omega} \cdot \mathbf{B} = 0$). In the negative charge region, charges leave the magnetosphere and form a negative charge-depleted region. This charge-depleted region acts as a positively charged region and repels the positive charge region residing on the other side of the null surface. This process forms a gap and ignites pair creation when the potential drop is sufficiently large. In the outer gap region, the magnetic field is much weaker which enables the generation of significant potential drop so that curvature radiation, inverse Compton scattering or synchrotron radiation can produce high-energy photons (Cheng et al., 1986a).

1.1.3.1 Structure

Density in a neutron star changes by several orders of magnitude from the atmosphere to the core (see Figure 1.5). Its structure is generally described in five characteristically different parts.

The outermost layer is the atmosphere which is a thin layer with a thickness smaller than 1 cm and density of $1\text{--}10 \text{ g cm}^{-3}$ (Romani, 1987; Miller, 1992). Details of this layer (e.g., composition, magnetic field strength, conductivity) are very important for the understanding of the emerging spectrum and, is still an active research area (see, e.g., Ho & Heinke, 2009; Suleimanov et al., 2014).

The second part is the outer crust. The outer crust is thought to be solid, composed of electrons and fully ionized iron nuclei arranged in a lattice with density

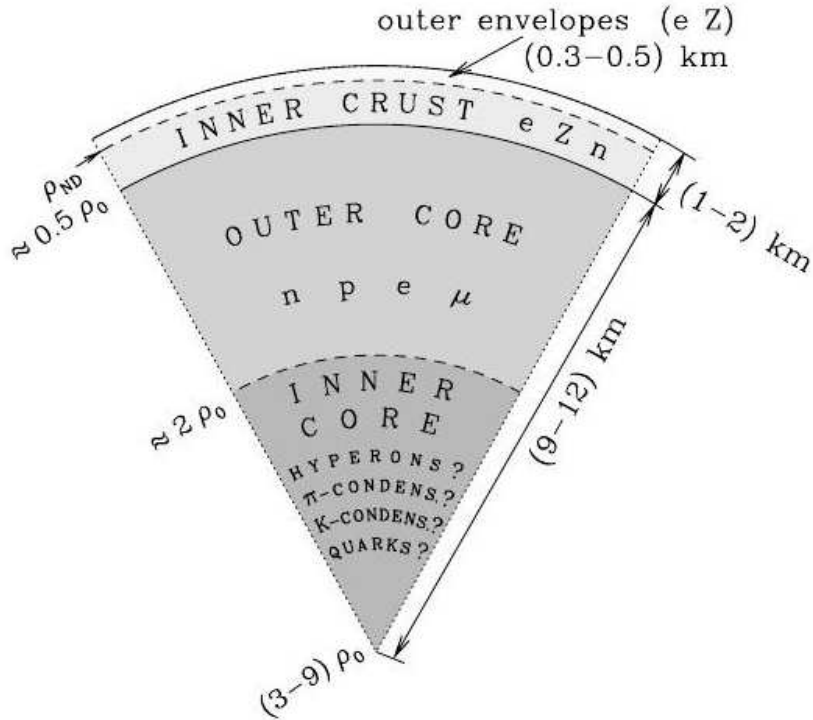


Figure 1.5: Neutron star structure. $\rho_{ND} = 4.3 \times 10^{11} \text{ g cm}^{-3}$ is the neutron drip density and $\rho_0 = 2.8 \times 10^{14} \text{ g cm}^{-3}$ is the nuclear matter saturation density. Figure is taken from Haensel et al. (2007).

ranging from 10^4 g cm^{-3} to $4.3 \times 10^{11} \text{ g cm}^{-3}$ (i.e. neutron drip density, ρ_{ND}) (Ruderman, 1968, 1969; Baym et al., 1971b). Electrons become relativistic above 10^7 g cm^{-3} and are captured by the nuclei and produce neutron rich nuclei via inverse beta decay.

The inner crust is the region where density becomes high enough for neutrons to start dripping out of the nucleus. At densities up to $2 \times 10^{14} \text{ g cm}^{-3}$ lattice of nuclei, free neutrons and electrons exist together which is called free-neutron regime (Langer et al., 1969; Baym et al., 1971a,b). In this region, both free neutrons and bound neutrons are considered to be superfluid (Migdal, 1959; Ginzburg & Kirzhnits, 1965). This idea was supported by observations of glitch phenomena (see §1.1.4). Although the thickness of the crust (outer+inner) depends on the equation of state, it constitutes approximately 10 percent of the star's radius (see, e.g., Haensel et al., 2007). For recent and extensive reviews on the properties of the neutron star crust see Haensel et al. (2007) and Chamel & Haensel (2008).

The vast majority of the neutron star's mass is in the core which is also the thickest part of the star, 9–12 km depending on the equation of state (Haensel et al., 2007). It is separated into two parts: the outer core and inner core. In the outer core density reaches the nuclear saturation value (ρ_0), $2.8 \times 10^{14} \text{ g cm}^{-3}$, and nuclei dissolve completely (Baym et al., 1971a). Matter in this region is mostly

composed of neutrons while a small number of protons, electrons and muons exist (Baym et al., 1971a). This part extends up to a density of $2\rho_0$ and its details were investigated by e.g., Oppenheimer & Volkoff (1939), Baym et al. (1971a) and Pandharipande & Smith (1975).

The inner core density is higher than $2\rho_0$ and can increase by an order of magnitude larger than ρ_0 towards the center (Baym et al., 1971a). The state of the matter at the inner core is uncertain: existence of meson condensate, hyperonic matter, quark matter and solid core are proposed (Cameron, 1959; Bahcall & Wolf, 1965; Ivanenko & Kurdgelaidze, 1969; Pandharipande, 1971; Bethe & Johnson, 1974; Migdal, 1971; Iachello et al., 1974). Haensel et al. (2007) present a detailed review of the inner structure of neutron stars.

1.1.4 Glitches

Glitches are sudden increases in the rotation frequency of pulsars followed with sudden changes in their spin-down rates. These events provide invaluable information on their internal structure. Glitches were first detected from the Crab and Vela pulsars through timing observations (see, e.g., Richards & Comella, 1969; Radhakrishnan & Manchester, 1969). Since then, more than 400 glitches have been observed from 150 pulsars (Jodrell Bank Observatory glitch catalogue⁵; Espinoza et al., 2011; Yu et al., 2013). Pulsar glitches are not accompanied by radiative events, such as variations in spectral properties or flux level (but see Weltevrede et al., 2011). Therefore, the proposed glitch models involve dynamical variations in the neutron star interior instead of an external mechanism. The size of the glitch (commonly measured with $\Delta\nu/\nu$) typically reflects the underlying internal dynamics of the neutron star: small size glitches ($\Delta\nu/\nu \sim 10^{-9}$, aka. Crab-like glitches) are explained by the decrease of the moment of inertia of the pulsar due to starquakes (Ruderman, 1969; Baym & Pines, 1971). Starquake model has problems in explaining the large size glitches ($\Delta\nu/\nu \sim 10^{-6}$, aka. Vela-like glitches) with an occurrence frequency of few years due to implausibility of storing enough energy in the crust to power these events (Baym & Pines, 1971). Thus, large size glitches are described as the angular momentum transfer from inner crust neutron superfluid to the crust by the sudden unpinning of the vortices which are pinned to the inner crust nuclei (Anderson & Itoh, 1975; Alpar et al., 1984a,b). Below we explain these two models.

1.1.4.1 Vortex Unpinning Model

Some materials exhibit zero electrical resistance when cooled below a critical temperature. This phenomenon is called superconductivity. The physical explanation

⁵<http://www.jb.man.ac.uk/pulsar/glitches.html>

of superconductivity is given by Bardeen et al. (1957). In their theory, i.e. Bardeen-Cooper-Schrieffer (BCS) theory, electrons (or in general fermions) form pairs below a critical temperature so that they behave like bosons and are strongly biased to share the same quantum state. In 1938 another phenomenon which is similar to the physics of superconductivity was discovered; flow of a fluid with zero viscosity, i.e. superfluidity (Kapitza, 1938; Allen & Misener, 1938). Existence of superfluid matter was suggested in the neutron stars (Migdal, 1959; Ginzburg & Kirzhnits, 1965). In these stars neutrons can form superfluid and rotational properties of the superfluid have been very important in understanding the glitches and their relaxation times (Baym et al., 1969; Anderson & Itoh, 1975; Alpar, 1977). A superfluid, if it rotates at a certain angular velocity range, a criterion which is satisfied by neutron stars (Baym et al., 1969), forms quantized swirling structures parallel to the spin axis, i.e. vortex lines (Onsager, 1949; Feynman, 1955), These vortices may pin to the neutron-rich nuclei (pinning centers) in the inner crust (Anderson & Itoh, 1975; Alpar, 1977). In a steady state, the superfluid slows down at the same rate with the crust only by moving vortices radially outward between pinning centers, a process which is called vortex creep (Alpar et al., 1984b). In some regions, the pinned vortices may retain their angular velocity as long as a critical rotational lag between the superfluid and the crust grows ($\delta\Omega \equiv \Omega_s - \Omega_c$, where Ω_s and Ω_c are the angular velocities of the superfluid and crust, respectively) (Anderson & Itoh, 1975). This critical rotational lag builds up due to the competing forces which pin vortices to the nuclei and which push them outwards (Alpar, 1977). Above the critical value vortices suddenly unpin, move outwards and transfer angular momentum to the crust, i.e. glitch (Anderson & Itoh, 1975). The later observed relaxation epoch is explained as the reconstruction of the steady state (Alpar et al., 1984a,b). This model is successful in explaining the large glitches ($\Delta\nu/\nu \sim 10^{-6}$, such as those observed from the Vela pulsar) with an occurrence time of ~ 2 yr (Alpar et al., 1981, 1984a). On the other hand, this model predicts higher glitch occurrence frequency for the young pulsars (i.e. Crab pulsar) than the observed frequencies (Alpar et al., 1996). Thus, Alpar et al. (1996) proposed that vortex unpinning can be triggered by starquakes instead of reaching a critical rotational lag and the following relaxation period can be explained by the motion of vortices to the new vortex trap regions and formation of vortex depletion regions in these pulsars (Alpar et al., 1996).

1.1.4.2 Starquake Model

Neutron stars start their lives with an oblate shape due to their high angular velocity (Ruderman, 1969). Gradual spin-down of a neutron star due to the external forces reduces the oblateness of the star which stresses the solid crust (Ruderman, 1969; Baym & Pines, 1971). When the elasticity of the crust reaches a critical strain

value the solid crust cracks which changes the moment of inertia of the crust, thus leading to a glitch (Ruderman, 1969). Srinivasan et al. (1990) and Ruderman et al. (1998) proposed that variations in the core magnetic field due to the motion of core superfluid vortices coupled to it can also cause fractures. Another crust cracking mechanism is the diffusion of the magnetic field in the cores of strongly magnetized stars, i.e. magnetically driven quakes (Thompson & Duncan, 1996; Rheinhardt & Geppert, 2002). This model is successful in explaining small size glitches ($\Delta\nu/\nu \sim 10^{-9}$) such as seen in the Crab pulsar.

1.2 Magnetars

1.2.1 General Properties

Anomalous X-ray pulsars (AXPs) have rotation periods in the range of 2–12 s and they spin down relatively fast with spin down rates spanning 10^{-12} – 10^{-10} s s⁻¹ (see, e.g., Mereghetti, 2013; Dib & Kaspi, 2014, and Figure 1.3). They are bright X-ray sources with X-ray luminosities ranging from 10^{33} to 10^{36} erg s⁻¹ in energies below 10 keV and most of them exhibit episodic burst events (see, e.g., Rea & Esposito, 2011; Mereghetti, 2011, 2013, for recent reviews). Their periods and period derivatives (see Equation 1.20), and for some of them, their association with supernova remnants, imply that they are young systems. Their observed X-ray luminosities cannot be explained by a rotational energy loss as for rotationally powered pulsars and by the accretion from a companion due to the lack of any evidence for binary nature (Hulleman et al., 2001; Wang et al., 2007).

Soft gamma-ray repeaters (SGRs) emit recurrent bursts in the hard X-ray and soft gamma-ray bands. Initially AXPs and SGRs were thought to be two separate classes. After the observation of bursts in AXP 1E 1048.1-5937 (Gavriil et al., 2002), an outburst in AXP 1E 2259+586 (Kaspi et al., 2003), and now from many AXPs, there is strong evidence that they represent a single class named magnetars: sources powered by the decay of extremely strong magnetic field (Duncan & Thompson, 1992) (see §1.2.2.1). Currently there are 13 AXPs (11 confirmed, 2 candidates) and 13 SGRs (10 confirmed, 3 candidates) (Olausen & Kaspi, 2014).

1.2.2 Theoretical Models

There are mainly four models suggested to explain the unusual properties of these sources. The first and more comprehensive model is the magnetar model (Thompson & Duncan, 1995, 1996). In this model the decay of their extremely high magnetic field has been proposed to be the source of their X-ray power. The second model is

the fallback disk model which suggests that the star is powered by the gravitational energy of the accreted matter from a fallback disk (Alpar, 1999; Chatterjee et al., 2000; Alpar, 2001). The quark star model proposes that these stars are not composed of neutrons but quarks (Horvath, 2007; Xu, 2007). The last model suggests that AXPs and SGRs are fast-rotating massive, strongly-magnetized white dwarfs (Paczynski, 1990; Usov, 1993). Here, the magnetar model and fallback disk model will be described in detail.

1.2.2.1 The Magnetar Model

Duncan & Thompson (1992) proposed that neutron stars can possess extremely high magnetic dipole fields, which can be higher than the quantum electrodynamics field limit:

$$B_{QED} = \frac{m_e^2 c^3}{e \hbar} = 4.4 \times 10^{13} \text{ G}, \quad (1.30)$$

and even stronger internal fields that makes the stored energy in the magnetic field dominate the rotational energy of the star. Such strong magnetic field strengths can be achieved by a dynamo mechanism just after the collapse of the progenitor star while the star is highly convective and rotates fast enough to operate as an efficient dynamo (Duncan & Thompson, 1992; Thompson & Duncan, 1993). In the magnetar model the decay of the magnetic field through mechanisms such as ambipolar diffusion, which is the main process in the core, Ohmic diffusion and Hall drift in the crust can extract enough energy to power and spin-down the star on the magnetar timescale ($\sim 10^4$ yr) (Thompson & Duncan, 1996).

The quiescent X-ray luminosity due to diffusive processes is (Thompson & Duncan, 1996):

$$L_X(t) = 5 \times 10^{34} \left(\frac{t}{10^4 \text{ yr}} \right)^{-0.32} \left(\frac{R}{10^6 \text{ cm}} \right)^2 \text{ ergs s}^{-1}, \quad (1.31)$$

where t is the age of the pulsar. On the other hand, diffusion driven stresses can cause fractures in the crust if the crustal field strength is in the range (Thompson & Duncan, 1996):

$$(4\pi\mu\Theta_{max})^{1/2} < B < (4\pi\mu)^{1/2}, \quad (1.32)$$

where Θ_{max} is the maximum yield strain and μ is the shear modulus of the crust. The fractures in the crust causes an instability which leads to the displacement of magnetic field lines that are attached to the crust (Thompson & Duncan, 1995). In magnetar model, this displacement of field lines causes Alfvén waves with velocities close to the speed of light in the magnetosphere which leads to typical bursts seen

in magnetars, and larger displacements of the magnetic footpoints are caused by large scale rearrangement of the strongly twisted core magnetic field (Thompson & Duncan, 1995, 1996, 2001). A disturbance in the core moves with a velocity of (Thompson & Duncan, 1995)

$$v = 9 \times 10^6 \left(\frac{B}{10^{15} \text{ G}} \right) \left(\frac{\rho}{10^{15} \text{ g cm}^{-3}} \right)^{-1/2} \text{ cm s}^{-1} \quad (1.33)$$

through the star. Thompson & Duncan (1995) and Thompson et al. (2002) noted that the travelling time associated with this event is on the order of time scale of hard initial spikes of giant flares observed from magnetars (see, e.g., Mazets et al., 1979; Hurley et al., 1999, 2005). This disturbance causes fractures and twists in the crust patches, eventually resulting in reconnection events which lead to more energetic bursts, i.e. giant flares (Thompson & Duncan, 1995, 2001; Thompson et al., 2002). The energy injected to the magnetosphere through Alfvén waves can be trapped in the closed field lines which forms an optically thick photon-pair plasma, and the later seen soft tail of flares are explained as the cooling of this plasma (Thompson & Duncan, 1995).

The rotational motion of the crust patches due to the magnetic stresses can also induce twists in the external magnetic field (Thompson et al., 2000, 2002). According to this model a twisted magnetosphere can lift the charges from the surface and maintain large scale currents. The impact of the charged particles heats the surface and emits X-ray photons, thus enhances persistent X-ray emission; if the field is twisted by 1 rad, the persistent X-ray emission in this scenario is given by

$$L_X = 1.5 \times 10^{35} \left(\frac{B}{10^{14} \text{ G}} \right) \left(\frac{M_{NS}}{1.4 M_\odot} \right) \text{ ergs s}^{-1} \quad (1.34)$$

(Thompson et al., 2002). Resonant Compton scattering of photons in the current carrying magnetosphere generates non-thermal emission observed from magnetars (Thompson et al., 2002). Furthermore, sudden relaxation of a gradual twist in the external magnetic field can supply enough energy to power a giant flare (Thompson et al., 2002).

In the magnetar model, glitches can be triggered by magnetic stresses rather than the spin-down of the pulsar. Sudden fractures in a highly magnetized star crust can cause disturbances in the crust that move with Alfvén velocity, and can lead to reaching critical velocity difference of the crust and superfluid for unpinning the vortex lines (Thompson & Duncan, 1993, 1996; Thompson et al., 2000). Thompson et al. (2000) also mention the possibility that giant flares can provide enough heat which increases the thermal vortex creep (see §1.1.4) and trigger a glitch.

1.2.2.2 The Fallback Disk Model

The fallback disk model (Alpar, 1999; Chatterjee et al., 2000; Alpar, 2001) assumes conventional dipole magnetic field strength for these stars, contrary to the magnetar model. Another assumption is that these sources have a disk which is formed by the remnant material from the supernova explosion, i.e. a fallback disk. The mass accretion rate is time-dependent and given by the relation (Chatterjee et al., 2000):

$$\dot{m} = \dot{m}_0 \left(\frac{t}{T} \right)^{-\alpha}, \quad (1.35)$$

where \dot{m}_0 is the accretion rate during the settling of the disk in a timescale of T . Chatterjee et al. (2000) showed that properties of the neutron star is determined by further evolution of the disk-star system governed by the location of the disk with respect to the Alfvén (R_A), corotation (R_c), and light cylinder (R_{LC}) (see Equation 1.27) radii (Chatterjee et al., 2000). We will summarize these evolution paths following Chatterjee et al. (2000): Inside the Alfvén radius, the flow of the infalling material is dominated by the magnetic field of the star; thus, disk cannot be closer to the star than R_m , where $R_m \approx 0.5R_A$, and matter is accreted along the field lines. If R_m is pushed beyond the light cylinder radius to where it cannot interact with the star, accretion stops and the star will be observed as an ordinary radio pulsar. If the star is rotating faster than the disk, i.e. $R_m \gg R_c$, it will transfer angular momentum to the disk and spin-down. This phase is called the *propeller phase* since the centrifugal forces will eject the matter before it falls onto the star. Due to the lack of accretion in this phase, the star will be faint in X-rays. Alpar (2001) suggested that XDINSs are neutron stars which are observed in this stage of the evolution. Towards the end of this phase as the star is spun-down significantly, the system approaches a steady accretion rate and an equilibrium period which is the period at which the disk corotates with the star, i.e. $R_m \sim R_c$. This period is given by the relation: (Frank et al., 2002; Alpar, 2001)

$$P = 16.8 \left(\frac{\dot{m}}{10^{15} \text{ g s}^{-1}} \right)^{-3/7} M^{-5/7} \left(\frac{\mu}{10^{30} \text{ G cm}^3} \right)^{6/7} \text{ s}, \quad (1.36)$$

where M and μ are the mass and magnetic moment of the star, respectively. In the *tracking phase*, the disk finally corotates approximately with the star. In this phase the disk accretes material and the star becomes X-ray bright. But the mass accretion rate is time dependent (see Equation 1.35) and decreasing, so is the brightness of the star. As the accretion rate decreases, the system enters another phase which is called advection-dominated flow (ADAF) and the star will have very low luminosity again.

In the fallback disk model magnetars are neutron stars observed in a time range

when their periods are close to the equilibrium period; more likely between their tracking and ADAF phases which also explains their observed narrow period ranges (Alpar, 1999; Chatterjee et al., 2000; Alpar, 2001).

Ertan et al. (2009) studied the evolution of magnetars with fallback disks in detail. They considered magnetars as the sources which are in their accretion phase with an efficient disk that causes the high spin-down rates and slow rotation periods of these stars. Their simulations in certain conditions showed that as the system evolves, X-ray luminosity of the star will diminish because of the decrease in the mass accretion rate and finally star will not be observable as a magnetar, naturally limiting the observed period range of these stars (Ertan et al., 2009).

Ertan & Çalıřkan (2006) showed that the optical and infrared emission from magnetars (see, e.g., Hulleman et al., 2000, 2001; Durant & van Kerkwijk, 2006) can be explained via emission from a disk. The X-ray and IR enhancements observed from some magnetars after their bursting episodes (Kaspi et al., 2003; Israel et al., 2003; Tam et al., 2004; Mazets et al., 1999) are explained by the evolution of the fallback disk affected by the burst (Ertan & Alpar, 2003; Ertan et al., 2006). Ekři & Alpar (2003) proposed that while the dipole field and fallback disk interaction evolves as explained above, the burst itself can be powered by magnetar like field strengths in the higher order multipoles.

So far, Wang et al. (2006) reported observation of a passive disk from a magnetar (4U 0142+61). Although they propose that the disk is passive, Ertan et al. (2007) showed that the optical and infrared observations of the source (Hulleman et al., 2000; Wang et al., 2006) can be explained with an active disk that is interacting with the star. Finally, a less robust observation of a disk from 1E 2259+586 in mid-infrared band was reported by Kaplan et al. (2009).

1.2.2.3 Emission Properties

All magnetars have been discovered as pulsating sources in the soft X-ray band. Their spectrum below 10 keV is modelled generally with blackbody plus power-law although there are implications that two blackbody fits are more feasible (Halpern & Gotthelf, 2005; Tiengo et al., 2008). There have been several attempts on modelling the soft X-ray spectra of magnetars with more physical models: Thompson et al. (2002) proposed that power-law tails in the X-ray spectra and changes in the pulse profiles of magnetars are produced by the resonant Compton scattering of the surface thermal photons by charged particles that are ejected to the magnetosphere as a result of the magnetic stresses applied to the crust by the twisted magnetic field inside the star. Lyutikov & Gavriil (2006) applied a semi-analytical version of this model to a magnetar with satisfying results. Güver et al. (2006) extended the work of Lyutikov & Gavriil (2006) including the effects of star's atmosphere based on

calculations of Özel (2001, 2003). Furthermore Güver et al. (2007) created a table model which also provides estimation of the magnetic field strength of the source. Güver et al. (2007) and Güver et al. (2008) presented their model fits to the spectra of two magnetars which are in good agreement with the data. Fernández & Thompson (2007) and Nobili et al. (2008a,b) explored the resonant Compton scattering in 3D Monte Carlo simulations. Modelling of magnetar spectra with resonant Compton scattering have been successful in explaining their soft X-ray spectrum (Lyutikov & Gavriil, 2006; Rea et al., 2008; Götz et al., 2009; Zane et al., 2009; Göğüş et al., 2011).

Magnetars that were in their bursting epochs were also observed to be emitting in the hard X-ray band. In 2004 non-thermal pulsed hard X-ray emission/soft gamma-ray emission from magnetars 1E 1841-045 (Molkov et al., 2004; Kuiper et al., 2004) 1RXS J170849.0-400910 (Revnivtsev et al., 2004) and 4U 0142+61 (den Hartog et al., 2004) (see Figures 1.6 and 1.7) was observed in their quiescent states. The spectrum of 1E 1841-045 extends up to ~ 150 keV with a power-law index of 1.39 ± 0.05 (Kuiper et al., 2008). 1RXS J170849.0-400910 was observed in the hard X-ray band during the Galactic Plane survey with *INTEGRAL* (Revnivtsev et al., 2004). Also, hard X-ray emission spectrum of 1RXS J170849.0-400910 extends up to ~ 175 keV with a power-law index 1.13 ± 0.06 and was shown to be pulsed up to 270 keV (den Hartog et al., 2008). 4U 0142+61 was discovered during *INTEGRAL* observations of the Cassiopeia region (den Hartog et al., 2004) and was observed to emit hard X-ray emission up to about 230 keV with a power law index of 0.93 ± 0.06 (den Hartog et al., 2008). The peak energy of the energy distribution is estimated as ~ 228 keV (see Figure 1.8) (den Hartog et al., 2008).

In the magnetar model crustal fractures lead to displacement of magnetic field lines which produces magnetohydrodynamic waves (Thompson & Duncan, 1995, 1996). Heyl & Hernquist (2005a,b) proposed that the energy injected to the magnetosphere through these waves can be dissipated via quantum electrodynamical processes and produce electron-positron pairs leading to the formation of a fireball and bursts. Furthermore they suggest that if the processes are not strong enough to yield an optically thick fireball, the produced non-thermal emission would be sufficient to explain the observed high-energy emission from magnetars with a spectral break lower limit of ~ 1 MeV. Thompson & Beloborodov (2005) and Beloborodov & Thompson (2007) explained the hard X-ray/soft gamma-ray emission as the cooling of a transition layer between the corona and the atmosphere which is heated by the corona. According to their calculations this emission is limited to ~ 1 MeV due to high magnetic field of the star. Another attempt to explain the hard X-ray emission was made by Baring & Harding (2007). They suggested that the upscattered surface thermal X-ray photons are the source of observed non-thermal hard X-ray

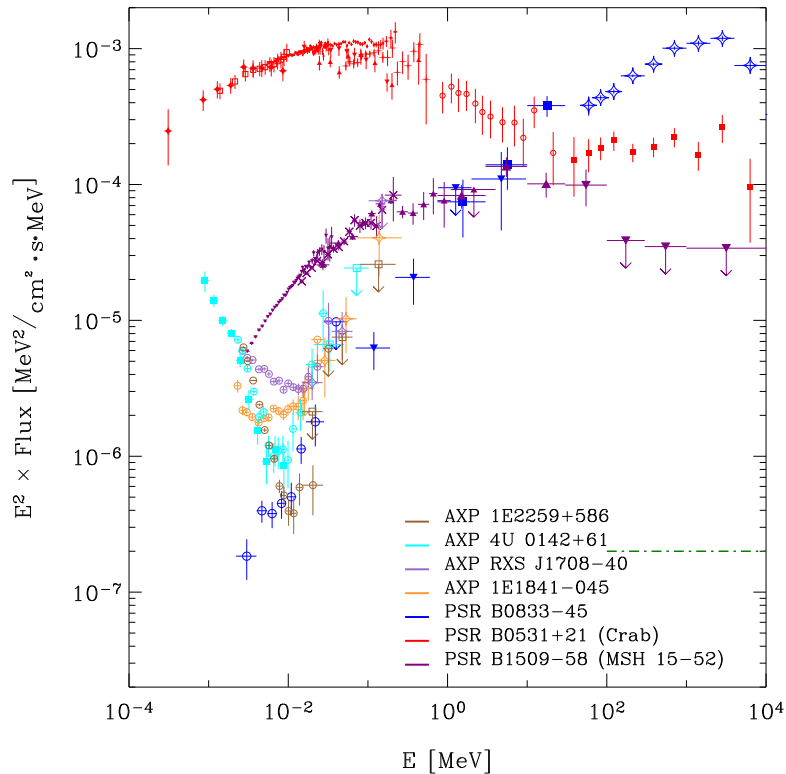


Figure 1.6: A wide band νF_ν spectrum of four AXPs: Spectra of two young radio pulsars, Crab and PSR B1509–58 and a middle-aged pulsar, Vela pulsar, are presented for comparison. Figure is taken from Kuiper et al. (2006).

emission from magnetars. These models have some problems in explaining the observed properties of hard X-ray emission which are discussed in detail in den Hartog et al. (2008).

In the context of fallback disk model, Trümper et al. (2010) proposed that hard X-ray emission originates from the bulk-motion Comptonization (BMC) of soft X-ray photons from the polar cap. They presented a BMC model fit result to the hard X-ray data of 4U 0142+61 which is in good agreement with the data in terms of fit statistics. The hard X-ray/gamma-ray emission will be discussed further in Chapter 2.

In contrast to normal pulsars, very few magnetars are observed in the radio band: SGRs 1806-20 and 1900+14 were observed in radio band only after their giant flares and no pulsations were observed (Frail et al., 1999; Gaensler et al., 2005; Cameron et al., 2005). Transient AXP XTE J1810-197 was the first AXP observed in radio band (Halpern & Gotthelf, 2005). Later on pulsed radio emission was observed from transient sources XTE J1810-197 and 1E 1547.0-5408 in connection with bursting activity (Camilo et al., 2006, 2007b) and from PSR J1622-4950 (indeed it was discovered as a pulsed radio emission source) without any evidence of bursting activity

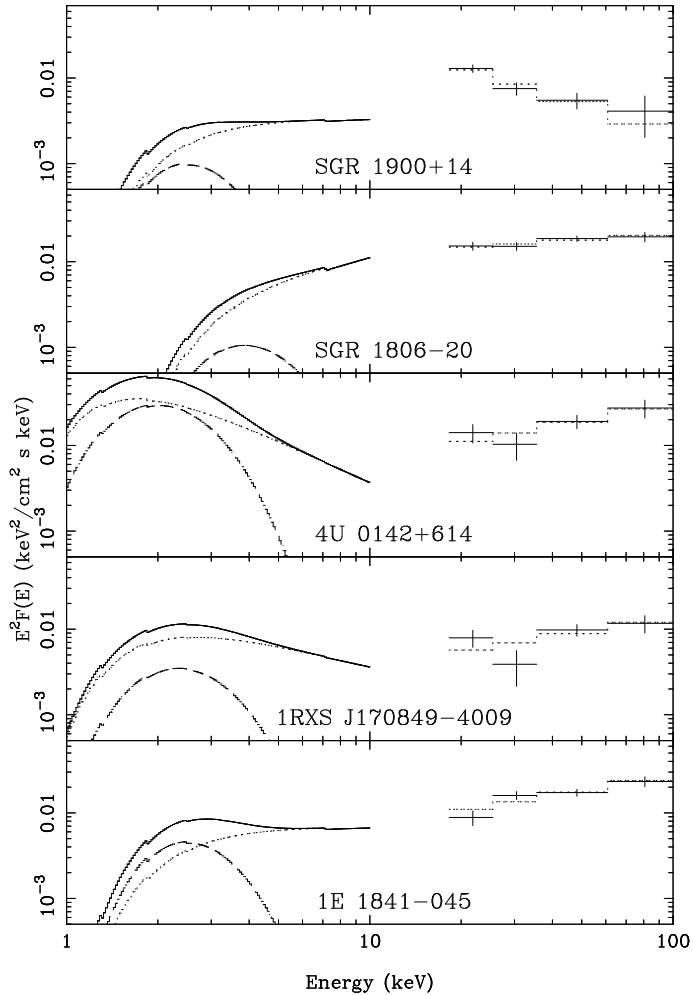


Figure 1.7: *INTEGRAL* detection of five magnetars above 18 keV. Dotted lines above 18 keV represent best fit power-law models. Blackbody (dashed lines) plus absorbed power-law (dotted lines) emission models below 10 keV are shown with solid lines. Figure is taken from Götz et al. (2006).

(Levin et al., 2010) although it may have been missed since further observations of the source exhibit diminishing X-ray flux (Anderson et al., 2012). Further searches in other magnetars did not yield any positive detection (Burgay et al., 2006; Lazarus et al., 2012). However, recently discovered SGR J1745-29 around Sagittarius A (Kennea et al., 2013) was observed to be emitting pulsed radio emission (Eatough et al., 2013; Spitler et al., 2014). Besides the rareness of the detection, their radio emission properties are also different than the normal pulsars. Spectral indices (α in flux density $S_\nu = \nu^\alpha$) of normal pulsars have an average of -1.8 ± 0.2 (Maron et al., 2000) while spectral indices of magnetars are ~ -0.5 or greater (Cameron et al., 2005; Camilo et al., 2006, 2007a). Their flux densities and pulse profiles also show higher variability than the normal pulsar standards (Camilo et al., 2007b,c, 2008; Levin et al., 2010). The mechanism for radio emission in normal pulsars is explained in §1.1.3. Burst related radio emissions from magnetars are explained by

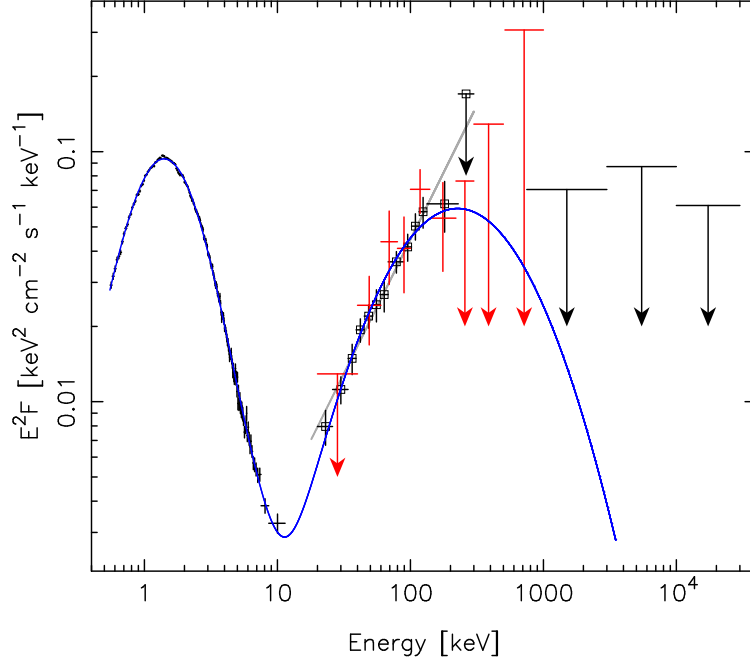


Figure 1.8: A wide band spectra of 4U 0142+61: *XMM-Newton* observations (0.55–11.5 keV) are shown in black. Black squares represent the *INTEGRAL*/ISGRI (20–300 keV) data, red open squares are *INTEGRAL*/SPI (20–1000 keV) data and black arrows represent the 2σ *CGRO*/COMPTEL (0.75–30 MeV) upper limits. Dashed line is the best fit power law model to the ISGRI data points and the blue curve is logparabola fit to the whole data (den Hartog et al., 2008). Figure is taken from den Hartog et al. (2008).

magnetic reconnection type events such as those observed in Solar flares (Lyutikov, 2002) and currents generated due to twisting/untwisting of magnetic field lines (Beloborodov, 2009). Rea et al. (2012) proposed that pulsed radio emission can be expected from magnetars with a high electric gap voltage and low X-ray efficiency in the quiescent state.

1.2.2.4 Glitches in Magnetars

RXTE observations of magnetars spanning more than a decade provided valuable information on the glitches of these sources. Although there are implications of timing anomalies from 1E 2259+586 (Usov, 1994; Baykal & Swank, 1996), glitch activity from a magnetar was first observed evidently from 1RXS J170849.0-400910 (Kaspi et al., 2000). Since then, glitches were observed from six magnetars (see, e.g., Kaspi et al., 2003; Dall’Osso et al., 2003; Woods et al., 2004; Morii et al., 2005; Israel et al., 2007b,a; Dib et al., 2008, 2009; Gavriil et al., 2011). Fractional glitch amplitudes ($\Delta\nu/\nu$) of these events range from 10^{-8} to 10^{-5} (Dib et al., 2009; İçdem et al., 2012) and fractional glitch derivative amplitudes ($\Delta\dot{\nu}/\dot{\nu}$) are between -0.1 and 1 (Woods et al., 2004; Dib et al., 2009).

Some of the magnetar glitches are observed to be accompanied by radiative variabilities (see, e.g., Kaspi et al., 2003; Israel et al., 2007a; Dib et al., 2009; Gavriil et al., 2011; Woods et al., 2011) although in conventional pulsars glitches are radiatively silent (except one outlier: see Weltevrede et al., 2011). On the other hand, 1RXS J170849.0-400910 and 1E 1841-045 have exhibited three unambiguous glitches without any evidence of radiative variability (Dib et al., 2008). Pons & Rea (2012) suggested that glitches in magnetars can indeed be related with radiative enhancements if they are caused by starquakes. They explain that the absence of enhancement detections in some sources can be due to their bright quiescent states and fast decay of the enhancements which make such detections difficult (Pons & Rea, 2012).

One of the magnetars, 1E 2259+586, recently showed a sudden decrease in its spin frequency (Archibald et al., 2013b), a few weeks after a hard X-ray burst (Foley et al., 2012). This was the first clear observation of an anti-glitch from a pulsar. This anti-glitch event was followed with a second event which is consistent with being a glitch or an anti-glitch event according to the analysis of Archibald et al. (2013b). A different approach applied to the data favored the anti-glitch explanation for the second event (Hu et al., 2014). The persistent X-ray emission of the source was observed to be doubled in conjunction with the anti-glitch (Archibald et al., 2013b). The normal glitches are usually explained with internal mechanisms operating in neutron stars, since they are not observed to be accompanied by radiative enhancements (e.g., Anderson & Itoh, 1975; Alpar, 1977). However, the observation of radiative events that are coincident with the anti-glitch of 1E 2259+586 (Archibald et al., 2013b) lead to rethinking of possible external mechanisms which involve magnetospheric processes (Lyutikov, 2013; Tong, 2014; Katz, 2014) and accretion processes (Katz, 2014; Ouyed et al., 2014; Huang & Geng, 2014). The anti-glitch event will be discussed in Chapter 4 in detail.

1.3 Thesis Outline

In this thesis, we investigated the high-energy gamma-ray spectral properties of AXP 4U 0142+61 and long-term temporal and X-ray properties of 1RXS J170849.0-400910 and 1E 1841-045.

The discovery of hard X-ray emission from magnetars (Molkov et al., 2004; Revnivtsev et al., 2004; den Hartog et al., 2004; Kuiper et al., 2004) opened new questions on the emission mechanisms of these sources. The mechanism of the hard X-ray emission has not been fully understood yet. Wide band spectrum of these sources are important in order to understand the nature of hard X-ray emission and assess the predictions of the existent theoretical models. With the launch of

Fermi satellite it became possible to investigate the high-energy gamma-ray emission from magnetars. In the first part of this thesis, we presented our results of a detailed search for the persistent and pulsed high-energy gamma-ray emission from 4U 0142+61 with the data obtained by Large Area Telescope (LAT) on board *Fermi*.

In the second part we focused on the long-term timing and X-ray emission properties of two magnetars, 1RXS J170849.0-400910 and 1E 1841-045, using the archival data from Rossi X-ray Timing Explorer (*RXTE*). Observations of glitches from magnetars are crucial to shed light on the glitch mechanisms, internal structure of magnetars and their similarities/distinctions from normal pulsar glitches. Another important information on the mechanism of glitches comes from the glitch recovery characteristics. More glitch observations, especially pre- and post-glitch observations, are important to distinguish the recovery characteristics. 1RXS J170849.0-400910 and 1E 1841-045 are important since they are observed to glitch frequently (Dib et al., 2008). Previous *RXTE* observations of these sources revealed three spin-up glitches from each source (Dib et al., 2008). We analyzed the subsequent *RXTE* observations of these sources spanning ~ 5 yr that is available until the end of the *RXTE* mission together with additional data from previous *RXTE* observations to maintain the continuity. Finally, we searched for glitches and radiative enhancements from these sources.

1.4 Instruments

In this section we give brief information on the satellites and their instruments from which the archive data we used in this study were collected. These satellites are *Rossi X-ray Timing Explorer (RXTE)* and *Fermi Gamma-ray Space Telescope (Fermi)*. Technical details on *RXTE* satellite and its instruments are compiled from XTE Technical Appendix (Appendix F)⁶, *RXTE Cookbook*⁷ and Jahoda et al. (2006). Details on *Fermi* and its instruments are compiled from Atwood et al. (2007, 2009) and Meegan et al. (2009).

RXTE was launched in December 1995 and operated for 16 years until it was shut down on January 2012. The *RXTE* satellite was built by NASA Goddard Space Flight Center in collaboration with University of California, San Diego and Massachusetts Institute of Technology. It orbited the Earth at an average altitude of 580 km with an inclination of 23° . It had three instruments on board: Proportional Counter Array (PCA), High-Energy X-ray Timing Experiment (HEXTE), and All-Sky Monitor (ASM) (see Figure 1.9).

The PCA has 5 identical units which are called proportional counter units

⁶<https://heasarc.gsfc.nasa.gov/docs/xte/appendix.f.html>

⁷<http://heasarc.nasa.gov/docs/xte/recipes/cook.book.html>

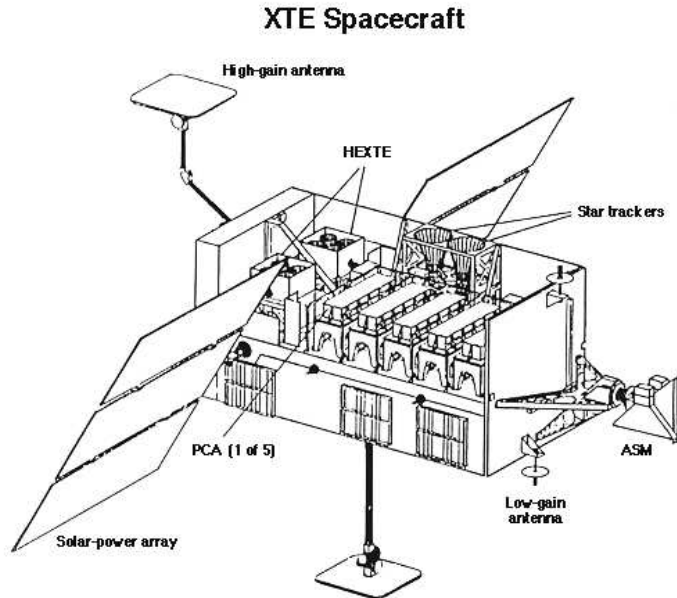


Figure 1.9: Schematic figure of *RXTE* and its instruments PCA, HEXTE and ASM. Figure is taken from http://heasarc.nasa.gov/Images/xte/xte_spacecraft.gif

(PCUs) operating in the 2–60 keV energy range with an energy resolution of 17% at 6 keV. It has a total effective area of $\sim 6000 \text{ cm}^2$ at 10 keV and a field of view (FOV) of $\sim 1^\circ$. Each unit is filled with 90 % Xenon and 10 % Methane gas. In a proportional counter detector, incident photons interact with the gas and produce electron-ion pairs as they move in the gas. In the final read-out the total number of electrons will be proportional to the energy of the incident photon. In each PCU, the gas filled region is divided into three layers so that it is possible to make layer selection. Selecting events only from the top Xenon layers increases the signal to noise ratio especially for faint sources. On top of the layers there is an anticoincidence layer, i.e. propane layer, which rejects charged particles and reduces the background level. Below the layers there is a Xenon veto layer which also acts as an anticoincidence layer. When an X-ray photon enters the PCU, it triggers an analog pulse that is amplified and converted to digital pulse height by the detector electronics. This is called an event. PCA has an Experiment Data System (EDS) interface to compress and analyze the events detected by PCUs with its parallel processing systems that are called event analyzers (EAs). EDS has 8 event analyzers, 2 system managers and 1 power distribution board. 6 of the EAs are for the analysis of the PCA data while 2 of them are for the ASM data. Each event analyzer for the PCA can run in 7 modes: Binned, pulsar fold, delta binned, event encoded, burst catcher, single-bit code, and fast Fourier transform mode. Each mode has configurations that can be chosen or defined according to the needs with a specified set of parameters. In this work we used event encoded mode which provides the time of every event, high

time resolution, PCU, layer and energy selection. Between available configurations we choose Good Xenon configuration which allows a temporal resolution of 1 microseconds. This configuration lists all events detected by the Xenon layers which are not rejected as background. The PCA was perfectly suited for our objectives. Therefore, we only employed data collected with the PCA.

The HEXTE is a scintillation detector made up of NaI(Tl)/CsI(Na) crystals and operates in the 15–250 keV energy range with an energy resolution of 15% at 60 keV. It has a FOV of 1° and provides a time resolution of 8 microseconds. HEXTE is devoted to the timing and measurement of the high-energy spectra of astrophysical objects.

The ASM has three cameras with position sensitive Xenon proportional counters and works in the 2–10 keV energy range. It scans 80% of the sky every 90 minutes and every camera on it has a FOV of $6^\circ \times 90^\circ$. It is devoted to the monitoring and study of time variable events.

The *Fermi* satellite was launched in June 2008 and still continues its operations. It is devoted to the discovery and understanding of the gamma-ray sources in the universe. *Fermi* operates in the energy range 8 keV–300 GeV, and is placed in a circular orbit with an inclination angle of 25.5° in an altitude of 565 km from Earth. It has two instruments on board: The Large Area Telescope (LAT) (Atwood et al., 2007, 2009) and The Gamma-ray Burst Monitor (GBM) (Meegan et al., 2009). The GBM works in the energy range 8 keV–40 MeV and is designed to

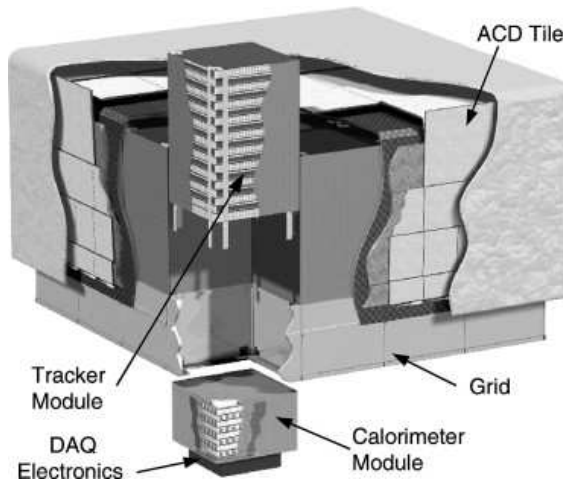


Figure 1.10: Schematic view of LAT. Tracker, calorimeter, anticoincidence and data acquisition systems are shown. The outermost layer is the thermal blanket. The Grid is composed of aluminum and supports the instrument. Figure is taken from Atwood et al. (2007).

observe transient sources. LAT scans entire sky in every ~ 3 hours, the GBM views entire sky continuously unless it is occulted by the Earth. The LAT is an imaging

instrument operating in the energy range 20 MeV–300 GeV with an effective area of 9500 cm².

In the high-energy gamma-ray regime the main interaction between radiation and matter is pair production. If the energy of a photon is greater than ~ 1 MeV, it is converted to an electron-positron pair. LAT, using this principle, converts gamma-rays to pairs; it tracks them, locates the source of gamma-ray on the sky, measures the energy and arrival time of the gamma-ray. It has 16 converter-trackers and calorimeters arranged in an array of 4×4 , an anticoincidence detector and data acquisition system (see Figure 1.10).

The converter-tracker module contains high-Z material converter foils and position-sensitive detectors in both dimensions. The converter-tracker system uses tungsten as the high-Z material and Silicon Strip Detectors (SSDs) for position-sensitive detection. These converter foils and detectors are arranged in a tray structure (see Figure 1.11). Each module contains 19 trays. The bottom tray and two trays in

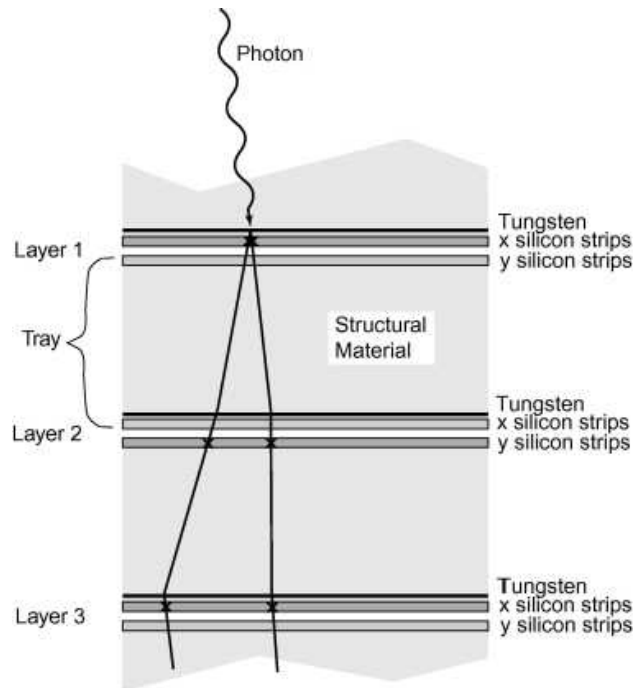


Figure 1.11: Structure of the converter-tracker system. Conversion of an incident photon to a pair and propagation of the pair between the layers are shown. Figure is taken from Atwood et al. (2007).

the middle of the module don't have any converter foil. The top tray and eleven trays have thin converter foils while the remaining four trays have thick converter foils. The aim of this design is to provide a balance between good angular resolution achieved via thin converter foils and good effective area achieved via thick converter foils. When a high-energy gamma-ray photon enters to the converter-tracker module

it is converted to an electron-positron pair in one of the tungsten foils and they are tracked by SSDs.

Electron-positron pairs after passing through converter-tracker module reach the calorimeter where their energies are measured. Each calorimeter system that is located under the converter-tracker modules is made up of 96 CsI(Tl) scintillation crystal blocks of dimension $2.7 \text{ cm} \times 2.0 \text{ cm} \times 32.6 \text{ cm}$. While particles pass through the crystal they generate scintillation light. This generated light is measured at both ends of the crystal blocks by PIN photodiodes.

The LAT is covered by an anticoincidence detector (see Figure 1.10) in order to detect and reject events caused by charged particles. It is composed of 89 scintillator detector tiles. Signals from each scintillator tile are transmitted to two photomultiplier tubes where they are read out.

Finally, the Data Acquisition System processes the information retrieved from other subsystems. It discriminates the events rejected by other subsystems, filters the data and transmits the data to the ground for further processing.

Chapter 2

Search for High-Energy Gamma-ray Emission from an Anomalous X-ray Pulsar, 4U 0142+61

This chapter was originally published in *The Astrophysical Journal*, 2010, Volume 723, Pages 100-103, Şaşmaz Muş, S. & Gögüş, E.

This version contains some additions.

2.1 Abstract

Until 2004, anomalous X-ray pulsars (AXPs) were known as strong emitters of soft X-rays only (< 10 keV). The discovery of hard X-ray component from AXPs provided important insight about their emission properties while it posed a serious challenge to explain its origin. The physical mechanism of the hard emission component has still not been fully resolved. We investigate the high-energy gamma-ray properties of the brightest AXP, 4U 0142+61 using data collected with the Large Area Telescope on board *Fermi Gamma-ray Space Telescope* to establish the spectral behavior of the source on a very broad energy span and search for pulsed emission. Here, we present our results of detailed search for the persistent and pulsed high-energy gamma-ray emission from 4U 0142+61 which result in no significant detection. However, we obtain upper limits to the persistent high-energy gamma-ray emission flux which helps us to constrain existing physical models.

2.2 Introduction

Anomalous X-ray pulsars (AXPs) have been intriguing sources since their discovery in early 1980s (Fahlman & Gregory, 1981). They are bright X-ray sources with X-ray luminosities (below 10 keV) in the range of 10^{33} – 10^{36} erg s^{-1} . They spin rather slowly and their spin periods are clustered in a narrow range of 2–12 s. The lack of any evidence for binary nature (e.g., Doppler modulation in their long term pulse periods) eliminates the possibility that they are accreting matter from a donor. Their spin down rates are relatively large, ranging between 10^{-12} and 10^{-10} s s^{-1} . Their rotational energy loss is insufficient by orders of magnitude to provide the observed X-ray luminosities. AXPs are commonly regarded as young isolated neutron stars that are powered by their extremely strong magnetic fields, $B \gtrsim 10^{14}$ G (Duncan & Thompson, 1992). Such strong magnetic fields can efficiently slow these young systems down via magnetic braking and provide energy for the emitted X-rays via diffusion of evolving magnetic field (Thompson & Duncan, 1996). A detailed review on AXPs can be found in Mereghetti (2008) and Woods & Thompson (2006).

A major observational development in AXP studies was the discovery of hard X-ray emission from AXPs 1E 1841-045 (Kuiper et al., 2004), 4U 0142+61 (den Hartog et al., 2004) and 1RXS J170849.0-400910 (Revnivtsev et al., 2004). 1E 1841-045, located at the center of supernova remnant (SNR) Kes 73, is the first AXP from which non-thermal pulsed hard X-ray/soft gamma-ray emission was discovered (Kuiper et al., 2004). The pulsed nature of this emission eliminates the possibility of its SNR origin. Spectral studies of this source using *INTEGRAL* observations in the 20–300 keV band revealed a power-law shape with an index of 1.39 ± 0.05

but no evidence of spectral break (Kuiper et al., 2008). The hard X-ray emission from 1RXS J170849.0-400910 was discovered in the Galactic Plane Survey observations with *INTEGRAL* (Revnivtsev et al., 2004) and shown to be pulsed as well (Kuiper et al., 2006; den Hartog et al., 2008). Finally, hard emission component from 4U 0142+61 was discovered during *INTEGRAL* observations of the Cassiopeia region (den Hartog et al., 2004). Detailed studies with 2.37 Ms *INTEGRAL* observations showed a power law spectrum up to about 230 keV with an index of 0.93 ± 0.06 (den Hartog et al., 2008). Based on the logparabolic function fit to the *INTEGRAL* SPI and ISGRI observations, they estimate a peak energy of the spectral energy distribution to be ~ 228 keV (den Hartog et al., 2008), and 20–150 keV flux as $(8.97 \pm 0.86) \times 10^{-11}$ erg cm $^{-2}$ s $^{-1}$. It is important to note that the energy emitted above 15 keV is comparable or larger than that in the soft X-ray band (that is, below 10 keV, see, e.g., den Hartog et al., 2008).

The physical nature of the hard X-ray/soft gamma-ray emission is still not well understood. Thompson & Beloborodov (2005); Beloborodov & Thompson (2007) proposed that the hard X-ray emission could originate from a plasma corona around the magnetar. They suggest that such a corona around magnetars can be formed via starquakes that could shear the neutron star crust and its external magnetic field. Heyl & Hernquist (2005a,b) proposed the fast-mode break down model in which an optically thick fireball produced by the magnetohydrodynamics waves created near the surface of the neutron star. Further they suggest that if fast modes are not strong enough to yield an optically thick fireball, the produced non-thermal emission would be sufficient to explain the observed high-energy emission from soft gamma repeaters and AXPs. Another attempt to explain the hard X-ray emission is by Baring & Harding (2007). They suggest that the upscattered surface thermal X-ray photons is the source of observed non-thermal hard X-ray emission from magnetars.

Cheng & Zhang (2001) suggested a gamma-ray emission model based on the outer gap model (see §1.1.3). This model predicts gamma-ray emission from magnetars that can be detected by *Fermi*. However, there is no explanation of the hard X-ray emission in this theory. Finally, Trümper et al. (2010) suggested an explanation in the context of fallback disk model in which they propose that the hard X-ray emission originates from the bulk-motion Comptonization (BMC) of soft X-ray photons from the polar cap. However, until now there are only one magnetar, 4U 0142+61, with an observation of a disk around it (Wang et al., 2006) and another one, 1E 2259+586, with a less robust observation of a disk (Kaplan et al., 2009) while there are several magnetars observed in the hard X-ray band (see, e.g., Kuiper et al., 2004; Götz et al., 2006; den Hartog et al., 2008).

In order to understand the nature of the hard emission component of AXPs, it is crucial to establish their spectral shapes on a wide range in the energy domain.

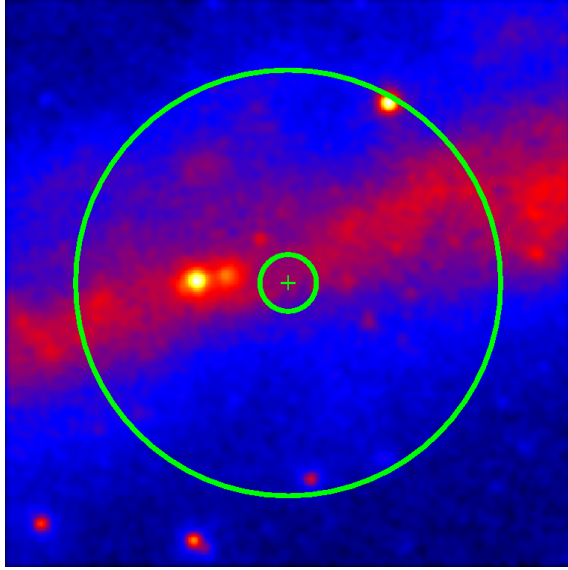


Figure 2.1: Smoothed *Fermi*/LAT count map around AXP 4U 0142+61 in the 0.2–100 GeV energy range. The large circle and small circle show the 15° and 2° radius extraction regions, respectively. The plus sign indicates the position of AXP 4U 0142+61.

In particular, it is important to determine where their spectral energy distribution peak. Thanks to the Large Area Telescope (LAT) on board *Fermi*, we are now able to investigate high-energy behavior of these sources with an unprecedented data quality.

In this paper, we performed detailed search for persistent and pulsed high-energy gamma-ray emission from 4U 0142+61 using *Fermi*/LAT observations. We also employed contemporaneous *RXTE* observations to obtain the spin ephemeris of the source. In §2.3, we describe the observations used and details of data analysis. We present our results in §2.4 and discuss their implications in §2.5.

2.3 Observations and Data Analysis

2.3.1 *Fermi*/LAT

LAT is one of the two instruments on board *Fermi* operating in the energy band of 20 MeV–300 GeV. It is a pair conversion telescope with a high-resolution silicon tracker, calorimeter, anticoincidence detector, programmable trigger and data acquisition system (Atwood et al., 2009). Since 2008 August 4, the LAT has been operating as an all sky monitor in high-energy gamma-rays, covering the full sky in approximately every 3 hr (see §1.4).

We accumulated the LAT data within a 15° radius¹ centered at 4U 0142+61, collected from 2008 August 4 to 2010 April 29 with an exposure time of ~ 31.7 Ms. We also performed spectral analysis using a 2° radius region around the source in order to completely avoid contamination from the nearby bright sources. We performed our unbinned likelihood analysis² using ScienceTools v9r15p2 with P6_V3_DIFFUSE set as the instrumental response. In the event selection process, we set the maximum zenith angle to 105° in order to eliminate background gamma-rays due to the Earth limb. All time intervals where the zenith cut intersects the region were excluded. In Figure 2.1, we present the count map image of the 40° radius region centered at 4U 0142+61. The diffuse gamma-ray emission from the Milky Way was modeled with the latest model, `gll_iem_v02.fit`. We also used `isotropic_iem_v02.txt` to account for the extragalactic isotropic diffuse emission and residual instrumental background. The spectral fits and flux calculations were done with the python version of `gtlike`, `pyLikelihood`.

For timing analysis, photon arrival times of all events within the 2° extraction region around 4U 0142+61 were converted to that at the solar system barycenter using `gtbary` of ScienceTools.

2.3.2 *RXTE*

To search for pulsed high-energy gamma-ray emission from 4U 0142+61, we obtained the precise spin ephemeris of the source using contemporaneous *RXTE* observations. On board *RXTE*, there are three scientific payloads: the Proportional Counter Array (PCA) that is sensitive to photon energies between 2–60 keV, the High-Energy X-ray Timing Experiment, sensitive to photons in the 15–250 keV photons and the All Sky Monitor. We have employed only the PCA observations to achieve our goal.

4U 0142+61 has been monitored with the *RXTE* periodically for the last ~ 8 years with pointings almost uniformly spaced, usually by about two weeks. We have selected 53 *RXTE* observations that were performed between 2008 August 4 and 2010 April 30 (under the Program IDs: P93019, P94019 and P05019) which cover the investigated LAT observing span. Individual *RXTE* pointings are typically between 3 and 4 ks long and the total exposure time of all selected observations is about 196 ks. For each observation, we extracted events in the 2–10 keV range collected with the PCA and converted their arrival times to the solar system barycenter using the `faxbary` tool of HEASoft 6.8.

¹As suggested by the *Fermi*/LAT instrument team,
http://fermi.gsfc.nasa.gov/ssc/data/analysis/documentation/Cicerone/Cicerone_Likelihood/Choose_Data.html

²http://fermi.gsfc.nasa.gov/ssc/analysis/scitools/likelihood_tutorial.html

2.4 Results

2.4.1 Search for Persistent Emission

As evident from Figure 2.1, 4U 0142+61 is clearly not detected in the LAT energy passband. A point source search using the filtered event list with the `gtfindsrc` tool of ScienceTools results in a potential source whose coordinates are inconsistent with that of 4U 0142+61, therefore yields no detection.

In order to obtain very-high-energy gamma-ray flux upper limits of 4U 0142+61, we fitted the data from the 15° radius region. We added all bright cataloged sources and recently discovered blazar (Vandenbroucke et al., 2010) within this region of interest into the model as well as the galactic diffuse and extragalactic diffuse emission leaving their model parameters free. The fit yields a test statistics (TS) value of ~ 0.23 which implies a detection significance less than 1σ . The 3σ flux upper limits with a power law index 2.5 are 2.32×10^{-6} MeV cm $^{-2}$ s $^{-1}$ in the 0.2–1.0 GeV band and 1.28×10^{-6} MeV cm $^{-2}$ s $^{-1}$ in the 1.0–10.0 GeV band. Note here that the spectral parameters and fluxes of the cataloged sources obtained in the latter fit are consistent with the catalog values³, showing that our analysis is robust.

We performed similar spectral modelling for the data of the 2° radius region with a power law model of index 3 as well as the galactic diffuse and extragalactic isotropic diffuse emission models. The resulting TS value is ~ 3 which implies a detection significance less than 2σ . We chose the 0.2–1.0 and 1.0–10.0 GeV energy bands for flux calculations and find 3σ upper limits to the source flux in these energy bands as 5.72×10^{-6} MeV cm $^{-2}$ s $^{-1}$ and 1.29×10^{-6} MeV cm $^{-2}$ s $^{-1}$, respectively. In Figure 2.4, we present the high-energy gamma-ray flux upper limits of 4U 0142+61 in the νF_ν representation along with its low energy gamma-ray behavior (the data obtained from den Hartog et al., 2008). We discuss their implications in §2.5.

2.4.2 Search for Pulsed Emission

We employed a Fourier based epoch folding technique to obtain the spin ephemeris of 4U 0142+61 using *RXTE*/PCA observations covering the time span of the LAT exposure of the source. We first generated the pulse profile of the source using three consecutive PCA observations around the epoch (MJD 54713.5). Then, we grouped observations in order for them to be spaced at least 0.2 days apart from each other, and we cross correlated the pulse profile of each group of pointings with the template profile to determine the phase shift of each pointing with respect to the template. Finally, we fit the phase shifts with a polynomial to obtain the spin ephemeris. In

³http://fermi.gsfc.nasa.gov/ssc/data/access/lat/1yr_catalog

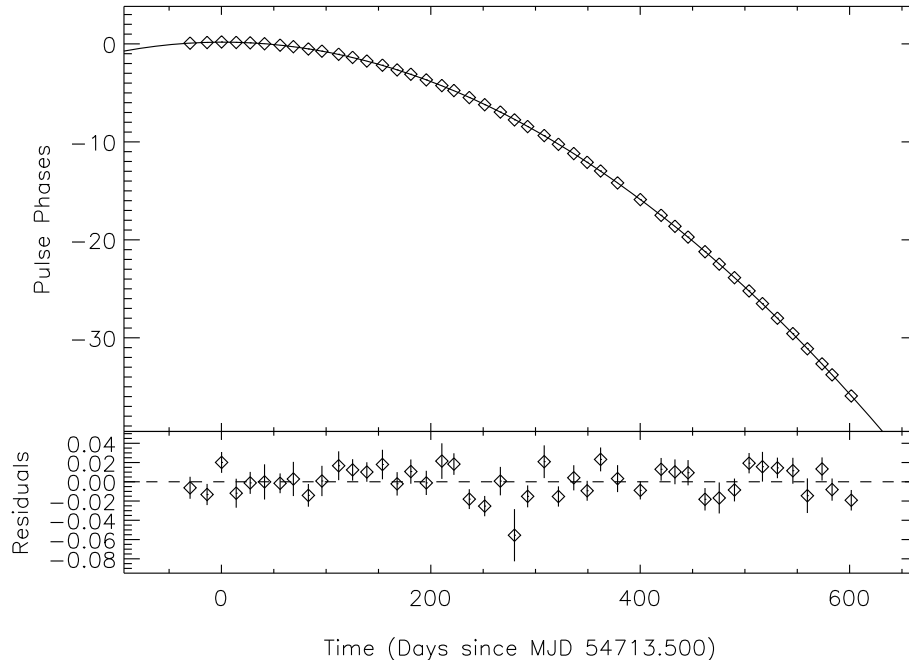


Figure 2.2: (*Top*) spin phase shifts of *RXTE*/PCA observations of 4U 0142+61 with respect to the epoch. The solid line is the best fitting model, that is a third-order polynomial. (*Bottom*) residuals of the fit.

Figure 2.2, we present the phase shift and the best fitting model, that is a third-order polynomial ($\chi^2/\text{degrees of freedom} = 59.6/42$). We tabulate the best fit spin ephemeris parameters of 4U 0142+61 in Table 2.1.

Table 2.1: Spin ephemeris of 4U 0142+61

Parameter	Value
Range (MJD)	54682.6 – 55315.1
Epoch (MJD)	54713.5
ν (Hz)	0.1150900026(9)
$\dot{\nu}$ (10^{-14} Hz s $^{-1}$)	-2.745(8)
$\ddot{\nu}$ (10^{-23} Hz s $^{-2}$)	3.6(3)

To search for pulsed high-energy gamma-ray emission from 4U 0142+61, we generated the LAT pulse profiles of the source in the 0.2–1.0 GeV and 1.0–10.0 GeV energy ranges using the precise PCA spin ephemeris obtained. We find that both LAT profiles are consistent with random fluctuations with respect to its mean. We calculate a 3σ upper limit to the rms pulsed fraction of 1.5% in the 0.2–1.0 GeV band and 2.3% in the 1.0–10.0 GeV band. We also investigated the lower energy part of the LAT passband (30–200 MeV), which also resulted with no evidence of pulsed emission; the 3σ rms pulsed fraction upper limit is 1.6% (see Figure 2.3).

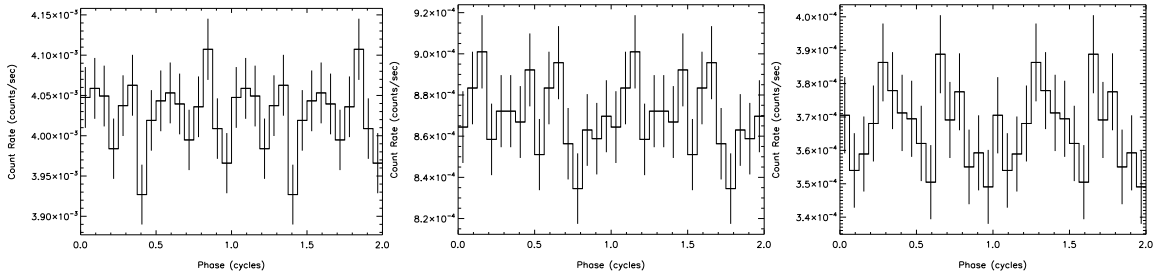


Figure 2.3: *Fermi*/LAT pulse profiles of 4U 0142+61. *Left*: in the 30–200 MeV band, *Middle*: in the 200 MeV–1 GeV band, *Right*: in the 1–10 GeV band.

2.5 Discussion

We searched for both persistent and pulsed high-energy emission from the AXP 4U 0142+61 using *Fermi*/LAT data. We find no significant detection in either of the two objectives. Nevertheless, we obtained 3σ upper limits for the high-energy persistent emission in the 0.2–1.0 GeV and 1.0–10.0 GeV ranges of 5.72×10^{-6} MeV cm $^{-2}$ s $^{-1}$ and 1.29×10^{-6} MeV cm $^{-2}$ s $^{-1}$, respectively. As for the pulsed emission, a 3σ upper limit to the rms pulsed amplitude in the 0.2–1.0 GeV range is 1.5% and in the 1.0–10.0 GeV range is 2.3%. The search in the lower energy LAT passband (30–200 MeV) also did not yield a pulsed emission. The 3σ rms pulsed amplitude upper limit is 1.6%. Our LAT upper limits are much lower than high pulsed fraction (up to 100%) seen in hard X-rays with *INTEGRAL* (den Hartog et al., 2008).

In order to establish the spectral shape of 4U 0142+61 on a wide energy range, we constructed the νF_ν spectrum of the source in the 15 keV–10 GeV range by adopting the hard X-ray spectrum presented in den Hartog et al. (2008) and placing the upper limits calculated in this work. den Hartog et al. (2008) fitted the *INTEGRAL*/ISGRI data with a simple power law model of index 0.93 ± 0.06 . We present this fit with dashed lines in Figure 2.4. We place an upper limit curve, which is the line connecting the two LAT upper limit measurements (as shown with solid line in Figure 2.4), is also a power law with an index of -0.76 . These two curves intersect with each other at ~ 1.1 MeV which is an upper limit to the spectral break energy. Note that the spectral break upper limit is consistent with den Hartog et al. (2008) measurement of 279_{-41}^{+65} keV obtained by fitting a logparabolic function to the combined *XMM-Newton*, *INTEGRAL*/ISGRI, *INTEGRAL*/SPI and *CGRO*/COMPTEL data.

Our estimated upper limit to the spectral break energy is in accordance with the coronal emission model by Beloborodov & Thompson (2007). According to their model, photons with energies in excess of $\gtrsim 1$ MeV would be trapped in the

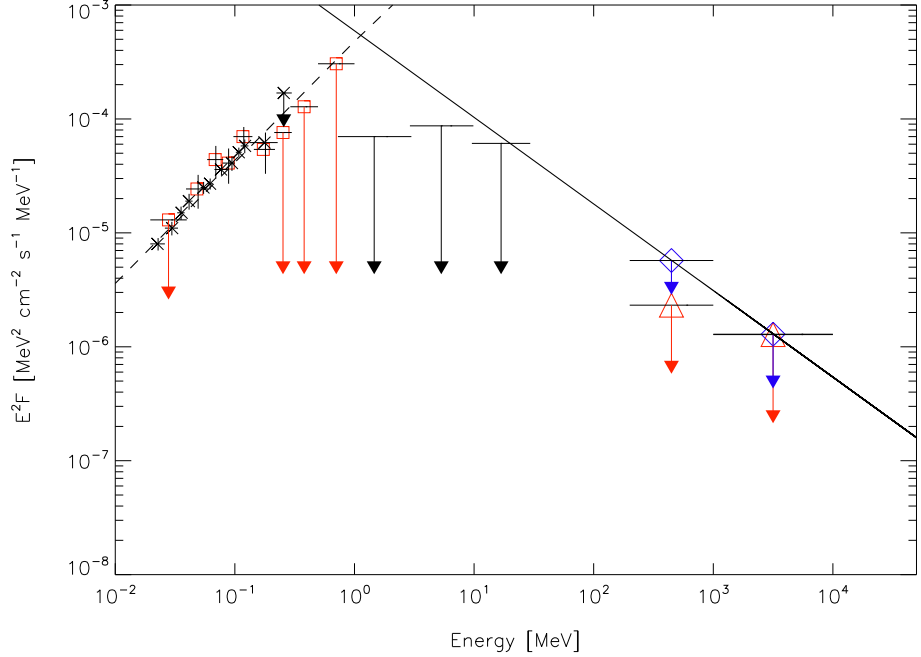


Figure 2.4: Wide band νF_ν spectrum of 4U 0142+61: *INTEGRAL*/ISGRI (20–300 keV) in black (stars), *INTEGRAL*/SPI (20–1000 keV) in red (open squares) and *CGRO*/COMPTEL (0.75–30 MeV) 2σ upper limits in black (data constructed from den Hartog et al., 2008). *Fermi*/LAT upper limits (in the 0.2–1.0 GeV and 1.0–10.0 GeV) obtained using the 2° extraction region are shown in blue diamonds and that of 15° extraction region in red triangles. Dashed line is the best fit power law model to the ISGRI data points (den Hartog et al., 2008). Solid line shows the power law upper limit trend of the 2° *Fermi*/LAT region.

ultrastrong magnetic fields ($B \gtrsim 10^{14}$ G). In such a case photons would either split into two photons or they would create an electron-positron pair, therefore, suppressing the emission from the inner corona above ~ 1 MeV. This is consistent with den Hartog et al. (2008)’s spectral break energy measurement of 279^{+65}_{-41} keV and our upper limit of ~ 1.1 MeV. However, a disturbance in the magnetosphere that is leading to formation of a corona is a transient event with a timescale of 1 yr (Beloborodov & Thompson, 2007; Beloborodov, 2013) while the hard X-ray emission of 4U 0142+61 didn’t show any significant variation during the 2003–2011 *INTEGRAL* observations (Wang et al., 2013).

Our estimate of the spectral break energy upper limit also agrees with the predictions of the quantum electrodynamics model by Heyl & Hernquist (2005a,b) as they expect the lower limit to the break energy to be around 1 MeV. On the other hand, they claim that if a source has a significant excess emission in optical wavelengths, as in the case of 4U 0142+61 (Hulleman et al., 2000), its νF_ν spectrum should continuously increase in the 10–200 MeV range. Note that optical emission originates from the neutron star itself (Kern & Martin, 2002; Dhillon et al., 2005)

and from a disk around 4U 0142+61 (Wang et al., 2006; Ertan & Çalıřkan, 2006). However, the origin of the excess optical emission in 4U 0142+61 is not clear. In the case that the excess optical emission originates from the compact object, our results place constraint, although not stringent, on the quantum electrodynamics model due to the lack of increase in the 10–200 MeV range in the νF_ν spectrum. If the disk provides a significant contribution to the observed emission (see, e.g., Ertan et al., 2007), then the optical radiation from the neutron star itself would not be excessive and the quantum electrodynamics model would still remain feasible.

On the other hand, Tong et al. (2010, 2011) discussed *Fermi* results in detail in the context of outer gap model for magnetars (Cheng & Zhang, 2001) in which gamma-ray emission is expected, and suggested that the non-detection is consistent with the fallback disk model due to inefficiency of the outer gap in case of accretion onto the star.

Chapter 3

Long-Term Timing and Glitch Characteristics of Anomalous X-ray Pulsar

1RXS J170849.0-400910

This chapter was published in *The Astrophysical Journal*, 2013, Volume 778, Page 156, Şaşmaz Muş, S., & Göğüş, E.

3.1 Abstract

We present the results of our detailed timing studies of an anomalous X-ray pulsar, 1RXS J170849.0-400910, using *Rossi X-ray Timing Explorer (RXTE)* observations spanning over ~ 6 yr from 2005 until the end of *RXTE* mission. We constructed the long-term spin characteristics of the source and investigated time and energy dependence of pulse profile and pulsed count rates. We find that pulse profile and pulsed count rates in the 2–10 keV band do not show any significant variations in ~ 6 yr. 1RXS J170849.0-400910 has been the most frequently glitching anomalous X-ray pulsar: three spin-up glitches and three candidate glitches were observed prior to 2005. Our extensive search for glitches later in the timeline resulted in no unambiguous glitches though we identified two glitch candidates (with $\Delta\nu/\nu \sim 10^{-6}$) in two data gaps: a strong candidate around MJD 55532 and another one around MJD 54819, which is slightly less robust. We discuss our results in the context of pulsar glitch models and expectancy of glitches within the vortex unpinning model.

3.2 Introduction

Glitches, sudden jumps in the rotation frequency of neutron stars, are the unique events that provide invaluable information on the internal structure of extremely compact stars. Originally detected from rotation powered neutron stars (see, e.g., Richards & Comella, 1969; Radhakrishnan & Manchester, 1969), glitches are generically not associated to changes in the radiative behavior of the source (but see Weltevrede et al., 2011). Therefore, the proposed glitch models involve dynamical variations in the neutron star interior instead of an external torque mechanism. The size of the glitch typically reflects the underlying internal dynamics of the neutron star: small-size glitches ($\Delta\nu/\nu \sim 10^{-9}$, aka. Crab-like glitches) are explained by the decrease of the moment of inertia of the pulsar (Ruderman, 1969; Baym & Pines, 1971) and large-size glitches ($\Delta\nu/\nu \sim 10^{-6}$, aka. Vela-like glitches) are described as the angular momentum transfer from inner crust neutron superfluid to the crust by the sudden unpinning of the vortices that are pinned to the inner crust nuclei (Anderson & Itoh, 1975; Pines et al., 1980).

Anomalous X-ray Pulsars (AXPs) are slowly rotating ($P \sim 2\text{--}12$ s) neutron stars with persistent emission being significantly in excess of their inferred rotational energy loss rate. So far, there has been no evidence of binary signature in AXPs. They are young systems ($\sim 10^4$ yr) as inferred from their characteristic spin-down ages ($P/2\dot{P}$), and also supported by their location on the plane of Milky Way, and the association of at least five AXPs with their supernova remnants. Almost all AXPs emitted short duration, energetic bursts in X-rays (see, e.g., Gavriil et al.,

2002; Kaspi et al., 2003, and for a recent review Rea & Esposito, 2011). Their surface dipole magnetic field strengths inferred from their periods and spin-down rates are on the order of $10^{14} - 10^{15}$ G, which is much higher than that of conventional magnetic field strengths of pulsars. The decay of their extremely strong magnetic fields is proposed as the source of energy for their persistent X-ray emission and burst activity (Thompson & Duncan, 1995, 1996; Thompson et al., 2002). Recently, observational evidence of dipole field decay was reported by Dall’Osso et al. (2012).

Glitch activity from an AXP was first seen in 1RXS J170849.0-400910 (Kaspi et al., 2000). Thanks to almost continuous spin monitoring of AXPs with *RXTE* for more than a decade, sudden spin frequency jumps have now been observed from six AXPs (see, e.g., Kaspi et al., 2003; Dall’Osso et al., 2003; Woods et al., 2004; Morii et al., 2005; Israel et al., 2007b,a; Dib et al., 2008, 2009; Gavriil et al., 2011). Fractional glitch amplitudes ($\Delta\nu/\nu$) of these events range from 10^{-8} to 10^{-5} (Dib et al., 2009; İğdem et al., 2012) and fractional post-glitch change in spin-down rates ($\Delta\dot{\nu}/\dot{\nu}$) are between -0.1 and 1 (Kaspi et al., 2003; Dib et al., 2009).

Glitches from AXPs somehow resemble those from radio pulsars, but contain some peculiar distinctive features in their recovery behavior and associated radiative characteristics (Woods et al., 2004; Morii et al., 2005; Dib et al., 2008, 2009; Gavriil et al., 2011). AXP 1E 2259+586 went into an outburst in conjunction with a glitch (Kaspi et al., 2003; Woods et al., 2004). AXP 1E 1048.1-5937 has shown X-ray burst correlated with a glitch event (Dib et al., 2009). During the burst active phase of AXP 4U 0142+61 between 2006 and 2007, six short bursts and a glitch with a long recovery time were observed (Gavriil et al., 2011). AXP 1E 1841-045 has exhibited bursts and glitches, but not coincidentally (Dib et al., 2008; Zhu & Kaspi, 2010; Kumar & Safi-Harb, 2010; Lin et al., 2011). Israel et al. (2007a) reported a burst and an extremely large glitch ($\Delta\nu/\nu \sim 6 \times 10^{-5}$) from CXOU J164710.2-455216, but the possibility of such a glitch was ruled out by Woods et al. (2011). However, the latter team point out that a glitch with the size of usual AXP glitches may indeed have occurred. 1RXS J170849.0-400910 has been the most frequently glitching AXP (Kaspi et al., 2000; Kaspi & Gavriil, 2003; Dall’Osso et al., 2003; Israel et al., 2007b; Dib et al., 2008), but it has not shown any bursts or remarkable flux variability related to the glitch epochs.

It is still unclear whether glitches are always associated with radiative enhancements. Recently, Pons & Rea (2012) suggested that in the context of the starquake model, glitches observed in the bright sources can be related to the radiative enhancements but due to the bright quiescent state of these sources and fast decay of the enhancements, these events can be observed as small changes in the luminosity or only detected in faint sources.

1RXS J170849.0-400910 is an AXP with a spin period of ~ 11 s. After the

discovery of its spin period (Sugizaki et al., 1997), it has been monitored with *RXTE* for ~ 13.8 yr. Analyzing the first ~ 1.4 yr of data Israel et al. (1999) and Kaspi et al. (1999) have concluded that the source is a stable rotator. The continued monitoring has been essential in detecting three unambiguous glitches and three glitch candidates without any significant pulse profile variations (Kaspi et al., 2000; Kaspi & Gavriil, 2003; Dall’Osso et al., 2003; Israel et al., 2007b; Dib et al., 2008). There appears to be a correlation between intensity and spectral hardness: the X-ray spectrum gets softer(harder) while the X-ray flux decreases(increases), possibly in relation with glitches (Rea et al., 2005; Campana et al., 2007; Rea et al., 2007; Israel et al., 2007b). Götz et al. (2007) reported the same correlation in the hard X-rays using *INTEGRAL*/ISGRI data. However, den Hartog et al. (2008) claimed that they did not find the reported variability in their analysis. Thompson et al. (2002) proposed that external magnetic field can twist and untwist. Twisting and untwisting of the external magnetic field can lead to cracks and unpin the vortices for the glitches (Thompson & Duncan, 1996; Dall’Osso et al., 2003). Such twist/untwist of the magnetic field with a period of $\sim 5-10$ yr has been suggested as an explanation for the observed correlations (Rea et al., 2005; Campana et al., 2007).

Here, we report the long-term analysis of *RXTE* observations of 1RXS J170849.0-400910 spanning ~ 6 yr. In §3.3 we describe *RXTE* observations that we used in our analysis. We present long-term timing characteristics of the source in §3.4.1. In §3.4.2 & §3.4.3 we constructed the pulse profiles, calculated pulsed count rates and examined their variability both in time and energy. We present the results of our extensive search for glitches in §3.4.4. Finally, in §3.5 we discuss our results in the context of glitch models and expectancy of glitches in the vortex unpinning model.

3.3 *RXTE* Observations

1RXS J170849.0-400910 has been almost regularly monitored with *RXTE* in 528 pointings since the beginning of 1998. Phase connected timing behavior of the source was investigated by Dib et al. (2008) using the *RXTE* data collected between 1998 January 12 and 2006 October 7, Dall’Osso et al. (2003) using data from 1998 January 13 to 2002 May 29, and Israel et al. (2007b) using from 2003 January 5 to 2006 June 3. Here we analyzed *RXTE* data collected in 280 pointings between 2005 September 25 and 2011 November 17 with the Proportional Counter Array (PCA). Note that the first 49 pointings in our sample were also used by Dib et al. (2008). We included them in order to maintain the continuity in the timing characteristics of 1RXS J170849.0-400910. Exposure times of individual *RXTE* observations ranged between 0.25 ks (in one observation) and 2.5 ks, with a mean exposure time of 1.9 ks (see Figure 3.1 for a distribution of exposure times). For our timing analysis,

we used data collected with all operating Proportional Counter Units (PCUs) in GoodXenon mode that provides a fine time resolution of $1 \mu\text{s}$.

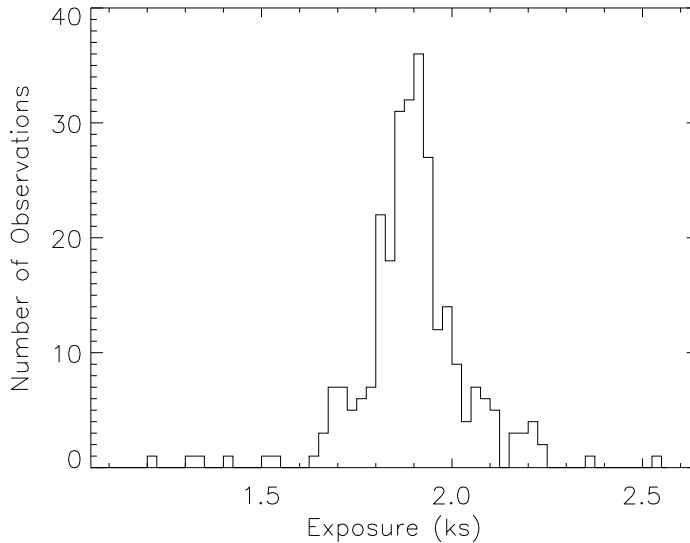


Figure 3.1: Distribution of exposure times of individual *RXTE*/PCA observations. The shortest observation with an exposure of 0.25 ks is excluded for clarity.

3.4 Data Analysis And Results

3.4.1 Phase Coherent Timing

We selected events in the 2–6 keV energy range from the top Xenon layer of each PCU in order to maximize the signal-to-noise ratio, as done also by Dib et al. (2008). All event arrival times were converted to the solar system barycenter and binned into light curves of 31.25 ms time resolution. We inspected each light curve for bursts and discarded the time intervals with the instrumental rate jumps. We merged observations together if the time gap between them was less than 0.1 days. The first set of observations (i.e. segment 0 in Table 3.1) which includes 49 observations from Dib et al. (2008) were folded initially with the spin ephemeris given by Dib et al. (2008) and later by maintaining the phase coherence. We then cross-correlated the folded pulse profiles with a high signal-to-noise template pulse profile generated from a subset of observations and determined the phase shifts of observations with respect to the template. We fitted phase shifts with

$$\phi(t) = \phi_0(t_0) + \nu_0(t - t_0) + \frac{1}{2}\dot{\nu}_0(t - t_0)^2 + \dots, \quad (3.1)$$

whose coefficients yield the spin frequency, and its higher order time derivatives, if required. In Table 3.1 we list the best fit spin frequency and frequency derivatives to the specified time intervals, obtained using also listed number of time of arrivals (TOAs). In Figure 3.2 (a) we present the spin frequency evolution of 1RXS J170849.0-400910, and in (b) phase residuals after subtraction of the best fit phase model given in Table 3.1. We obtained frequency derivatives by fitting a second order polynomial to the sub-intervals of about 2.5 months long data and present them in Figure 3.2 (c).

Table 3.1: Pulse Ephemeris of 1RXS J170849.0-400910 ^a

Parameter	Segment 0	Segment 1	Segment 2	Segment 3	Segment 4	Segment 5
Range (MJD)	53638 – 54056	54106 – 54421	54471 – 54786	54837 – 55151	55203 – 55517	55568 – 55882
Epoch (MJD)	53635.6772	54106.040	54471.050	54836.804	55202.849	55567.977
Number of TOAs	55	46	46	43	45	44
ν (Hz)	0.090884080(5)	0.090877558(5)	0.090872536(5)	0.090867590(3)	0.090862448(1)	0.090857386(7)
$\dot{\nu}$ (10^{-13} Hz s ⁻¹)	-1.55(2)	-1.50(1)	-1.43(2)	-1.642(5)	-1.641(1)	-1.73(2)
$\ddot{\nu}$ (10^{-22} Hz s ⁻²)	-18(4)	-14(2)	-23(3)	1.9(4)	–	19(3)
$d^3\nu/dt^3$ (10^{-28} Hz s ⁻³)	2.9(5)	0.9(2)	1.3(2)	–	–	-1.41(3)
$d^4\nu/dt^4$ (10^{-35} Hz s ⁻⁴)	-1.7(2)	–	–	–	–	–
rms (phase)	0.0174	0.0145	0.0200	0.0212	0.0265	0.0203

^a Values in parenthesis are the uncertainties in the last digits of their associated measurements.

3.4.2 Pulse Profile Evolution

We investigated long-term pulse profile evolution of the source both in energy and time. For the pulse profile analysis, we excluded data collected with PCU0 and the data of PCU1 for the observations after 2006 December 25 due to the loss of their propane layers (therefore, having elevated background levels). We obtained the pulse profiles with 32 phase bins by folding the data in six energy bands with the appropriate phase connected spin ephemeris given in Table 3.1. The energy intervals investigated are 2–10 keV, 2–4 keV, 4–6 keV, 6–8 keV, 8–12 keV and 12–30 keV. In order to account for the different number of operating PCUs, we normalized the rates of each bin with the number of active PCUs. Finally, we subtracted the DC level and divided by the maximum rate of each profile. In Figures 3.3 and 3.4, we present the normalized pulse profiles for the six segments given in Table 3.1 in six energy bands and their evolution in time.

The 2–10 keV pulse profiles of 1RXS J170849.0-400910 are characterized by a broad structure formed by the superposition of two features: the main peak near the pulse phase, $\phi \sim 0.55$ and a weaker shoulder around $\phi \sim 0.85$. Pulse profiles of the two lowest energy bands exhibit an additional shoulder (near phase ~ 0.35) in the 55203–55516 epoch (Segment 4), which is not clearly seen in any other epochs. Pulse profiles in the 2–4 keV band consist of the main peak in all epochs, while the shoulder feature ($\phi \sim 0.85$) is either weak or non-existent. The shoulder appears in

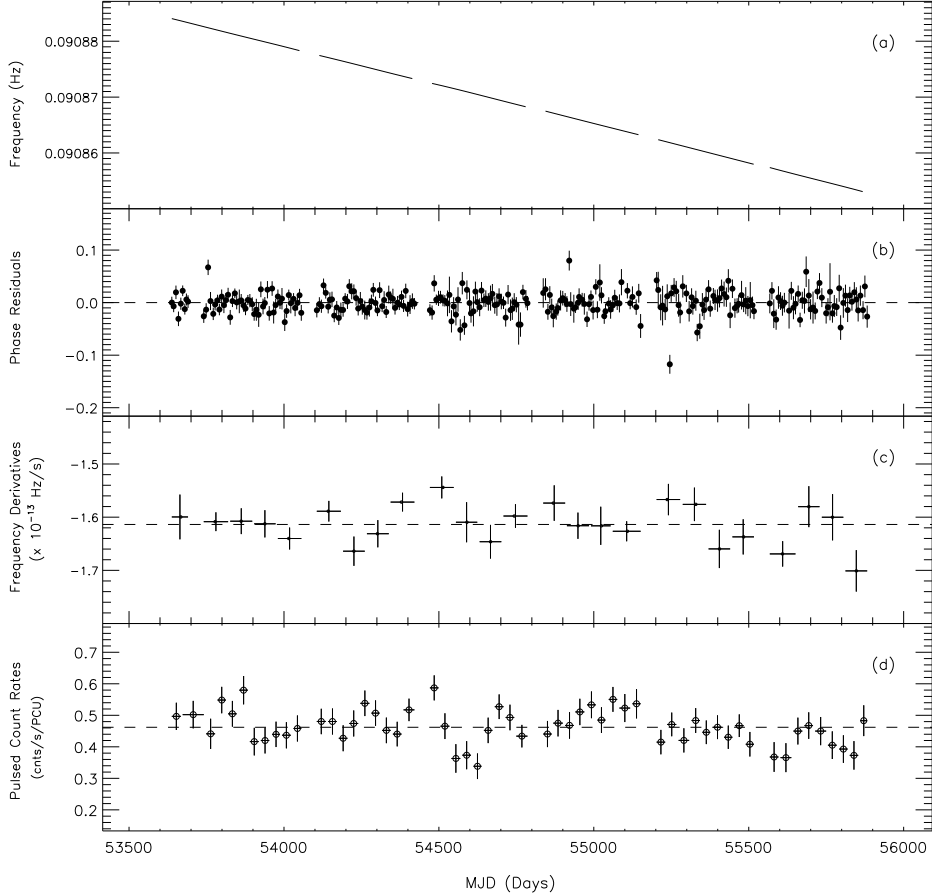


Figure 3.2: (a) Spin frequency evolution of 1RXS J170849.0-400910. (b) Phase residuals after the subtraction of the pulse ephemeris given in Table 3.1. (c) Frequency derivatives obtained using ~ 2.5 months long data segments. (d) Long-term behavior of the rms pulsed count rates in the 2–10 keV band.

the 4–6 keV band, and becomes more dominant above 6 keV. Pulse profiles above 8 keV contain only the shoulder feature. Note the fact that the duty cycle of the pulse profiles drops with increasing energy. The dominance of the secondary peak (shoulder) with the increase in photon energy was also reported in den Hartog et al. (2008) by using *INTEGRAL*, *XMM-Newton* and earlier *RXTE* observations.

We calculated the Fourier Powers (FPs) for a quantitative measure of the pulse profile variations. First we computed the Fourier transform of each profile and calculated the powers in the first six harmonics as $FP_k = 2(a_k^2 + b_k^2)/(\sigma_{a_k}^2 + \sigma_{b_k}^2)$. Here a_k and b_k are the coefficients in the Fourier series, and σ_{a_k} and σ_{b_k} are the uncertainties in the coefficients a_k and b_k , respectively. Second, we corrected the powers for the binning using equation 2.19 of van der Klis (1989) and calculated upper and lower limits to the FPs by using the method described in Groth (1975) (and also in Vaughan et al., 1994). Finally, we normalized the FPs by the total power. We show in Figure 3.5, the time evolution of the normalized harmonic

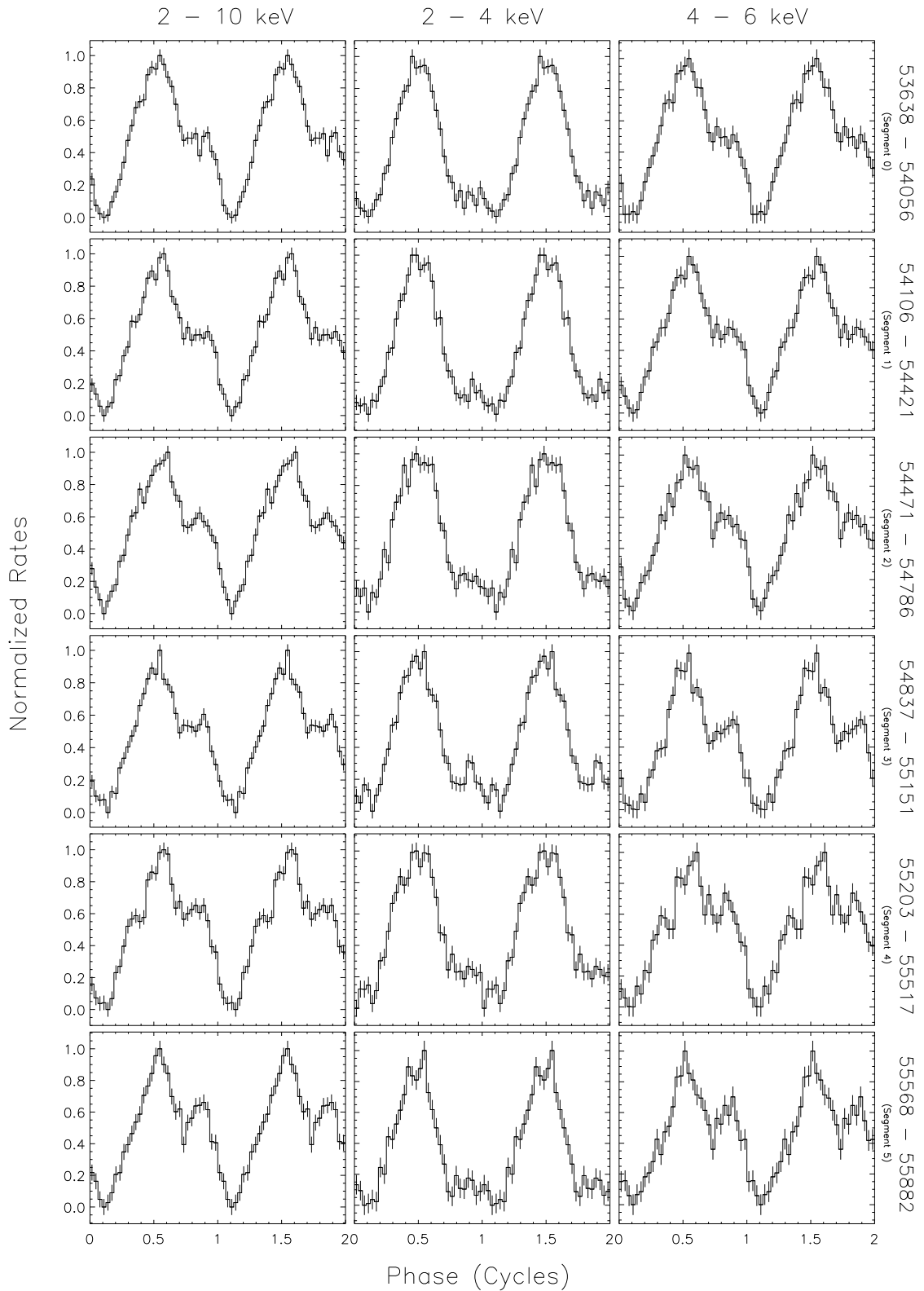


Figure 3.3: Pulse profile history of 1RXS J170849.0-400910 in the energy bands 2–10, 2–4 and 4–6 keV. The labels on the right are the corresponding time intervals of accumulated data.

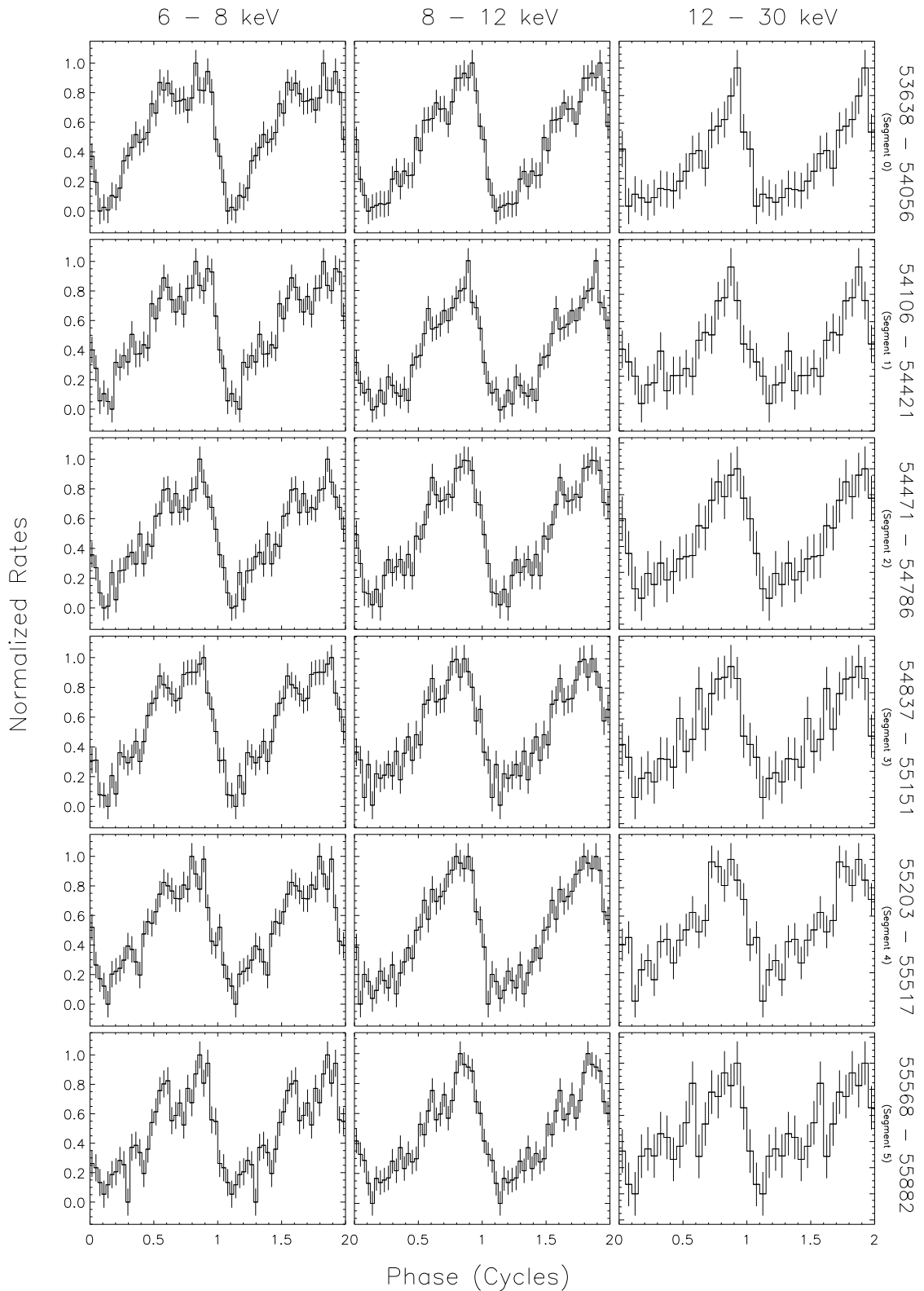


Figure 3.4: Pulse profile history of 1RXS J170849.0-400910 in the energy bands 6–8, 8–12 and 12–30 keV. The labels on the right are the corresponding time intervals of accumulated data. The 12–30 keV profiles are plotted with 20 phase bins due to lower count rate in this energy band.

powers in the first three Fourier harmonics. We find that the FPs remain fairly constant in time in all investigated energy intervals.

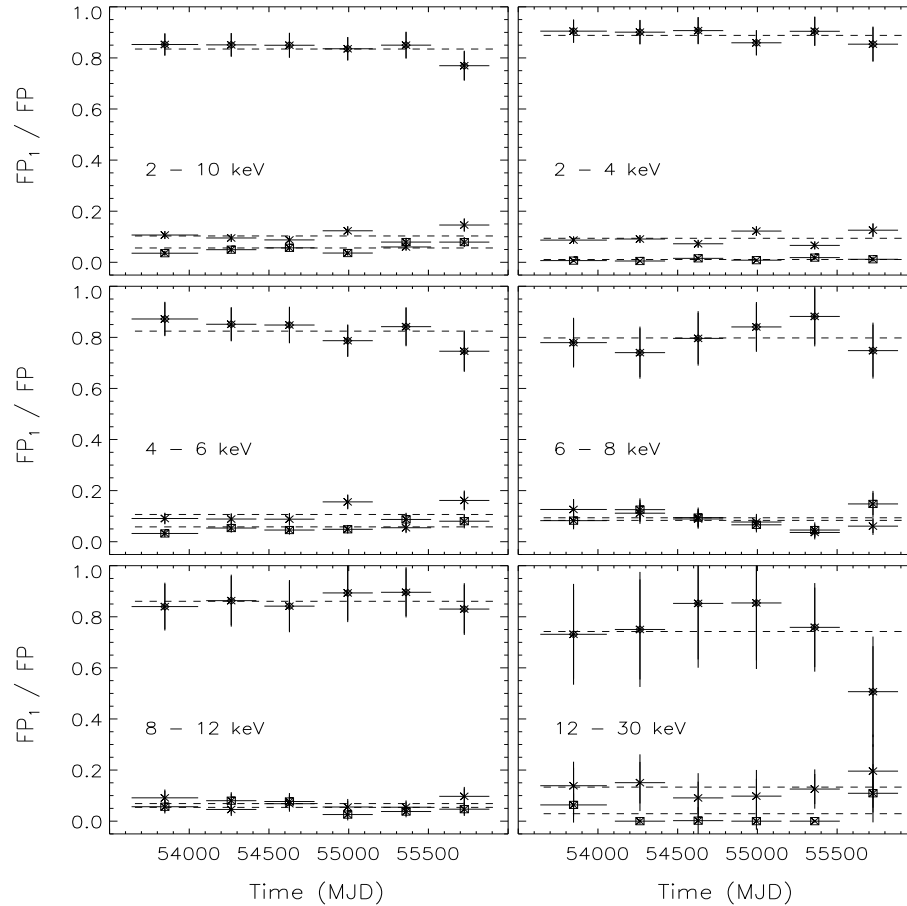


Figure 3.5: Time evolution of the normalized Fourier harmonic powers in the first three harmonics. Dashed lines represent the averaged power of the related harmonic in all segments. The energy intervals in which the powers are calculated are displayed inside the panels.

3.4.3 Pulsed Count Rates

PCA is not an imaging instrument; it collects all events originating within about 1° (FWHM) field centered near the position of 1RXS J170849.0-400910. Therefore, we cannot construct a precise X-ray light curve of the source using PCA observations since the accurate determination of X-ray background with the PCA is not possible. Nevertheless, we can trace the behavior of the pulsed X-ray emission of 1RXS J170849.0-400910 since there is no other pulsed X-ray source with exactly the same pulse period in the vicinity. X-rays originating from the other sources in the field of view (even the pulsed ones) are averaged out after folding the data with

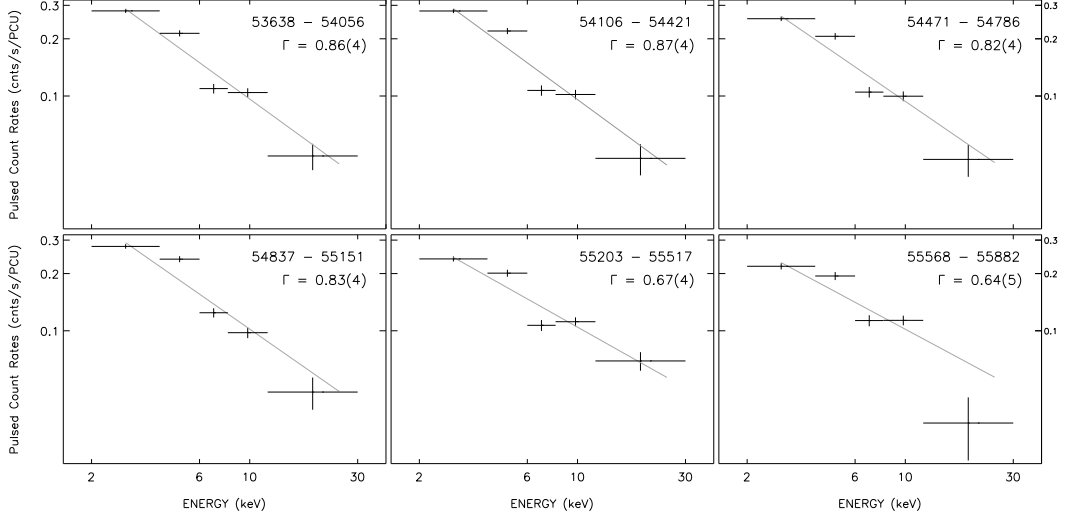


Figure 3.6: Plots of rms pulsed count rates vs. energy. Time intervals within which these plots were obtained are shown in the top-right of each panel. Solid lines show the best fit power law trends to the corresponding energy dependent rms pulsed count rates. Uncertainties in these power law indices refer to the last digit as shown in parenthesis in each panel.

the spin frequency of 1RXS J170849.0-400910 and remain within the DC level. For these reasons, we calculated the rms pulsed count rates of the source using

$$\text{PCR}_{\text{rms}} = \left(\frac{1}{N} \sum_{i=1}^N (R_i - R_{\text{ave}})^2 - \Delta R_i^2 \right)^{\frac{1}{2}} \quad (3.2)$$

$$\delta \text{PCR}_{\text{rms}} = \frac{1}{N \text{PCR}_{\text{rms}}} \left(\sum_{i=1}^N [(R_i - R_{\text{ave}}) \Delta R_i]^2 \right)^{\frac{1}{2}} \quad (3.3)$$

where R_i are the count rates in each phase bin, ΔR_i are their uncertainties, R_{ave} is their average and N is the number of phase bins. Note that this is a background exempt representation of pulsed intensity of the source.

In Figure 3.2(d) we present the time variation of rms pulsed count rates in the 2–10 keV energy range. Here, each pulsed intensity value is an average of about 1 month of data accumulation. We find that the rms pulsed count rate in the 2–10 keV band does not show any significant variation. Figure 3.6 presents the pulsed count rates as a function of energy (in other words, rough energy spectra of the pulsed X-ray emission from 1RXS J170849.0-400910). Power law fits to these rough energy spectra yield a general trend from a more steep shape to a more shallow one as time progresses.

3.4.4 Search for Glitches

There is no explicit glitch detected in our data sample as it can be seen from the fit results to the phase drifts in Table 3.1. To investigate whether there are any small amplitude variations in phase drifts (i.e. frequency jumps), we fitted phase shifts using the MPFITFUN¹ (Markwardt, 2009) procedure which performs Levenberg-Marquardt least-squares fit with the corresponding phases of a glitch model containing a jump in every ~ 0.1 day and a linear decay, as follows:

$$\nu(t) = \nu_0(t) + \Delta\nu + \Delta\dot{\nu}(t - t_g) \quad (3.4)$$

where $\nu_0(t)$ is the preglitch frequency evolution, $\Delta\nu$ is the frequency jump, $\Delta\dot{\nu}$ is the change of the frequency derivative after the glitch and t_g is the epoch of the glitch. First we applied this methodology to a previously published glitch in 2005 June and a candidate glitch in 2005 September. We detected the frequency jumps ($\Delta\nu$) and glitch epochs in agreement with the published values (Israel et al., 2007b; Dib et al., 2008). We then carried out the glitch search in all six epochs listed in Table 3.1 as follows: For each epoch, we analyzed the fit results on the $\Delta\nu$ versus the reduced χ^2 plane and identified the set of parameters corresponding to the lowest reduced χ^2 value. We then computed rms fluctuations of phase residuals using the possible glitch parameters and compared them with those obtained using the polynomial fit results listed in Table 3.1. We find that rms phase residual fluctuations with respect to the glitch model fits do not indicate any improvement in the fit quality compared to the polynomial fits (Figure 3.7). Moreover, the largest glitch amplitude ($\Delta\nu$) obtained is about 3×10^{-8} Hz in segments 0, 1 and 5 which could well be due to random fluctuations of phases, as can be seen in Figure 3.7.

Consecutive *RXTE* observations were typically performed at 7–10 day time intervals. Due to Sun constraints, there were five longer gaps of ~ 50 days in our data set. In order to assess the probability for the detection of a glitch that might have occurred during these longer gaps, we adopted the detectability criterion defined as (Alpar & Ho, 1983; Alpar & Baykal, 1994):

$$\delta\nu + \delta\dot{\nu} * \Delta t \ll \Delta\nu \quad (3.5)$$

where $\delta\nu$ and $\delta\dot{\nu}$ specify the total error on the spin frequency and frequency derivative determined on both ends of the gap, Δt denotes the duration of the gap, and $\Delta\nu$ is the change in spin frequency due to a putative glitch. Equation 3.5 implies that $\Delta\nu$ has to be much bigger than maximum error accumulated across the gap in order to identify it as a possible glitch event. We calculated the total error for

¹<http://purl.com/net/mpfit>

each gap adopting the timing solutions on both sides of the gaps, and present these results in Table 3.2.

We then applied the glitch search methodology to ~ 250 day-long data segments centered around each gap (gap segment), and evaluated minimum χ^2 searches as explained above. Best-fit timing solutions are listed in Table 3.2. Among all gaps, only glitch amplitudes in gap segment 3 (54687–54913) and gap segment 5 (55406–55666) satisfy condition 3.5. In particular, the glitch amplitude in gap segment 5 is ~ 7 times larger than the noise criterion which makes it a rather strong candidate for a possible glitch event. The putative glitch identified in gap segment 3 has an amplitude ~ 4 times larger than the corresponding minimum noise criterion. The amplitudes of estimated glitch events in gap segments 1, 2 and 4 possess large errors. The rms fluctuations of phase residuals in gap segments are similar in gap segments 1, 2, 3, and 5, while they are much larger in gap segment 4. Note that glitch amplitude in gap segment 4 is affected from an outlier phase measurement (see Figure 3.8), without which the glitch amplitude becomes even less significant. We, therefore, identified two glitch candidates; a strong case in the gap segment 5, and another one in gap segment 3 which is slightly less robust. We discuss their implications below.

Table 3.2: Timing Solutions in the Segments (Including the Gaps)^a

Parameter	Gap Segment 1	Gap Segment 2	Gap Segment 3	Gap Segment 4	Gap Segment 5
Range (MJD)	53952.558–54190.841	54323.309–54575.557	54687.314–54913.097	55048.230–55307.736	55405.757–55665.660
Epoch (MJD)	54106.040	54471.050	54836.804	55202.849	55567.977
Number of TOAs	29	31	27	28	31
ν (Hz)	0.0908775775(8)	0.090872564(1)	0.090867525(2)	0.090862442(2)	0.090857270(4)
$\dot{\nu}$ (10^{-13} Hz s $^{-1}$)	–1.617(2)	–1.584(2)	–1.590(4)	–1.646(3)	–1.638(4)
t_g (MJD)	54174.105	54531.016	54818.531	55245.277	55532.328
$\Delta\nu$ (10^{-8} Hz)	8(4)	2(2)	6.4(4)	4(1)	12.4(3)
$\Delta\dot{\nu}$ (10^{-15} Hz s $^{-1}$)	–43(56)	9(9)	–3(1)	–10(4)	–4.3(8)
rms (phase)	0.0151	0.0165	0.0170	0.0264	0.0156
Gap Range (MJD)	54056–54106	54422–54471	54786–54836	55151–55202	55517–55567
Gap Criterion (10^{-8} Hz)	2.31	2.15	1.76	0.73	1.74

^a Values in parenthesis are the uncertainties in the last digits of their associated measurements.

3.5 Discussion and Conclusions

We performed detailed long-term timing studies of 1RXS J170849.0-400910 spanning ~ 6 yr. Together with the earlier extensive study of the source by Dib et al. (2008), our investigation considers the entire database of *RXTE* observations of 1RXS J170849.0-400910. In our long-term timing investigations, it was possible to describe the phase shifts with a second order polynomial in only one interval (Segment 4 in Table 3.1), while all other parts required higher order terms. These results are similar to what has been obtained by Dib et al. (2008), Archibald et al. (2008), and Israel et al. (2007b), confirming the fact that 1RXS J170849.0-400910 is indeed a noisy pulsar.

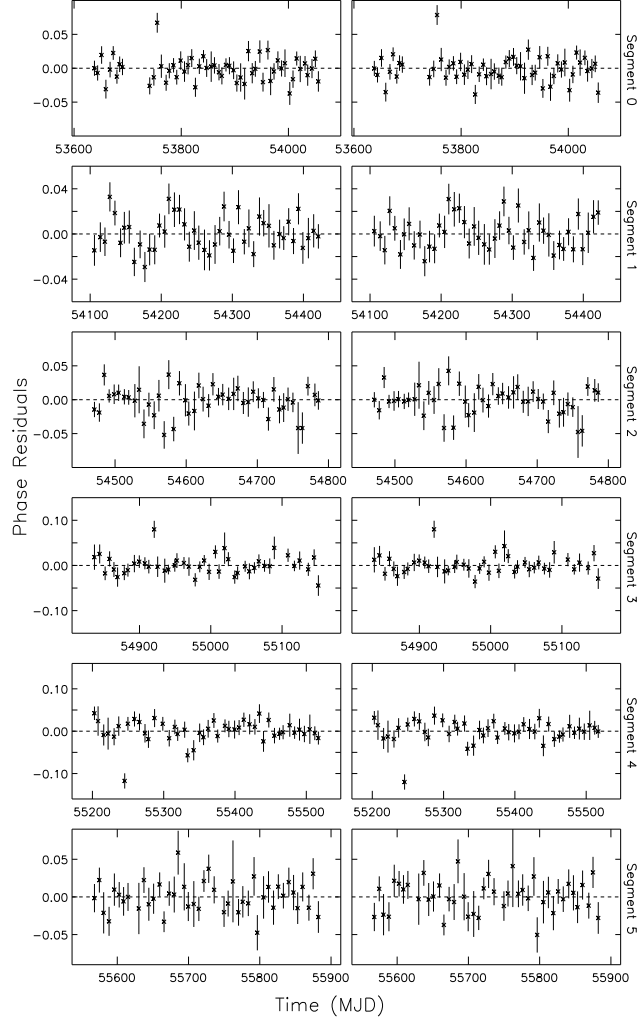


Figure 3.7: *Left column:* Phase residuals of the polynomial fit to each data segment. *Right column:* Phase residuals of the glitch model fit.

The pulse profile of 1RXS J170849.0-400910 in the 2–10 keV band does not show any significant variations over the last ~ 6 yr, maintaining its general pulse structure as in the earlier epochs. A minor structure (described as a shoulder above) in the pulse profile below 4 keV becomes stronger with energy and dominates the pulse profiles above 8 keV, as also noted by den Hartog et al. (2008) regarding earlier observations of the source. We also find no significant changes in the rms pulsed count rates (i.e. a measure of the pulsed flux) in the 2–10 keV range. In these respects, 1RXS J170849.0-400910 exhibits an almost stable pulsed X-ray emission behavior. We constructed a coarse energy spectrum of the rms pulsed count rates for each observation segment and found that it becomes gradually harder with time, as indicated by a shallowing power law index.

As a result of ~ 14 yr of *RXTE* observations, three glitches with two different recovery characteristics were unveiled unambiguously, and three candidate glitches

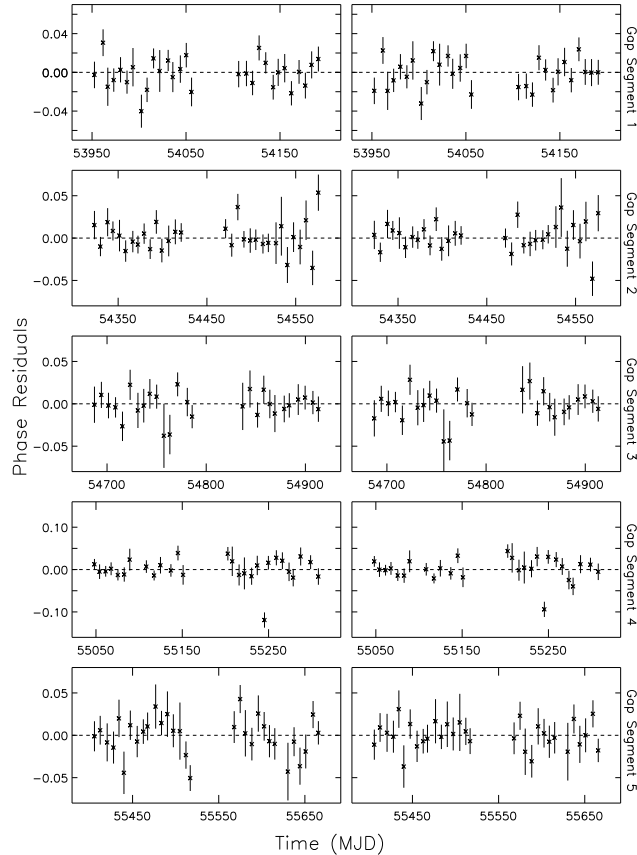


Figure 3.8: *Left column*: Phase residuals of the polynomial fit to each gap segment. *Right column*: Phase residuals of the glitch model fit.

were suggested in the time baseline between 1999 and 2005. Such a glitching behavior of 1RXS J170849.0-400910 made this system one of the most frequently glitching pulsars (Israel et al., 2007b; Dall’Osso et al., 2003; Dib et al., 2008). It is important to report the fact that, we do not find any unambiguous glitches in the time interval between 2006 and 2011. However, glitch search in the gaps yielded a strong candidate in gap 5 with glitch amplitude $\sim 10^{-7}$ Hz which is ~ 7 times larger than the noise in this gap and on the order of largest glitches observed from this source. We identified another candidate in gap segment 3, although it is slightly less robust.

Glitches are generally explained by models involving the neutron star crust, superfluid component of the inner crust or core superfluid and starquakes. The superfluid vortex unpinning model involves the crust and inner crust superfluid (Anderson & Itoh, 1975; Alpar et al., 1984b). In this model vortices formed by superfluid are pinned to the neutron-rich nuclei. While the crust spins down due to the electromagnetic torques, a rotational lag between the superfluid component and the crust builds up. When a critical value of rotational lag ($\delta\Omega \equiv \Omega_s - \Omega_c$, where Ω_s and Ω_c are the superfluid’s and crust’s angular velocity, respectively) is reached,

vortices suddenly unpin, resulting in transfer of angular momentum to the crust, i.e. glitch. This lag also determines the glitch occurrence time interval. This model is successful in explaining large glitches ($\Delta\nu/\nu \sim 10^{-6}$), such as those observed from the Vela pulsar with an occurrence time interval of ~ 2 yr (Alpar et al., 1981, 1984a).

Another class of models invokes starquakes, which are triggered by the cracking of the solid neutron star crust when growing internal stresses strain the crust beyond its yield point (Ruderman, 1969, 1976, 1991; Baym & Pines, 1971). This critical strain can be reached due to several mechanisms: the star spin down causes a progressive decrease of the equilibrium oblateness of the crust (Ruderman, 1969, 1991; Franco et al., 2000); variations of the core magnetic field, due to the motion of core superfluid vortices coupled to it (Srinivasan et al., 1990; Ruderman et al., 1998); and, in strongly magnetized neutron stars, the rapid diffusion of the core magnetic field (or the “turbulent” evolution of the crustal field) provides an alternative channel to produce crustal fractures (Thompson & Duncan, 1996; Rheinhardt & Geppert, 2002). Dall’Osso et al. (2003), based on the different recovery characteristics of the glitches of 1RXS J170849.0-400910, proposed that they can be explained by a magnetically-driven starquake model since they intrinsically involve local processes and a higher degree of complexity.

In order to discriminate between different possible models, Alpar & Baykal (1994) following Alpar & Ho (1983), investigated the global properties of large pulsar glitches using a sample of 430 pulsars, excluding the Vela pulsar. As these sources are not continuously monitored due to limited telescope times or other observational constraints, there are unavoidable data gaps in between successive pointings. This case puts a serious constraint on the detectability of a glitch if it occurs in a data gap of a pulsar with noisy timing behavior. They introduced a noise criterion (see Equation 3.5) for significantly detecting frequency jumps in the observational gaps. Therefore, they restricted their analysis to the 19 pulsar glitches with $\Delta\nu/\nu > 10^{-7}$. They estimated the physical parameters, e.g., inter-glitch time for the vortex unpinning model and the glitch size for the core-quake model. The parameters of the former model were estimated with two different assumptions for unpinning: First, the critical glitch parameter is taken as $\delta\Omega$ which is a representative of the number of vortices that is unpinned at the time of the glitch. Second, this parameter is taken as fractional density of the unpinned vortices that is proportional to $\delta\Omega/\Omega$, as the density of vortices $\propto \Omega$. They also assumed that the probability of observing n glitches is given by Poisson statistics. Glitch size estimation from the core-quake model is far bigger than the glitch amplitudes of the Vela pulsar and sample mean. Thus, their work statistically excluded the core-quake model. They also compared the parameter estimates of the vortex unpinning model with those of glitches from Vela and other pulsars, and concluded that the vortex unpinning model with a

constant fractional vortex density ($\langle\delta\Omega/\Omega\rangle$) is the most compatible model and can represent an invariant for glitches.

To test the glitch expectancy within the vortex unpinning model for 1RXS J170849.0-400910 glitches, we applied the same statistical glitch expectancy analysis (see Equation 11 of Alpar & Baykal, 1994) and estimated the expected number of glitches using ~ 14 yr of *RXTE* observations. We calculated the critical fractional vortex density of the vortex unpinning model by using the time span between 1998 January and 2005 November, which contains three glitches and three glitch candidates (Dib et al., 2008; Dall’Osso et al., 2003; Israel et al., 2007b). For a single pulsar, $\dot{\nu}/\nu$ value is not expected to fluctuate between observations. However, this is not the case for 1RXS J170849.0-400910 as it changes between $-1.87 \times 10^{-12} \text{ s}^{-1}$ and $-1.31 \times 10^{-12} \text{ s}^{-1}$ with an average value of $-1.66 \times 10^{-12} \text{ s}^{-1}$, which further implies the noisy timing characteristics of the source. Therefore, we performed our calculations for all these three values. First we included the observational gaps into the total time span which, by the chosen noise criterion, restricts our analysis to large glitches with $\Delta\nu/\nu$ on the order of 10^{-6} . Using $\dot{\nu}/\nu$ values and observed number of glitches with $\Delta\nu/\nu \sim 10^{-6}$ (i.e. $n = 2$), we obtain the upper, lower and average values for critical parameter value of the vortex unpinning model. We note an important fact here that a glitch candidate (i.e. near candidate glitch 2 in Dib et al., 2008) was reported by Israel et al. (2007b) with a fractional amplitude of 1.2×10^{-6} . If the latter report is correct, the number of large glitches in the 1998–2005 interval would be 3 (i.e. $n = 3$) which changes the critical parameter. Finally, we excluded all data gaps except the ones with glitches reported in them, and the ones that satisfied the noise criterion in our analysis, and we considered all reported glitches with $\Delta\nu/\nu \gtrsim 10^{-7}$ (i.e. $n = 6$) and calculated the critical parameters for this case as well. In Table 3.3 we list the values of the critical parameter for each of the above-mentioned cases and their corresponding expected number of glitches in the time intervals between 1998–2005, 1998–2011, and 2006–2011. As expected, the average value of the critical parameter yields the observed number of glitches in the 1998–2005 interval. We find that the total number of expected glitches with fractional amplitudes of $\gtrsim 10^{-6}$ ($n = 2$ in Table 3.3) varies between 3.2 and 4.6 if the time baseline spans until the end of the *RXTE* coverage of the source in 2011 November. The number of glitches in the 2006–2011 time range, where we found a strong candidate, were expected to range from 1.4 to 2.0. We then repeated the above procedure, this time excluding all data gaps except the ones with reported candidate glitches. In this case, the noise criterion allows consideration of all glitches with $\Delta\nu/\nu \sim 10^{-7}$ (i.e. $n = 6$), and we re-calculated the critical parameters (see Table 3.3).

Glitch expectancy analysis within the context of the vortex unpinning model sug-

Table 3.3: Critical parameter values and results of the expectancy analysis of 1RXS J170849.0-400910

Number of glitches (n)	Critical parameter ^a ($\langle\delta\Omega/\Omega\rangle$)	Expectancy of Glitches ^b		
		1998–2005	1998–2011	2006–2011
2	2.3×10^{-4}	1.8	3.2	1.4
	2.0×10^{-4}	2.0	3.6	1.6
	1.6×10^{-4}	2.5	4.6	2.0
3	1.5×10^{-4}	2.6	4.8	2.1
	1.4×10^{-4}	3.0	5.4	2.4
	1.1×10^{-4}	3.8	6.9	3.0
6	7.7×10^{-5}	5.3	9.2	3.8
	6.8×10^{-5}	6.0	10.4	4.2
	5.4×10^{-5}	7.6	13.2	5.4

^a The upper (top), average (middle) and lower values (bottom) for the critical parameter value of the vortex unpinning model.

^b Calculated using the average value of the $\dot{\nu}/\nu$ within the specified time range. Timing solutions before 2005 are taken from Dib et al. (2008).

gests that 1RXS J170849.0-400910 might have had, on average, two large glitches in 6 yr, corresponding to the interval of 2006–2011 (Table 3.3). The two significant glitch candidates we identified in gap segments are, therefore, important, since they comprise the observed number to match with the expectancy of the vortex creep model. As far as only glitch statistics is concerned, this case implies that the mechanism leading to the observed glitches in 1RXS J170849.0-400910 is internal. However, where particular glitch characteristics were concerned (e.g., discrepancies in glitch recovery), the vortex unpinning model is argued to be not sufficient (Dall’Osso et al., 2003).

1RXS J170849.0-400910 is the only member of the magnetar family that has not exhibited energetic X-ray bursts. Almost all other AXPs, that have experienced timing glitches, emitted energetic bursts either in conjunction with (e.g., 1E 2259+586, Woods et al., 2004) or contemporaneous to their glitches. It is, therefore, suggestive that a common mechanism might be responsible for both glitches and bursts. The dipole magnetic field strength of 1RXS J170849.0-400910 as inferred from its spin period and spin-down rate is about 4.6×10^{14} G, that is strong enough to produce significant deformation in the neutron star crust and eventually lead to the release of energy via bursts (Thompson & Duncan, 1995). Nevertheless, the condition on 1RXS J170849.0-400910 has not given rise to any observable bursts, even though it has experienced the largest number of glitches among all magnetars. While a common mechanism could reproduce coincident energetic bursts and glitches in general, it might be generating glitches but not detectable enhancements and bursts in 1RXS J170849.0-400910, possibly due to this source having slightly lower crust shear modulus, so that the release of less energy can still produce breaks in the crust. The energetic bursts, however, are not accounted for within the context

of the vortex unpinning model which appears to be favored for this source in our statistical investigations.

Recently Eichler & Shaisultanov (2010) suggested that vortices can be unpinned mechanically via oscillations rather than by a sudden heat release. According to their estimation, the relative velocity between the crust and superfluid, which is generated by the mechanical energy release at the depths below 100 m, can exceed the critical velocity lag and unpin the vortices. In order to explain the radiatively silent glitches seen in some AXPs (as in the case of 1RXS J170849.0-400910) they proposed that mechanically triggered glitch event might not be accompanied by a long-term X-ray brightening since a glitch can be triggered by less energy release. In this picture, the origin of X-ray brightening is also through mechanical energy release and these flux enhancements are expected to be accompanied with glitch events. This scenario can be diagnosed through the exact timing of glitches with radiative enhancements (Eichler & Shaisultanov, 2010).

Chapter 4

A Glitch and an Anti-glitch in the Anomalous X-ray Pulsar 1E 1841-045

This chapter was published in *Monthly Notices of the Royal Astronomical Society*, 2014, Volume 440, Pages 2916–2921 Şaşmaz Muş, S., Aydın, B., & Göğüş, E.

4.1 Abstract

We investigated long-term spin properties of AXP 1E 1841-045 by performing temporal analysis of archival *RXTE* observations spanning about 5.2 yr from 2006 September to 2011 December. We identified two peculiar timing anomalies within ~ 1 year apart from each other: A glitch with $\Delta\nu/\nu \sim 4.8 \times 10^{-6}$ near MJD 54303 and an anti-glitch with $\Delta\nu/\nu \sim -5.8 \times 10^{-7}$ near MJD 54656. The glitch we identified, which is the fourth glitch seen from this source in the 13 yr of *RXTE* monitoring, is characteristically similar to the last two previously detected glitches. On the other hand, we identified an anti-glitch from 1E 1841-045 for the first time. The amplitude of the anti-glitch was comparable with that recently observed from AXP 1E 2259+586. We found no significant variations in the pulsed X-ray output of the source during either the glitch or the anti-glitch. We discuss our results in relation to the standard pulsar glitch mechanisms for the glitch, and to plausible magnetospheric scenarios for the anti-glitch.

4.2 Introduction

Anomalous X-ray Pulsars (AXPs), along with Soft Gamma-Ray Repeaters (SGRs) are extremely magnetized neutron stars (magnetars) powered by the decay of their strong magnetic fields. These sources exhibit numerous unusual characteristics, such as, relatively slow rotation speeds, high spin-down rates, bright persistent X-ray emission and, for most of them, episodic bursts seen in X-rays (see, e.g., Rea & Esposito, 2011; Mereghetti, 2011, for recent reviews). The dipole magnetic field strengths, inferred from their spin periods and spin down rates are indeed extremely high, which are sufficient to account for their observed unique properties (Duncan & Thompson, 1992).

Long-term spin behavior of magnetars usually do not follow a secular trend, likely due to large magnetic torques along with episodic wind outflow that could take place in strongly magnetized environments (Thompson et al., 2000). Additionally, sudden increase in the angular velocity (i.e. glitches) has been observed from several AXPs. However, glitch events in AXPs have peculiar differences compared to the properties of glitches from rotation powered pulsars: 1E 1048.1-5937 is one of the most variable AXP both in timing and radiative behavior as several short energetic burst and flare events were observed (Gavriil et al., 2002, 2006; Tam et al., 2008; Dib et al., 2009). Its 2007 flare event was coincident with a large glitch (Dib et al., 2009). Similarly, 4U 0142+61 went into an active period, exhibiting six bursts and a glitch event that was over-recovered, causing the neutron star to rotate more slowly than before the glitch (Gavriil et al., 2011). Another AXP showing coincident burst and glitch

event is CXOU J164710.2-455216 (Krimm et al., 2006; Israel et al., 2007a; Muno et al., 2007; Woods et al., 2011). On the other hand, 1RXS J170849.0-400910 and 1E 1841-045 displayed glitches, but there has been no evidence of accompanying radiative enhancements in these sources (Kaspi et al., 2000; Kaspi & Gavriil, 2003; Dall’Osso et al., 2003; Israel et al., 2007b; Dib et al., 2008; Şaşmaz Muş & Göğüş, 2013).

1E 2259+586 has shown an outburst in association with a glitch (Kaspi et al., 2003; Woods et al., 2004). More interestingly, this source exhibited a sudden decrease in its angular velocity, i.e. an anti-glitch (Archibald et al., 2013b) within two weeks from a hard X-ray burst (Foley et al., 2012). The sudden spin-down trend in this AXP has been in conjunction with a doubled persistent source flux (Archibald et al., 2013b). These authors also report that the observed anti-glitch was followed by either a glitch event ~ 90 d later or by a second anti-glitch ~ 50 d later. Recently, Hu et al. (2014) suggested that the two anti-glitch explanation is more plausible based on a Bayesian approach. Unlike glitches observed from isolated neutron stars, which are generally attributed to an internal mechanism (e.g, Anderson & Itoh, 1975; Alpar, 1977), anti-glitch event was explained in terms of external effects, including magnetospheric processes (Lyutikov, 2013; Tong, 2014; Katz, 2014) or accretion of orbiting objects (Katz, 2014; Ouyed et al., 2014; Huang & Geng, 2014).

1E 1841-045 has a pulse period of ~ 11.8 s. It is a bright persistent X-ray source with an emission spectrum extending into hard X-rays, up to about 150 keV (Kuiper et al., 2004). It is also a source of several short energetic magnetar bursts (Kumar & Safi-Harb, 2010; Lin et al., 2011; Collazzi et al., 2013; Pal’shin et al., 2013). Three glitches have been observed from 1E 1841-045 with amplitudes ranging from $\sim 10^{-7}$ Hz to 1.2×10^{-6} Hz (Dib et al., 2008). Note that these events were radiatively silent, i.e. there was no significant variation of the radiative behavior of the source associated with these timing anomalies (Dib et al., 2008; Zhu & Kaspi, 2010). The persistent X-ray emission of 1E 1841-045 has remained constant during the duration of energetic bursts (Lin et al., 2011; Archibald et al., 2013a).

Here, we present the results of long-term timing analysis of 1E 1841-045 using Rossi X-ray Timing Explorer (*RXTE*) observations spanning ~ 5.5 yr. In the following section, we introduce these *RXTE* observations and our data analysis scheme. In §4.4, we present the results of our detailed temporal investigations, and report on the discovery of an anti-glitch and additional glitch from this source. We then discuss our findings in §4.5.

Table 4.1: Pulse Ephemeris of 1E 1841-045^a

Parameters Name	Segment 0	Segment 1 ^b	Segment 2 ^b	Segment 3	Segment 4	Segment 5
Range (MJD)	53829 – 54076	54126 – 54431	54492 – 54807	54860 – 55168	55223 – 55538	55588 – 55903
Epoch (MJD)	53823.9694	54125.967	54491.992	54860.107	55223.090	55587.871
Number of fitted points	19	26	24	22	29	24
ν (Hz)	0.084868766(5)	<i>0.084861458(8)</i>	<i>0.084852295(8)</i>	0.084843233(2)	0.084834325(4)	0.084824920(3)
$\dot{\nu}$ (10^{-13} Hz s ⁻¹)	-2.82(1)	<i>-3.92(2)</i>	<i>-2.72(2)</i>	-2.834(1)	-2.883(7)	-2.943(6)
$\ddot{\nu}$ (10^{-22} Hz s ⁻²)	-5.6(9)	<i>187(4)</i>	<i>-23(4)</i>	-	-9.0(5)	-4.1(4)
$d^3\nu/dt^3$ (10^{-28} Hz s ⁻³)	-	<i>-12.4(3)</i>	<i>1.5(3)</i>	-	-	-
rms (phase)	0.0143	<i>0.1184</i>	<i>0.0210</i>	0.0160	0.0230	0.0226
χ^2/DOF	16/15	<i>1508.6/21</i>	<i>37.8/19</i>	19.1/19	46.6/25	40.6/20

^a Values in parentheses are the uncertainties in the last digits of their associated measurements.

^b These spin parameters written in italics yield unacceptable fits to data but are listed here in order to illustrate the inadequacy of the polynomial model.

4.3 Observations and Data Processing

1E 1841-045 has been observed with *RXTE* in 279 occasions over a time span of ~ 13 yr from 1999 February to 2011 December¹. Data covering the first ~ 7.6 yr have already been investigated by Dib et al. (2008). Here, we investigated 137 *RXTE* observations performed from 2006 September 19 to 2011 December 8 for the first time. Additionally, we also included the last 12 (2006 April 3 - 2006 September 5) *RXTE* pointings in the sample of Dib et al. (2008) in order to link our long-term timing results with their extensive coverage. Exposure times of these 149 pointings were between ~ 1.2 ks and ~ 9.6 ks with a mean of ~ 4.6 ks and spacing between successive pointings varied between 0.04 and 61 days with an average of 14 days.

We employed data collected with the Proportional Counter Array (PCA), that was an array of nearly identical five proportional counter units (PCUs) operated optimally in the energy range of 2–30 keV (Jahoda et al., 2006). We first filtered each observation for occasional bursts, data anomalies and instrumental rate spikes by screening their light curves in the 2–30 keV band with the 31.25 ms time resolution. We then converted the arrival times of the remaining events to the Solar system barycenter. In order to maximize the signal-to-noise ratio for timing analysis of 1E 1841-045, we selected events in the 2–11 keV energy range recorded at the top Xenon layer of each operating PCU in GoodXenon mode, as was also done by Dib et al. (2008).

4.4 Data Analysis & Results

In order to undertake a coherent timing analysis, we grouped all 149 observations into six segments intercepted with observational interruptions in between due to Solar constraints. In addition, we merged observations together if the time spacing

¹The complete list of *RXTE* observations as well as pointing details can be obtained from the High Energy Astrophysics Science Archive Research Center of NASA at <http://heasarc.gsfc.nasa.gov>.

between them was less than 0.1 d. In this grouping scheme, segment 0 has 12 observations which are the last *RXTE* pointings used by Dib et al. (2008). We first generated a high signal-to-noise ratio pulse profile template using a subset of observations (typically five or six) from the beginning of each segment. We obtained the pulse profile for each observation by folding light curves with a nominal spin frequency. We then cross-correlated the pulse profiles with the template and measured their phase shifts with respect to the template. Finally, we fitted the phase shifts with a polynomial of the following form:

$$\phi(t) = \phi_0(t_0) + \nu_0(t - t_0) + \frac{1}{2}\dot{\nu}_0(t - t_0)^2 + \dots, \quad (4.1)$$

where t_0 is the epoch time. We found that all segments, except for Segment 1 and Segment 2, are fitted well with polynomials of the third order or lower. We present the results of polynomial model fits to each segment in Table 4.1. We note that the spin frequency and spin-down rate of Segment 0 are consistent with those reported by Dib et al. (2008). In Table 4.1, we also list root-mean-square (rms) fluctuations of the resulting phase residuals, which are presented in the top panel of Figure 4.1. A 4th order polynomial fit to pulse arrival times in Segment 1 yields extremely large fit statistics (χ^2 of 1508.6 for a degrees of freedom (DOF) of 21; see Figure 4.1 top panel and Figure 4.2 panel b). We therefore identified this segment to search for glitch(es), as we describe in detail below.

We fitted the pulse arrival times of Segment 2 with a 4th order polynomial but obtain unacceptable fit statistics ($\chi^2/DOF = 37.8/19$). We note the fact that there are systematic variations of the phase residuals around MJD 54650. A higher-order polynomial fit to this segment results in lower fit statistics, whereas the errors of derived spin parameters become large. For these reasons, we also investigated this segment for timing anomalies.

We found that arrival times of Segment 3 can be represented with a second order polynomial, that is the lowest order we obtained among our investigation span of 5.5 yr. We also found that the frequency derivatives² within this segment remain constant (see the middle panel in Figure 4.1). For Segments 4 and 5, we obtained adequate fit with a third-order polynomial. However, the rms phase residual fluctuations for these segments are larger than other segments, namely Segments 0 and 3. Note the important fact that energetic short-duration bursts from this magnetar were observed during Segments 4 and 5; they are denoted with vertical solid lines in Figure 4.1.

In order to determine whether the large fluctuations in the phase residuals of Segments 1, 2, 4 and 5 are due to a sudden change in the spin frequency of the source,

²Frequency derivatives are obtained by fitting a second order polynomial to subset of observations of ~ 2 months long

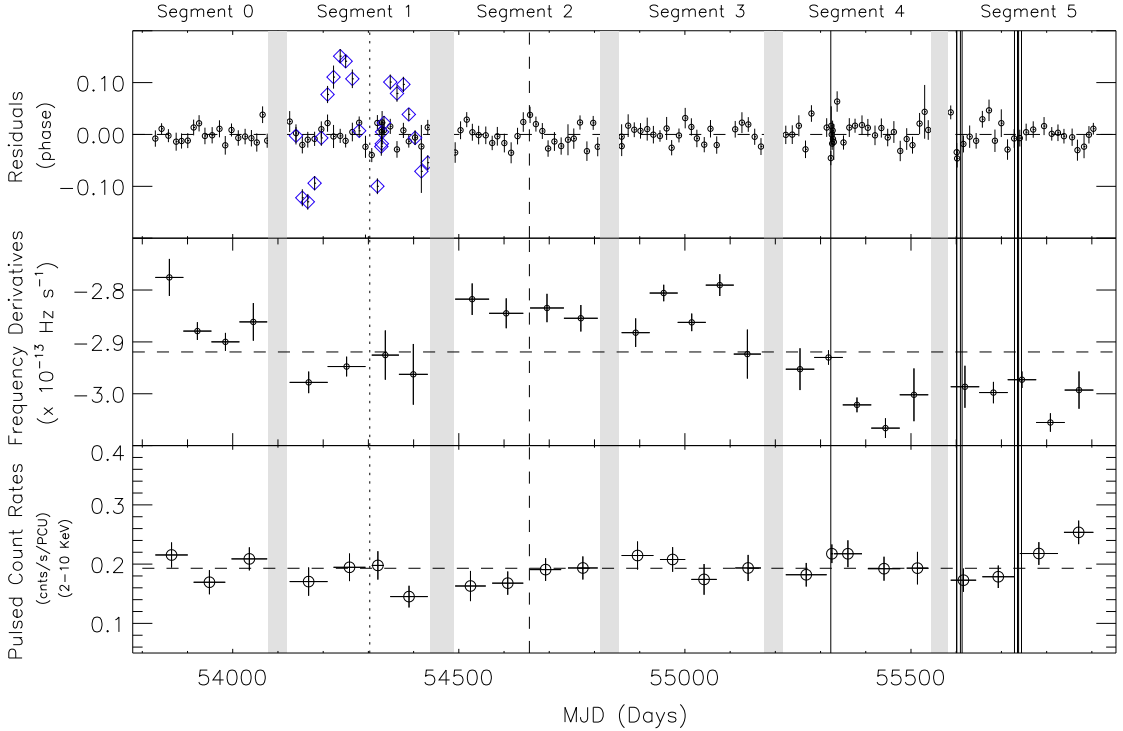


Figure 4.1: *Top panel:* Phase residuals after the subtraction of the polynomial models presented in Table 4.1 from data. For Segment 1 we present the phase residuals after subtraction of the polynomial model (blue diamonds) presented in Table 4.1 and glitch model presented in Table 4.2 (see Figure 4.2 for more detailed presentation of this segment). *Middle panel:* Frequency derivative evolution of the source. *Bottom panel:* Evolution of the pulsed count rates in the 2–10 keV band. The times of glitch 4 and anti-glitch are shown with the vertical dotted and dashed lines, respectively. Solid vertical lines indicate the times of energetic bursts listed in table 1 of Lin et al. (2011). Data gaps are indicated with light gray bars.

we fitted phase shifts of these segments using MPFITFUN routine (Markwardt, 2009) with a model involving a quadratic polynomial and a sudden change of spin frequency (i.e. glitch). The corresponding spin trend of this model is:

$$\nu(t) = \nu_0(t) + \Delta\nu + \Delta\dot{\nu}(t - t_g) \quad (4.2)$$

Here t_g is the time of the glitch. $\Delta\nu$ is the change in the frequency at the time of the glitch. $\Delta\dot{\nu}$ is the frequency derivative change after the glitch and $\nu_0(t)$ is pre-glitch frequency evolution.

In Segment 1, we found that a model involving a glitch provides statistically significant improvement in fitting the phase shifts ($\chi^2/DOF = 31.6/21$). We, therefore, conclude that there is a glitch at MJD ~ 54303 with an amplitude of $\Delta\nu \sim 4 \times 10^{-7}$ Hz. This is the 4th glitch observed from 1E 1841-045. We present the parameters for Glitch 4 in Table 4.2. Note that the amplitude of this glitch is on the

Table 4.2: Parameters for Glitch 4^a

Range (MJD)	54126–54431
Epoch (MJD)	54125.967
Number of fitted points	26
ν (Hz)	0.084861236(2)
$\dot{\nu}$ (10^{-13} Hz s ⁻¹)	-2.965(3)
t_g (MJD)	54303(3)
$\Delta\nu$ (10^{-8} Hz)	40.7(6)
$\Delta\dot{\nu}$ (10^{-15} Hz s ⁻¹)	1.2(7)
rms (phase)	0.0174
χ^2/DOF	31.6/21

^a Values in parentheses are the uncertainties in the last digits of their associated measurements.

order of last two glitches observed from this source (see Dib et al., 2008). We also present the phase residuals of the polynomial model and glitch model for comparison in Figure 4.2.

As noted earlier, pulse phase modeling of the Segment 2 with a fourth-order polynomial yields an unacceptable fit statistics (see panel c of Figure 4.3), while increasing the order of the polynomial results in unconstrained spin parameters. For this reason, we also modeled the phases of this segment with a glitch model. We found that an ordinary glitch model fit does not improve the fit statistics. However, a glitch with a negative amplitude (i.e. an anti-glitch) of $\Delta\nu \sim -5 \times 10^{-8}$ Hz provides a significant improvement in fit statistics ($\chi^2/\text{DOF} = 16.3/19$); a $\Delta\chi^2$ of 21.5 for the same number of DOF as the polynomial model fit. Based on this, we conclude that 1E 1841-045 exhibited an anti-glitch near MJD 54656, that is ~ 1 yr after Glitch 4. We list the parameters of the anti-glitch model fit in Table 4.3. Note that fit results suggesting the anti-glitch epoch between MJD 54645 and 54662 yield similar statistics.

In the top panel of Figure 4.3 we present the frequency evolution of the source in this segment. To show the sudden deviation of the spin frequency, we fitted a linear trend to the frequencies prior to MJD ~ 54650 and extrapolated this fit to the rest of this segment (see panel b in Figure 4.3). We found that the spin-down rate before MJD 54630 and after MJD 54670 are consistent with one another ($-2.84(1) \times 10^{-13}$ and $-2.86(1) \times 10^{-13}$ Hz s⁻¹, respectively). The average spin-down rate during about 40 days in between is about -3×10^{-13} Hz s⁻¹. We also present the phase residuals of the model including the anti-glitch in the panel d of Figure 4.3.

Fits to the pulse arrival times of Segment 4 and 5 with models involving a glitch or anti-glitch did not yield any improvement in the fit statistics. We therefore conclude that the system exhibits higher level of timing noise, likely related to the

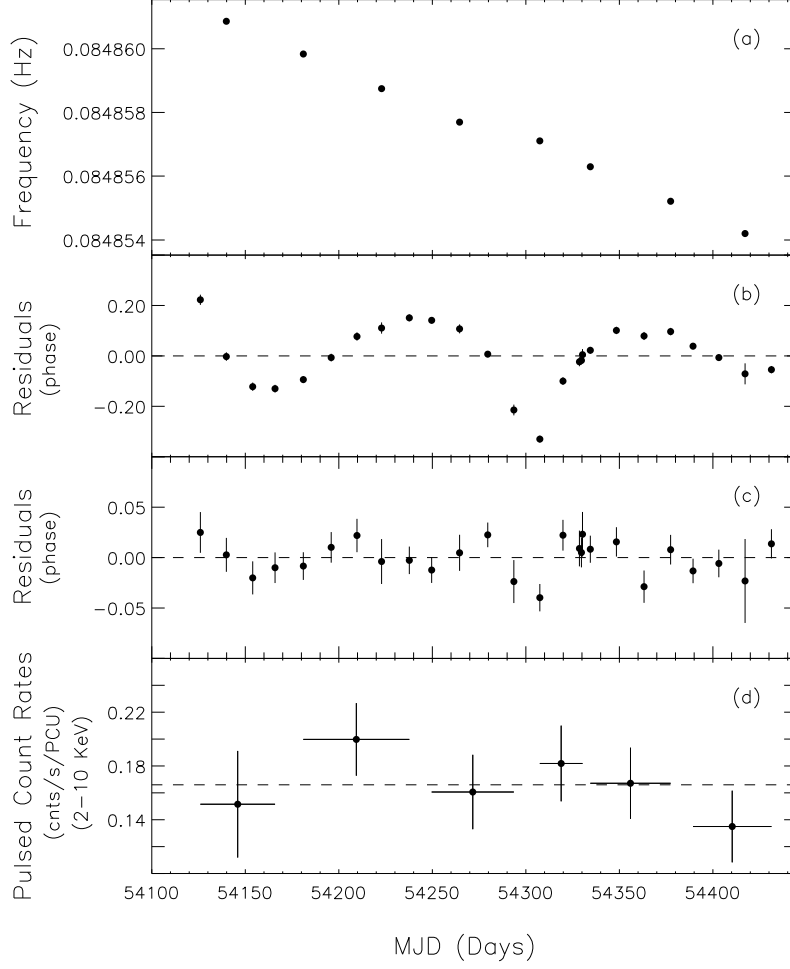


Figure 4.2: (a) Spin frequency evolution of the source during Segment 1. (b) Phase residuals after the subtraction of a fourth order polynomial model from the data. (c) Phase residuals after subtracting the glitch model. (d) Pulsed count rates of the source in the 2–10 keV band obtained using sets of observations spanning mostly over 40–50 days to ensure significant pulsed flux measurement.

Table 4.3: Parameters for Anti-glitch^a

Range (MJD)	54492–54807
Epoch (MJD)	54491.992
Number of fitted points	24
ν (Hz)	0.084852317(2)
$\dot{\nu}$ (10^{-13} Hz s ⁻¹)	-2.833(3)
t_g (MJD)	54656.0
$\Delta\nu$ (10^{-8} Hz)	-4.9(6)
$\Delta\dot{\nu}$ (10^{-15} Hz s ⁻¹)	-1.8(6)
rms (phase)	0.0139
χ^2/DOF	16.3/19

^a Values in parentheses are the uncertainties in the last digits of their associated measurements.

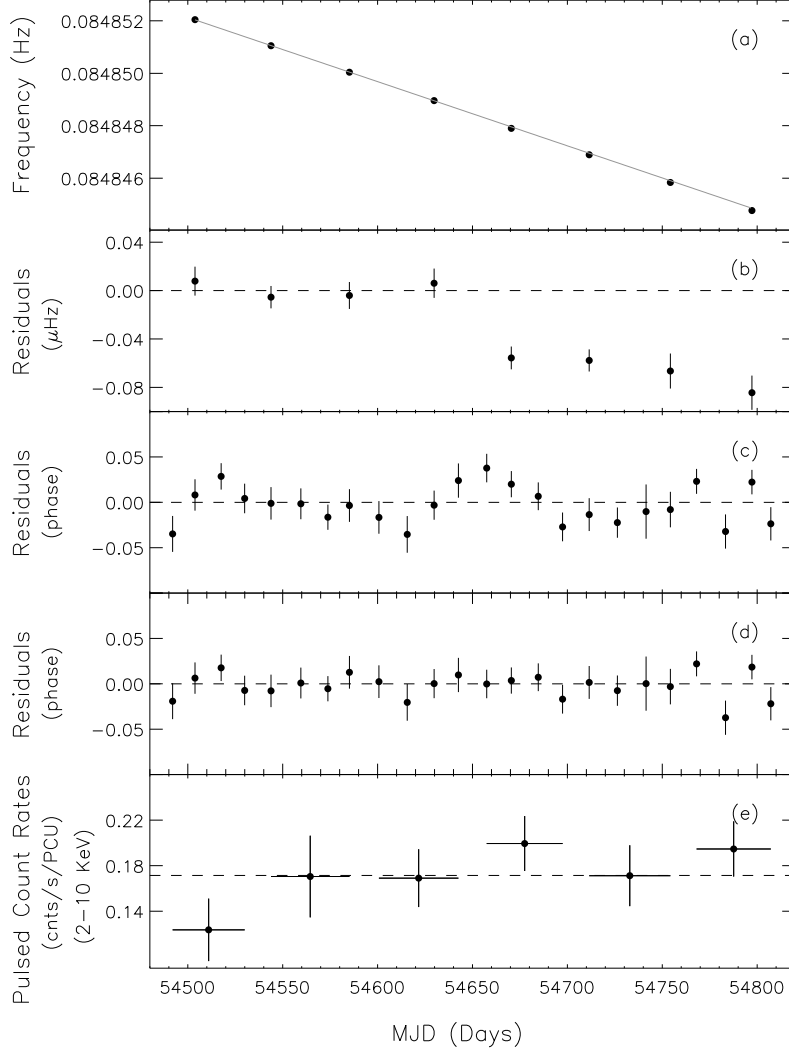


Figure 4.3: (a) Spin frequency evolution of the source during Segment 2. The solid line is the spin-down trend obtained by fitting the observations before MJD ~ 54630 , and extrapolated onwards. (b) Residuals of the model and its extrapolation in (a). (c) Phase residuals after the subtraction of a fourth order polynomial fit presented in Table 4.1. (d) Phase residuals after the subtraction the glitch model presented in Table 4.3 (e) The pulsed count rates in 2–10 keV averaged over ~ 40 days.

emission of numerous energetic bursts during these episodes (see Figure 4.1).

Finally, in order to search for radiative variabilities we performed pulsed count rate analysis as explained in Şaşmaz Muş & Göğüş (2013). We found that pulsed count rate of the source is constant over ~ 5.5 yr of *RXTE* observations (see third panel of Figure 4.1).

4.5 Discussion and Conclusions

1E 1841-045 was observed ~ 13 yr by *RXTE*. We performed timing analysis of 1E 1841-045 using ~ 5 yr of *RXTE* observations. Previous ~ 7.6 yr has been analyzed

by Dib et al. (2008) and 3 glitches have been reported. Largest glitch observed from this source has an amplitude of $\sim 1.2 \times 10^{-6}$ Hz with a recovery timescale of 43 days and fractional increase of 0.1 in its spin-down rate. Consequent two glitches have amplitudes on the order of $\sim 10^{-7}$ Hz without any observable exponential recovery. There is no evidence of accompanying radiative enhancements during all three glitch epochs.

Through our detailed investigations of *RXTE* monitoring of 1E 1841-045 spanning over five years, we have identified two timing events separated by ~ 1 yr: a glitch and an ‘anti-glitch’. The glitch event has occurred at MJD ~ 54303 with an amplitude of $\Delta\nu \sim 4 \times 10^{-7}$ Hz without any observable exponential recovery. Note that this marks the fourth glitch identified from this source: one of the earlier three has an amplitude of $\sim 10^{-6}$ Hz with a recovery timescale of 43 days, while the other two were at similar amplitudes and showed no exponential recovery (Dib et al., 2008). Similar to the three earlier glitch episodes in 1E 1841-045, we found no associated radiative enhancement deduced from the pulsed X-ray flux measurement (bottom panels of Figures 4.1 and 4.2).

The second event, an anti-glitch seen from 1E 1841-045 for the first time, has occurred at MJD ~ 54656 with an amplitude of $\Delta\nu \sim -5 \times 10^{-8}$ Hz. The amplitude of the only other anti-glitch event observed from 1E 2259+586 (Archibald et al., 2013b) is strikingly similar. We found that the source experienced an elevated spin-down rate over about 40 days, and $\dot{\nu}$ returned back to the pre-anti-glitch level after MJD 54670. Note that the average spin-down rate in the elevated regime is about -3×10^{-13} Hz s $^{-1}$, that is similar to the $\dot{\nu}$ values exhibited by the source over ~ 150 days following an energetic burst on MJD 55322.6 (see the middle panel of Figure 4.1). Both pulsed X-ray emission (see the bottom panel of Figure 4.3) and the 0.5–10 keV flux (see figure 3 of Lin et al., 2011) of the source remain constant during the anti-glitch episode, similar to the case for the fourth glitch.

According to the standard pulsar glitch models (see, e.g., Anderson & Itoh, 1975; Alpar, 1977), a faster-rotating superfluid transfers angular momentum to the crust, which results in positive increment in the observed spin frequency of the neutron star. Alpar & Baykal (1994) statistically determined that superfluid vortex unpinning model with a constant fractional vortex density, which is the fraction of vortex density involved in the glitch event, provides the most plausible explanation for glitches observed from rotation powered pulsars. In this model, the number of glitches in a given time span that a pulsar would experience is related to the constant fractional vortex density, the ratio of the spin-down rate and frequency of the pulsar. From previous observations and glitches observed from 1E 1841-045 we determined the fractional vortex density as 2.90×10^{-4} . Note that this is consistent with fractional vortex density for 1RXS J170849.0-400910 (Şaşmaz Muş & Göğüş,

2013). Using this parameter for 1E 1841-045 and an average value of the ratio of the spin-down rate to the frequency yield the expected number of glitches from this magnetar during the entire 13 yr of *RXTE* observation span as 4.5. With the fourth glitch we uncovered in this study, our results are in agreement with the expectations of the vortex unpinning model.

Recent observation of the anti-glitch from 1E 2259+586 implies a neutron star superfluid interior that is rotating more slowly than the crust within the context of standard pulsar glitch models (Archibald et al., 2013b; Anderson & Itoh, 1975). It has been suggested that the rotation of the superfluid can be slowed down by crustal deformations arising from magnetic stresses in highly magnetized sources (Thompson et al., 2000; Duncan, 2013). Thompson et al. (2000) suggest that 1E 2259+586 and 1E 1841-045 might have had episodes of accelerated spin-down owing to the fact that they are older than their associated supernovae remnants as inferred by their characteristic ages. Thompson et al. (2000) also proposed a particle outflow scheme to account for the sudden spin-down behavior of SGR 1900+14³ (Woods et al., 1999), in conjunction with its August 27 giant flare. However, there was no indication of particle outflow from 1E 2259+586 around the time of the anti-glitch (Archibald et al., 2013b). For this reason, the particle outflow scenario was discarded. Alternatively, there are already a couple of magnetospheric models suggested to understand the origin of the anti-glitch: Lyutikov (2013) proposed that the sudden spin-down and in general variable spin-down trends are caused by the changes in torque due to transient opening of a small region of the twisted magnetosphere during the X-ray burst. Tong et al. (2013); Tong (2014) have applied the wind braking scenario (Michel, 1969; Harding et al., 1999; Thompson et al., 2000) to magnetars in the case that the rotational energy of the star is mainly extracted via a constant particle wind from the star. In this model, an anti-glitch corresponds to an enhanced state of the particle wind (Tong, 2014). Both partial magnetospheric opening and wind braking models require radiative enhancements accompanying the anti-glitch, which was the case for 1E 2259+586 as its X-ray flux increased by at least a factor of 2 coinciding with the anti-glitch (Archibald et al., 2013b). Our results, however, place an indirect constraint on both models since we find no observable variations in the pulsed X-ray emission from 1E 1841-045 at the time of its anti-glitch. Nevertheless, occasional detection of energetic bursts from 1E 1841-045 indicate that its magnetosphere is active and not all but some X-ray bursts may lead to a magnetospheric rearrangement that could lead to the episodic rapid spin-down as prescribed by Lyutikov (2013).

Note the fact that we became aware of the paper by Dib & Kaspi (2014) during

³The rapid spin-down trend in SGR 1900+14 can be considered as the first observational manifestation of an anti-glitch, though the sparsity of observations did not allow definitive confirmation.

the review stage of our paper. They fit a very wide data segment (spanning more than 1200 days that includes our suggested anti-glitch) with a fifth order polynomial, and find an rms of 0.041, which is much larger than their any other segments. Even with the fifth order polynomial fit, large fluctuations in the phase residuals are clearly visible (see panel (c) around MJD 54600 of figure 1 in Dib & Kaspi, 2014). They make no comment on this significant timing anomaly, which we interpret as an anti-glitch.

Chapter 5

Summary and Outlook

In this thesis, we searched for persistent and pulsed gamma-ray emission from one of the brightest magnetars in X-rays, 4U 0142+61, using *Fermi*/LAT observations. Our search did not yield any detection of gamma-ray emission. However, we placed upper limits on persistent and pulsed emission of 4U 0142+61 in the 0.2–10 GeV range. We also placed an upper limit on the spectral break energy of the source as ~ 1 MeV. Together with the earlier works on soft and hard X-ray emission of 4U 0142+61, these upper limits provide a hint on the spectral shape of the source in a wide energy band. It is noteworthy that this study resulted in the first paper in the literature on the very high-energy characteristics of a magnetar. After this work was published, Fermi collaboration published their results of persistent and pulsed gamma-ray emission search for thirteen magnetars which were consistent with our findings (Abdo et al., 2010). Enoto et al. (2011) estimated a lower limit of spectral break as 180 keV using data obtained with *Suzaku*. Recently, *MAGIC* telescopes observed 4U 0142+61 above 200 GeV which resulted in no detection (Aleksić et al., 2013).

Next, we worked on the timing properties of magnetars which is important for gathering information on the internal structure of these stars and their differences from other types of pulsars. For the sake of statistical analysis, we focused on 1RXS J170849.0-400910 and 1E 1841-045 which are observed to glitch frequently (Dib et al., 2008; Dall’Osso et al., 2003).

For the investigation of 1RXS J170849.0-400910 we used ~ 6 years and for 1E 1841-045 ~ 5.5 years of *RXTE* data that is available until the decommissioning of the satellite. Our investigation for glitches resulted in no clear detection in 1RXS J170849.0-400910. However, we found evidence of timing anomalies which we concluded to be significant glitch candidates by employing the noise criterion (Alpar & Ho, 1983; Alpar & Baykal, 1994). The fractional glitch amplitudes of these events are on the order of $\Delta\nu/\nu \sim 10^{-6}$. Following Alpar & Ho (1983) and Alpar & Baykal (1994), we employed a glitch expectancy analysis based on the vortex unpinning model. The

analysis suggests that the number of glitches that might be observed from this source in ~ 6 years is two which further implies that the glitch candidates are important since they fulfill the expectancy of the model. However, expectancy analysis needs to be discussed in detail when more unambiguous glitch samples become available.

We also searched for radiative variabilities in 1RXS J170849.0-400910. However, we couldn't find any evidence of a radiative event in the timeline of ~ 6 yr. 1RXS J170849.0-400910 has not been observed to exhibit bursts, in contrast to other members of the magnetar family. Although observations of timing anomalies coinciding with bursts (see, e.g., Woods et al., 2004) are suggestive for a common mechanism, at this stage there is no stringent evidence of a different glitch mechanism operating in this source. However, in terms of the observed glitch characteristics, such as glitch recovery, the vortex unpinning model is argued to be insufficient (Dall'Osso et al., 2003).

In the analysis of 1E 1841-045 we identified two peculiar timing anomalies ~ 1 year apart from each other: a glitch with $\Delta\nu/\nu \sim 4.8 \times 10^{-6}$ and an anti-glitch with $\Delta\nu/\nu \sim -5.8 \times 10^{-7}$. The glitch is the fourth glitch seen from this source in the ~ 13 years of *RXTE* monitoring and is characteristically similar to the last two previously detected glitches (Dib et al., 2008) from this source. On the other hand, we identified an anti-glitch from 1E 1841-045 for the first time. The amplitude of the anti-glitch is comparable with that of an anti-glitch recently observed from 1E 2259+586 (Archibald et al., 2013b). We find no significant variations in the pulsed X-ray output of the source during both the glitch and anti-glitch events. According to the glitch expectancy analysis, the number of glitches that might be observed from this source in 13 years of *RXTE* observations is 4.5. With the fourth glitch we uncovered in this study, our results are in good agreement with the expectations of the vortex unpinning model.

The only other clear example of an anti-glitch was observed from the magnetar 1E 2259+586 (Archibald et al., 2013b). Before that there was an evidence that SGR 1900+14 had undergone a period of spin-down during its giant flare in 1998, though the sparsity of observations made it difficult to understand the nature of this event (Woods et al., 1999). Similarly, 1E 2259+586 exhibited an increment of a factor of ~ 2 in its X-ray flux, coincident with the anti-glitch event (Archibald et al., 2013b). The coincident radiative events suggested that the mechanism for spin-down events might be external (Thompson et al., 2000; Archibald et al., 2013b). Particle outflow induced spin-down was proposed by Thompson et al. (2000) to explain the observed spin-down event of SGR 1900+14. However, search for particle outflow from 1E 2259+586 resulted in no detection (Archibald et al., 2013b). On the other hand, if the mechanism that caused the anti-glitch is internal, this can only be explained by a superfluid rotating slower than the crust (Archibald et al., 2013b;

Thompson et al., 2000; Duncan, 2013). The energetic bursts, however, are not accounted for within the context of the standard pulsar glitch models.

Recently, a couple of magnetospheric models were proposed in an attempt to explain the anti-glitch event both of which require a radiative enhancement accompanying the anti-glitch (Lyutikov, 2013; Tong, 2014). Although sparsity of observations limits detection of quickly recovered radiative enhancements, our results place an indirect constraint on these models since we found no observable variations in the pulsed X-ray emission from 1E 1841-045 at the time of its anti-glitch.

Further observations of such interesting events correlated with multiwavelength observations can provide new tests for glitch models and lead to the potential discovery of new mechanisms operating in these sources. The *Swift* satellite is monitoring 1E 1841-045 every 2–3 weeks. Investigating these observations for glitch and anti-glitch events can be the first step for achieving this goal. With the decommission of the *RXTE* satellite, *Swift* will provide important information on the mechanisms and statistics of the glitches. *Swift* has already provided the observation of an anti-glitch from 1E 2259+586 (Archibald et al., 2013b). Furthermore, combined with its spectral facilities, it can shed light on the relation of glitches with radiative enhancements.

Finally, the wide band energy spectrum of magnetars needs further investigation both from the observational and theoretical aspects and can provide stringent tests of hard X-ray/gamma-ray emission models. In order to pursue this goal, *Fermi* observations of these sources can be utilized which now contain more than 6 years of accumulated data.

Bibliography

- Abdo, A. A., Ackermann, M., Ajello, M., et al. 2010, *ApJ*, 725, L73
- Abdo, A. A., Ajello, M., Allafort, A., et al. 2013, *ApJS*, 208, 17
- Aleksić, J., Antonelli, L. A., Antoranz, P., et al. 2013, *A&A*, 549, A23
- Allen, J. F., & Misener, A. D. 1938, *Nature*, 141, 75
- Alpar, M. A. 1977, *ApJ*, 213, 527
- . 1999, *ArXiv Astrophysics e-prints*, astro-ph/9912228
- . 2001, *ApJ*, 554, 1245
- Alpar, M. A., Anderson, P. W., Pines, D., & Shaham, J. 1981, *ApJ*, 249, L29
- . 1984a, *ApJ*, 278, 791
- Alpar, M. A., & Baykal, A. 1994, *MNRAS*, 269, 849
- Alpar, M. A., Chau, H. F., Cheng, K. S., & Pines, D. 1996, *ApJ*, 459, 706
- Alpar, M. A., Cheng, A. F., Ruderman, M. A., & Shaham, J. 1982, *Nature*, 300, 728
- Alpar, M. A., & Ho, C. 1983, *MNRAS*, 204, 655
- Alpar, M. A., Pines, D., Anderson, P. W., & Shaham, J. 1984b, *ApJ*, 276, 325
- Anderson, G. E., Gaensler, B. M., Slane, P. O., et al. 2012, *ApJ*, 751, 53
- Anderson, P. W., & Itoh, N. 1975, *Nature*, 256, 25
- Antoniadis, J., Freire, P. C. C., Wex, N., et al. 2013, *Science*, 340, 448
- Archibald, A. M., Dib, R., Livingstone, M. A., & Kaspi, V. M. 2008, in *American Institute of Physics Conference Series*, Vol. 983, 40 Years of Pulsars: Millisecond Pulsars, Magnetars and More, ed. C. Bassa, Z. Wang, A. Cumming, & V. M. Kaspi, 265–267
- Archibald, R., Scholz, P., & Kaspi, V. 2013a, *The Astronomer’s Telegram*, 5420, 1
- Archibald, R. F., Kaspi, V. M., Ng, C.-Y., et al. 2013b, *Nature*, 497, 591
- Arons, J. 1979, *Space Sci. Rev.*, 24, 437

- Arons, J. 1981, in IAU Symposium, Vol. 94, Origin of Cosmic Rays, ed. G. Setti, G. Spada, & A. W. Wolfendale, 175–204
- Atwood, W. B., Bagagli, R., Baldini, L., et al. 2007, *Astroparticle Physics*, 28, 422
- Atwood, W. B., Abdo, A. A., Ackermann, M., et al. 2009, *ApJ*, 697, 1071
- Baade, W., & Zwicky, F. 1934, *Physical Review*, 46, 76
- Bahcall, J. N., & Wolf, R. A. 1965, *Physical Review*, 140, 1452
- Bardeen, J., Cooper, L. N., & Schrieffer, J. R. 1957, *Physical Review*, 106, 162
- Baring, M. G., & Harding, A. K. 2007, *Ap&SS*, 308, 109
- Baykal, A., & Swank, J. 1996, *ApJ*, 460, 470
- Baym, G., Bethe, H. A., & Pethick, C. J. 1971a, *Nuclear Physics A*, 175, 225
- Baym, G., Pethick, C., & Pines, D. 1969, *Nature*, 224, 673
- Baym, G., Pethick, C., & Sutherland, P. 1971b, *ApJ*, 170, 299
- Baym, G., & Pines, D. 1971, *Annals of Physics*, 66, 816
- Beloborodov, A. M. 2009, *ApJ*, 703, 1044
- . 2013, *ApJ*, 762, 13
- Beloborodov, A. M., & Thompson, C. 2007, *ApJ*, 657, 967
- Bethe, H. A., & Johnson, M. B. 1974, *Nucl. Phys. A*, 230, 1
- Burgay, M., Rea, N., Israel, G. L., et al. 2006, *MNRAS*, 372, 410
- Burgay, M., D’Amico, N., Possenti, A., et al. 2003, *Nature*, 426, 531
- Caballero, I., & Wilms, J. 2012, *Mem. Soc. Astron. Italiana*, 83, 230
- Cameron, A. G. W. 1959, *ApJ*, 130, 916
- Cameron, P. B., Chandra, P., Ray, A., et al. 2005, *Nature*, 434, 1112
- Camilo, F., Ransom, S. M., Halpern, J. P., & Reynolds, J. 2007a, *ApJ*, 666, L93
- Camilo, F., Ransom, S. M., Halpern, J. P., et al. 2006, *Nature*, 442, 892
- Camilo, F., Reynolds, J., Johnston, S., Halpern, J. P., & Ransom, S. M. 2008, *ApJ*, 679, 681
- Camilo, F., Cognard, I., Ransom, S. M., et al. 2007b, *ApJ*, 663, 497
- Camilo, F., Ransom, S. M., Peñalver, J., et al. 2007c, *ApJ*, 669, 561
- Campana, S., Rea, N., Israel, G. L., Turolla, R., & Zane, S. 2007, *A&A*, 463, 1047
- Chadwick, J. 1932, *Nature*, 129, 312

- Chamel, N., & Haensel, P. 2008, *Living Reviews in Relativity*, 11, 10
- Chatterjee, P., Hernquist, L., & Narayan, R. 2000, *ApJ*, 534, 373
- Cheng, K. S., Ho, C., & Ruderman, M. 1986a, *ApJ*, 300, 500
- . 1986b, *ApJ*, 300, 522
- Cheng, K. S., & Zhang, L. 2001, *ApJ*, 562, 918
- Collazzi, A. C., Xiong, S., & Kouveliotou, C. 2013, *GRB Coordinates Network*, 15228, 1
- Dall’Osso, S., Granot, J., & Piran, T. 2012, *MNRAS*, 422, 2878
- Dall’Osso, S., Israel, G. L., Stella, L., Possenti, A., & Perozzi, E. 2003, *ApJ*, 599, 485
- Damen, E., Magnier, E., Lewin, W. H. G., et al. 1990, *A&A*, 237, 103
- Daugherty, J. K., & Harding, A. K. 1982, *ApJ*, 252, 337
- Demorest, P. B., Pennucci, T., Ransom, S. M., Roberts, M. S. E., & Hessels, J. W. T. 2010, *Nature*, 467, 1081
- den Hartog, P. R., Kuiper, L., Hermsen, W., et al. 2008, *A&A*, 489, 245
- den Hartog, P. R., Kuiper, L., Hermsen, W., & Vink, J. 2004, *The Astronomer’s Telegram*, 293, 1
- Deutsch, A. J. 1955, *Annales d’Astrophysique*, 18, 1
- Dhillon, V. S., Marsh, T. R., Hulleman, F., et al. 2005, *MNRAS*, 363, 609
- Dib, R., & Kaspi, V. M. 2014, *ApJ*, 784, 37
- Dib, R., Kaspi, V. M., & Gavriil, F. P. 2008, *ApJ*, 673, 1044
- . 2009, *ApJ*, 702, 614
- Duncan, R. C. 2013, *Nature*, 497, 574
- Duncan, R. C., & Thompson, C. 1992, *ApJ*, 392, L9
- Durant, M., & van Kerkwijk, M. H. 2006, *ApJ*, 648, 534
- Eatough, R. P., Falcke, H., Karuppusamy, R., et al. 2013, *Nature*, 501, 391
- Eichler, D., & Shaisultanov, R. 2010, *ApJ*, 715, L142
- Eksi, K. Y., & Alpar, M. A. 2003, *ApJ*, 599, 450
- Enoto, T., Makishima, K., Nakazawa, K., et al. 2011, *PASJ*, 63, 387
- Ertan, Ü., & Alpar, M. A. 2003, *ApJ*, 593, L93
- Ertan, Ü., & Çalışkan, Ş. 2006, *ApJ*, 649, L87

- Ertan, Ü., Ekşi, K. Y., Erkut, M. H., & Alpar, M. A. 2009, *ApJ*, 702, 1309
- Ertan, Ü., Erkut, M. H., Ekşi, K. Y., & Alpar, M. A. 2007, *ApJ*, 657, 441
- Ertan, Ü., Göğüş, E., & Alpar, M. A. 2006, *ApJ*, 640, 435
- Espinoza, C. M., Lyne, A. G., Kramer, M., Manchester, R. N., & Kaspi, V. M. 2011, *ApJ*, 741, L13
- Fahlman, G. G., & Gregory, P. C. 1981, *Nature*, 293, 202
- Fernández, R., & Thompson, C. 2007, *ApJ*, 660, 615
- Feynman, R. P. 1955, *Progress in Low Temperature Physics*, 1, 17
- Foley, S., Kouveliotou, C., Kaneko, Y., & Collazzi, A. 2012, *GRB Coordinates Network*, 13280, 1
- Frail, D. A., Kulkarni, S. R., & Bloom, J. S. 1999, *Nature*, 398, 127
- Franco, L. M., Link, B., & Epstein, R. I. 2000, *ApJ*, 543, 987
- Frank, J., King, A., & Raine, D. J. 2002, *Accretion Power in Astrophysics: Third Edition* (Cambridge, UK: Cambridge University Press)
- Gaensler, B. M., Kouveliotou, C., Gelfand, J. D., et al. 2005, *Nature*, 434, 1104
- Galloway, D. K., Özel, F., & Psaltis, D. 2008, *MNRAS*, 387, 268
- Gavriil, F. P., Dib, R., & Kaspi, V. M. 2011, *ApJ*, 736, 138
- Gavriil, F. P., Kaspi, V. M., & Woods, P. M. 2002, *Nature*, 419, 142
- . 2006, *ApJ*, 641, 418
- Giacconi, R., Gursky, H., Paolini, F. R., & Rossi, B. B. 1962, *Physical Review Letters*, 9, 439
- Ginzburg, V. L., & Kirzhnits, D. A. 1965, *J. Exptl. Theoret. Phys.*, 47, [1965, *Sov. Phys. JETP*, 20, 1346]
- Gold, T. 1968, *Nature*, 218, 731
- . 1969, *Nature*, 221, 25
- Goldreich, P., & Julian, W. H. 1969, *ApJ*, 157, 869
- Götz, D., Mereghetti, S., Tiengo, A., & Esposito, P. 2006, *A&A*, 449, L31
- Götz, D., Rea, N., Zane, S., Turolla, R., & Lyutikov, M. 2009, *ArXiv e-prints*, arXiv:0902.4791
- Götz, D., Rea, N., Israel, G. L., et al. 2007, *A&A*, 475, 317
- Göğüş, E., Güver, T., Özel, F., Eichler, D., & Kouveliotou, C. 2011, *ApJ*, 728, 160

- Griffiths, D. J. 1999, *Introduction to Electrodynamics: Third Edition* (Upper Saddle River, New Jersey 07458: Prentice-Hall, Inc.)
- Groth, E. J. 1975, *ApJS*, 29, 285
- Güver, T., & Özel, F. 2013, *ApJ*, 765, L1
- Güver, T., Özel, F., Cabrera-Lavers, A., & Wroblewski, P. 2010a, *ApJ*, 712, 964
- Güver, T., Özel, F., & Göğüş, E. 2008, *ApJ*, 675, 1499
- Güver, T., Özel, F., Göğüş, E., & Kouveliotou, C. 2007, *ApJ*, 667, L73
- Güver, T., Özel, F., & Lyutikov, M. 2006, *ArXiv Astrophysics e-prints*, astro-ph/0611405
- Güver, T., Wroblewski, P., Camarota, L., & Özel, F. 2010b, *ApJ*, 719, 1807
- Haberl, F., & Pietsch, W. 2005, *A&A*, 438, 211
- Haensel, P., Potekhin, A. Y., & Yakovlev, D. G., eds. 2007, *Astrophysics and Space Science Library*, Vol. 326, *Neutron Stars 1 : Equation of State and Structure*
- Halpern, J. P., & Gotthelf, E. V. 2005, *ApJ*, 618, 874
- Harding, A. K., Contopoulos, I., & Kazanas, D. 1999, *ApJ*, 525, L125
- Hartman, R. C., Bertsch, D. L., Bloom, S. D., et al. 1999, *ApJS*, 123, 79
- Heindl, W. A., Rothschild, R. E., Coburn, W., et al. 2004, in *American Institute of Physics Conference Series*, Vol. 714, *X-ray Timing 2003: Rossi and Beyond*, ed. P. Kaaret, F. K. Lamb, & J. H. Swank, 323–330
- Heinke, C. O., Rybicki, G. B., Narayan, R., & Grindlay, J. E. 2006, *ApJ*, 644, 1090
- Hessels, J. W. T., Ransom, S. M., Stairs, I. H., et al. 2006, *Science*, 311, 1901
- Hewish, A., Bell, S. J., Pilkington, J. D. H., Scott, P. F., & Collins, R. A. 1968, *Nature*, 217, 709
- Hewish, A., & Okoye, S. E. 1965, *Nature*, 207, 59
- Heyl, J. S., & Hernquist, L. 2005a, *ApJ*, 618, 463
- . 2005b, *MNRAS*, 362, 777
- Ho, W. C. G., & Heinke, C. O. 2009, *Nature*, 462, 71
- Hobbs, G., Lyne, A. G., & Kramer, M. 2010, *MNRAS*, 402, 1027
- Horvath, J. E. 2007, *Ap&SS*, 308, 431
- Hu, Y.-M., Pitkin, M., Heng, I. S., & Hendry, M. A. 2014, *ApJ*, 784, L41
- Huang, Y. F., & Geng, J. J. 2014, *ApJ*, 782, L20

Hulleman, F., Tennant, A. F., van Kerkwijk, M. H., et al. 2001, *ApJ*, 563, L49

Hulleman, F., van Kerkwijk, M. H., & Kulkarni, S. R. 2000, *Nature*, 408, 689

Hulse, R. A., & Taylor, J. H. 1975, *ApJ*, 195, L51

Hurley, K., Cline, T., Mazets, E., et al. 1999, *Nature*, 397, 41

Hurley, K., Boggs, S. E., Smith, D. M., et al. 2005, *Nature*, 434, 1098

Iachello, F., Langer, W. D., & Lande, A. 1974, *Nuclear Physics A*, 219, 612

İçdem, B., Baykal, A., & Inam, S. Ç. 2012, *MNRAS*, 419, 3109

Ikhsanov, N. R. 2007, *MNRAS*, 375, 698

Israel, G. L., Campana, S., Dall’Osso, S., et al. 2007a, *ApJ*, 664, 448

Israel, G. L., Covino, S., Stella, L., et al. 1999, *ApJ*, 518, L107

Israel, G. L., Götz, D., Zane, S., et al. 2007b, *A&A*, 476, L9

Israel, G. L., Covino, S., Perna, R., et al. 2003, *ApJ*, 589, L93

Ivanenko, D., & Kurdgelaidze, D. F. 1969, *Nuovo Cimento Lettere*, 2, 13

Jahoda, K., Markwardt, C. B., Radeva, Y., et al. 2006, *ApJS*, 163, 401

Kapitza, P. 1938, *Nature*, 141, 74

Kaplan, D. L., Chakrabarty, D., Wang, Z., & Wachter, S. 2009, *ApJ*, 700, 149

Kaspi, V. M., Chakrabarty, D., & Steinberger, J. 1999, *ApJ*, 525, L33

Kaspi, V. M., & Gavriil, F. P. 2003, *ApJ*, 596, L71

Kaspi, V. M., Gavriil, F. P., Woods, P. M., et al. 2003, *ApJ*, 588, L93

Kaspi, V. M., Lackey, J. R., & Chakrabarty, D. 2000, *ApJ*, 537, L31

Katz, J. I. 2014, *Ap&SS*, 349, 611

Kennea, J. A., Burrows, D. N., Kouveliotou, C., et al. 2013, *ApJ*, 770, L24

Kern, B., & Martin, C. 2002, *Nature*, 417, 527

Krimm, H., Barthelmy, S., Campana, S., et al. 2006, *The Astronomer’s Telegram*, 894, 1

Kuiper, L., den Hartog, P. R., & Hermsen, W. 2008, *ArXiv e-prints*, arXiv:0810.4801

Kuiper, L., Hermsen, W., den Hartog, P. R., & Collmar, W. 2006, *ApJ*, 645, 556

Kuiper, L., Hermsen, W., & Mendez, M. 2004, *ApJ*, 613, 1173

Kumar, H. S., & Safi-Harb, S. 2010, *ApJ*, 725, L191

- Landau, L. D. 1932, *Phys. Z. Sowjetunion*, 1, 285
- Langer, W. D., Rosen, L. C., Cohen, J. M., & Cameron, A. G. W. 1969, *Ap&SS*, 5, 259
- Lattimer, J. M. 2010, *New Astronomy Reviews*, 54, 101
- . 2012, *Annual Review of Nuclear and Particle Science*, 62, 485
- Lattimer, J. M., & Prakash, M. 2001, *ApJ*, 550, 426
- Lazarus, P., Kaspi, V. M., Champion, D. J., Hessels, J. W. T., & Dib, R. 2012, *ApJ*, 744, 97
- Levin, L., Bailes, M., Bates, S., et al. 2010, *ApJ*, 721, L33
- Lin, J., Özel, F., Chakrabarty, D., & Psaltis, D. 2010, *ApJ*, 723, 1053
- Lin, L., Kouveliotou, C., Göğüş, E., et al. 2011, *ApJ*, 740, L16
- Link, B., Epstein, R. I., & Lattimer, J. M. 1999, *Physical Review Letters*, 83, 3362
- Livingstone, M. A., Kaspi, V. M., Gavriil, F. P., et al. 2007, *Ap&SS*, 308, 317
- Lyne, A. G., Burgay, M., Kramer, M., et al. 2004, *Science*, 303, 1153
- Lyutikov, M. 2002, *ApJ*, 580, L65
- . 2013, *ArXiv e-prints*, arXiv:1306.2264
- Lyutikov, M., & Gavriil, F. P. 2006, *MNRAS*, 368, 690
- Manchester, R. N., Hobbs, G. B., Teoh, A., & Hobbs, M. 2005, *VizieR Online Data Catalog*, 7245, 0
- Markwardt, C. B. 2009, in *Astronomical Society of the Pacific Conference Series*, Vol. 411, *Astronomical Data Analysis Software and Systems XVIII*, ed. D. A. Bohlender, D. Durand, & P. Dowler, 251
- Maron, O., Kijak, J., Kramer, M., & Wielebinski, R. 2000, *A&AS*, 147, 195
- Mazets, E. P., Cline, T. L., Aptekar', R. L., et al. 1999, *Astronomy Letters*, 25, 635
- Mazets, E. P., Golenetskij, S. V., & Guryan, Y. A. 1979, *Soviet Astronomy Letters*, 5, 343
- Meegan, C., Lichti, G., Bhat, P. N., et al. 2009, *ApJ*, 702, 791
- Mereghetti, S. 2008, *A&A Rev.*, 15, 225
- . 2011, *Advances in Space Research*, 47, 1317
- . 2013, *Brazilian Journal of Physics*, 43, 356
- Mészáros, P. 1992, *High-energy radiation from magnetized neutron stars*. (Chicago, IL (USA): University of Chicago Press)

- Michel, F. C. 1969, *ApJ*, 158, 727
- Migdal, A. B. 1959, *Nuclear Physics*, 13, 655
- . 1971, *Zh. Eksp. Teor. Fiz.*, 61, 2209
- Miller, M. C. 1992, *MNRAS*, 255, 129
- Miller, M. C., Lamb, F. K., & Psaltis, D. 1998, *ApJ*, 508, 791
- Molkov, S. V., Cherepashchuk, A. M., Lutovinov, A. A., et al. 2004, *Astronomy Letters*, 30, 534
- Morii, M., Kawai, N., & Shibazaki, N. 2005, *ApJ*, 622, 544
- Muno, M. P., Gaensler, B. M., Clark, J. S., et al. 2007, *MNRAS*, 378, L44
- Nobili, L., Turolla, R., & Zane, S. 2008a, *MNRAS*, 386, 1527
- . 2008b, *MNRAS*, 389, 989
- Olausen, S. A., & Kaspi, V. M. 2014, *ApJS*, 212, 6
- Onsager, L. 1949, *Nuovo Cimento Suppl.*, 6, 249
- Oppenheimer, J. R., & Volkoff, G. M. 1939, *Physical Review*, 55, 374
- Ouyed, R., Leahy, D., & Koning, N. 2014, *Ap&SS*, 184
- Özel, F. 2001, *ApJ*, 563, 276
- . 2003, *ApJ*, 583, 402
- . 2006, *Nature*, 441, 1115
- . 2013, *Reports on Progress in Physics*, 76, 016901
- Özel, F., Gould, A., & Güver, T. 2012, *ApJ*, 748, 5
- Özel, F., Güver, T., & Psaltis, D. 2009, *ApJ*, 693, 1775
- Pacini, F. 1967, *Nature*, 216, 567
- Paczynski, B. 1990, *ApJ*, 365, L9
- Pal'shin, V., Aptekar, R., Frederiks, D., et al. 2013, *GRB Coordinates Network*, 15245, 1
- Pandharipande, V. R. 1971, *Nucl. Phys. A*, 178, 123
- Pandharipande, V. R., & Smith, R. A. 1975, *Phys. Lett. B*, 59, 15
- Pines, D., Shaham, J., Alpar, M. A., & Anderson, P. W. 1980, *Progress of Theoretical Physics Supplement*, 69, 376
- Pons, J. A., & Rea, N. 2012, *ApJ*, 750, L6

- Radhakrishnan, V., & Manchester, R. N. 1969, *Nature*, 222, 228
- Rea, N., & Esposito, P. 2011, in *High-Energy Emission from Pulsars and their Systems*, ed. D. F. Torres & N. Rea, 247
- Rea, N., Oosterbroek, T., Zane, S., et al. 2005, *MNRAS*, 361, 710
- Rea, N., Pons, J. A., Torres, D. F., & Turolla, R. 2012, *ApJ*, 748, L12
- Rea, N., Zane, S., Lyutikov, M., & Turolla, R. 2007, *Ap&SS*, 308, 61
- Rea, N., Zane, S., Turolla, R., Lyutikov, M., & Götz, D. 2008, *ApJ*, 686, 1245
- Rea, N., Israel, G. L., Pons, J. A., et al. 2013, *ApJ*, 770, 65
- Revnivtsev, M. G., Sunyaev, R. A., Varshalovich, D. A., et al. 2004, *Astronomy Letters*, 30, 382
- Rheinhardt, M., & Geppert, U. 2002, *Physical Review Letters*, 88, 101103
- Rhoades, C. E., & Ruffini, R. 1974, *Physical Review Letters*, 32, 324
- Richards, D. W., & Comella, J. M. 1969, *Nature*, 222, 551
- Romani, R. W. 1987, *ApJ*, 313, 718
- Ruderman, M. 1969, *Nature*, 223, 597
- . 1976, *ApJ*, 203, 213
- . 1991, *ApJ*, 382, 587
- Ruderman, M., Zhu, T., & Chen, K. 1998, *ApJ*, 492, 267
- Ruderman, M. A. 1968, *Nature*, 218, 1128
- Ruderman, M. A., & Sutherland, P. G. 1975, *ApJ*, 196, 51
- Salvati, M., & Massaro, E. 1978, *A&A*, 67, 55
- Şaşmaz Muş, S., & Göğüş, E. 2013, *ApJ*, 778, 156
- Shapiro, S. L., & Teukolsky, S. A. 1983, *Black Holes, White Dwarfs, and Neutron Stars: The Physics of Compact Objects* (New York: Wiley-Interscience)
- Spitler, L. G., Lee, K. J., Eatough, R. P., et al. 2014, *ApJ*, 780, L3
- Srinivasan, G., Bhattacharya, D., Muslimov, A. G., & Tsygan, A. J. 1990, *Current Science*, 59, 31
- Staelin, D. H., & Reifenstein, III, E. C. 1968, *Science*, 162, 1481
- Sturrock, P. A. 1971, *ApJ*, 164, 529
- Sugizaki, M., Nagase, F., Torii, K., et al. 1997, *PASJ*, 49, L25
- Suleimanov, V. F., Klochkov, D., Pavlov, G. G., & Werner, K. 2014, *ApJS*, 210, 13

- Tam, C. R., Gavriil, F. P., Dib, R., et al. 2008, *ApJ*, 677, 503
- Tam, C. R., Kaspi, V. M., van Kerkwijk, M. H., & Durant, M. 2004, *ApJ*, 617, L53
- Thompson, C., & Beloborodov, A. M. 2005, *ApJ*, 634, 565
- Thompson, C., & Duncan, R. C. 1993, *ApJ*, 408, 194
- . 1995, *MNRAS*, 275, 255
- . 1996, *ApJ*, 473, 322
- . 2001, *ApJ*, 561, 980
- Thompson, C., Duncan, R. C., Woods, P. M., et al. 2000, *ApJ*, 543, 340
- Thompson, C., Lyutikov, M., & Kulkarni, S. R. 2002, *ApJ*, 574, 332
- Thorsett, S. E., & Chakrabarty, D. 1999, *ApJ*, 512, 288
- Tiengo, A., Esposito, P., & Mereghetti, S. 2008, *ApJ*, 680, L133
- Tiengo, A., Esposito, P., Mereghetti, S., et al. 2013, *Nature*, 500, 312
- Tolman, R. C. 1939, *Physical Review*, 55, 364
- Tong, H. 2014, *ApJ*, 784, 86
- Tong, H., Song, L. M., & Xu, R. X. 2010, *ApJ*, 725, L196
- . 2011, *ApJ*, 738, 31
- Tong, H., Xu, R. X., Song, L. M., & Qiao, G. J. 2013, *ApJ*, 768, 144
- Trümper, J., Pietsch, W., Reppin, C., et al. 1978, *ApJ*, 219, L105
- Trümper, J. E., Zezas, A., Ertan, Ü., & Kylafis, N. D. 2010, *A&A*, 518, A46
- Usov, V. V. 1993, *ApJ*, 410, 761
- . 1994, *ApJ*, 427, 984
- van der Klis, M. 1989, in *Timing Neutron Stars*, ed. H. Ögelman & E. P. J. van den Heuvel, 27
- Vandenbroucke, J., Buehler, R., Ajello, M., et al. 2010, *ApJ*, 718, L166
- Vasisht, G., & Gotthelf, E. V. 1997, *ApJ*, 486, L129
- Vaughan, B. A., van der Klis, M., Wood, K. S., et al. 1994, *ApJ*, 435, 362
- Wang, W., Tong, H., & Guo, Y.-J. 2013, *ArXiv e-prints*, arXiv:1311.0107
- Wang, Z., Chakrabarty, D., & Kaplan, D. L. 2006, *Nature*, 440, 772
- Wang, Z., Kaspi, V. M., & Higdun, S. J. U. 2007, *ApJ*, 665, 1292

- Webb, N. A., & Barret, D. 2007, *ApJ*, 671, 727
- Wellstein, S., & Langer, N. 1999, *A&A*, 350, 148
- Weltevrede, P., Johnston, S., & Espinoza, C. M. 2011, *MNRAS*, 411, 1917
- Wheaton, W. A., Doty, J. P., Primini, F. A., et al. 1979, *Nature*, 282, 240
- Woods, P. M., Kaspi, V. M., Gavriil, F. P., & Airhart, C. 2011, *ApJ*, 726, 37
- Woods, P. M., & Thompson, C. 2006, Soft gamma repeaters and anomalous X-ray pulsars: magnetar candidates, ed. W. H. G. Lewin & M. van der Klis, 547–586
- Woods, P. M., Kouveliotou, C., van Paradijs, J., et al. 1999, *ApJ*, 524, L55
- Woods, P. M., Kaspi, V. M., Thompson, C., et al. 2004, *ApJ*, 605, 378
- Woosley, S. E., Heger, A., & Weaver, T. A. 2002, *Reviews of Modern Physics*, 74, 1015
- Xu, R. 2007, *Advances in Space Research*, 40, 1453
- Yu, M., Manchester, R. N., Hobbs, G., et al. 2013, *MNRAS*, 429, 688
- Zane, S., Rea, N., Turolla, R., & Nobili, L. 2009, *MNRAS*, 398, 1403
- Zhu, W., & Kaspi, V. M. 2010, *ApJ*, 719, 351